UNIVERSITA' DEGLI STUDI DI PADOVA

FACOLTA' DI INGEGNERIA

Analisi teorica e sperimentale di un sistema di controllo per un veicolo biomimetico "Boxfish"

RELATORE: Ch.mo Prof. Luca Schenato
CORRELATORE: Ch.ma Prof.ssa Xinyan Deng

LAUREANDO: Giovanni Barbera

A.A. 2008-2009

"You need chaos in your soul to give birth to a dancing star."

Friedrich Nietzsche

Contents

Abstract

Negli ultimi decenni l'applicazione in campo ingegneristico delle tecniche adottate in natura per consentire una rapida ed efficiente locomozione sta prendendo sempre più piede, tanto da dare il nome ad una nuova branca della Scienza, la "Biomimetica". Con ciò non si non vuole tuttavia, come potrebbe suggerire il termine, operare una semplice *imitazione* dei meccanismi (peraltro spesso complessi) impiegati dai diversi animali per muoversi e spostarsi efficacemente. L'interesse è piuttosto indirizzato alla comprensione ed alla formalizzazione matematica di tali meccanismi, finalizzata alla riproduzione di modelli, spesso semplificati, che sfruttino in modo analogo i medesimi principi.

Su questa linea guida è stato svolto il presente lavoro, che mira a discutere e proporre nuove soluzioni nell'ambito del controllo di un veicolo sottomarino autonomo ispirato al modello del "boxfish", un particolare pesce tropicale racchiuso in uno squadrato carapace. Le doti natatorie di questo esemplare, per lungo tempo sottovalutate a causa del profilo decisamente poco idrodinamico dell'esemplare, sono state negli ultimi anni fortemente rivalutate, divenendo oggetto di studio per la notevole agilità e la sorprendente efficienza energetica dimostrate.

L'intero lavoro è suddiviso in due sezioni principali: nella prima viene studiato e proposto un modello matematico completo di veicolo sottomarino con propulsione a pinna, costruito *ad hoc* sul modello del *boxfish*; lo studio è indirizzato in particolare agli effetti idrodinamici legati all'interazione del corpo con il fluido circostante e all'azione prodotta sul veicolo dall'oscillazione delle pinne pettorali e della pinna caudale.

Segue quindi una verifica sperimentale su un modello appositamente realizzato: algoritmi di controllo attitudinale mediante sensor fusion sono discussi e adattati all'utilizzo di pinne pettorali come attuatori; l'orientazione del veicolo viene stimata con metodi geometrici sulla base di dati raccolti da sensori eterogenei installati a bordo, e l'efficacia degli algoritmi di controllo proposti è supportata sia da realistiche simulazioni al calcoltore sul modello proposto, sia da dati sperimentali raccolti sul campo.

Chapter 1

Introduction

Fish swimming is one of the most impressive example of control one can find in nature. Because such complex interactions between body, fins and water are involved, the modeling, development and control of a robotic fish is a challenging issue, both from a technologic and from a theoretical point of view.

Over the last two decades marine locomotion has been an active area of research both for engineers and biologists [1–3]. The interest in Autonomous Underwater Vehicles (AUVs) is to be attributed to the large number of practical purposes (e.g., ocean exploration), especially those in cluttered or dangerous environments, such as in very deep or cold water, in offshore platforms, etc. Animal aquatic locomotion systems, based on a five hundred million year evolution and continuous improvement by natural selection, has been a constant source of inspiration for engineers. New trends in robotics are heading toward the design of bio-inspired models, especially for aerial and aquatic locomotion: based on the observation of fish, insects, and birds behavior, new kinds of propellers and actuators have been proposed, to increase efficiency and maneuverability [4, 5].

The aim of this project is not just a mere reproduction of a fish shape and its mechanical locomotion patterns though; this purpose would be hard to pursue even with the help of the most advanced technologies, because of the high degree of complexity of biological actuators.

Because of the increasing interest in fish swimming techniques, a flourishing literature is available on this topic, this providing an exhaustive analysis of biological and kinematics aspects and basic principles which underlie marine locomotion.

In the following section an overview of fish locomotion is briefly presented.

1.1 How fish swim

Fish swimming modes and techniques are so wide and numerous that trying to classify all of them is not an easy task. A first distinction can be made between transient, unsteady swimming mechanisms [6, 7] and periodic motion patterns for thrust generation and maneuvering; in this work we focus on the latter, since it is the most suitable for control.

Before proceeding, some basic definitions and terminology which will be used throughout the next sections need to be introduced (see Fig. 1.1):

- *Paired fins*: fins which can be found only in symmetric pairs (pectoral and pelvic fins belong to this category).
- *Median fins*: fins which lie on the median axis of the body (dorsal and anal fins belong to this category).
- *TL*: total body length; a common speed unit for fishes is $TL\text{s}^{-1}$.
- *Gait*: "a pattern of locomotion characteristic of a limited range of speeds described by quantities of which one or more change discontinuously at transitions to other gaits" [8].

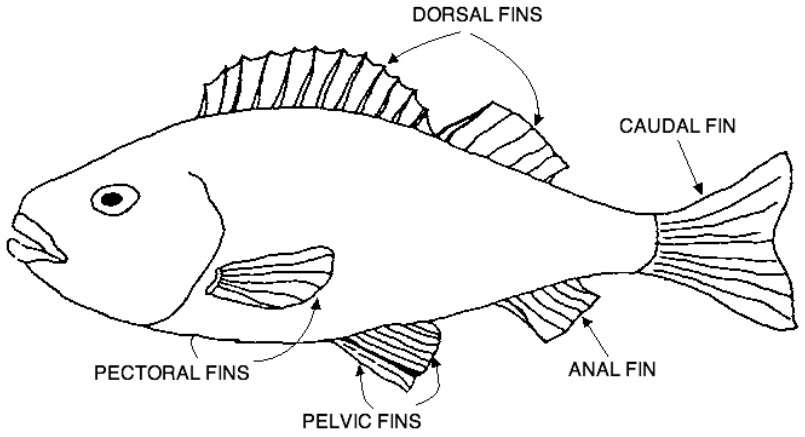

FIGURE 1.1: Morphology of fishes.

1.1.1 Fish classification

Generally, different fish swim in different ways, therefore one possible classification is based on the method employed to produce thrust: fish can thus be roughly divided

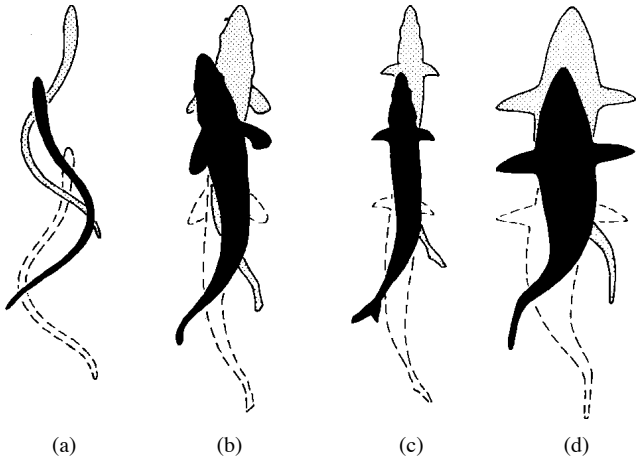

FIGURE 1.2: Different degrees of undulatory motion for BCF swimmers: (a) anguilliform, (b) subcarangiform, (c) carangiform and (d) thunniform. Courtesy of [9].

into two categories [2, 10], *body and/or caudal fin* (BCF) swimmers and *median and/or paired fin* (MPF) swimmers[1]. The former category — the most common one — employs basically the caudal fin and/or the oscillation of the body to generate thrust (ranging from the *anguilliform* to the *thunniform*, see Fig. 1.2); the latter

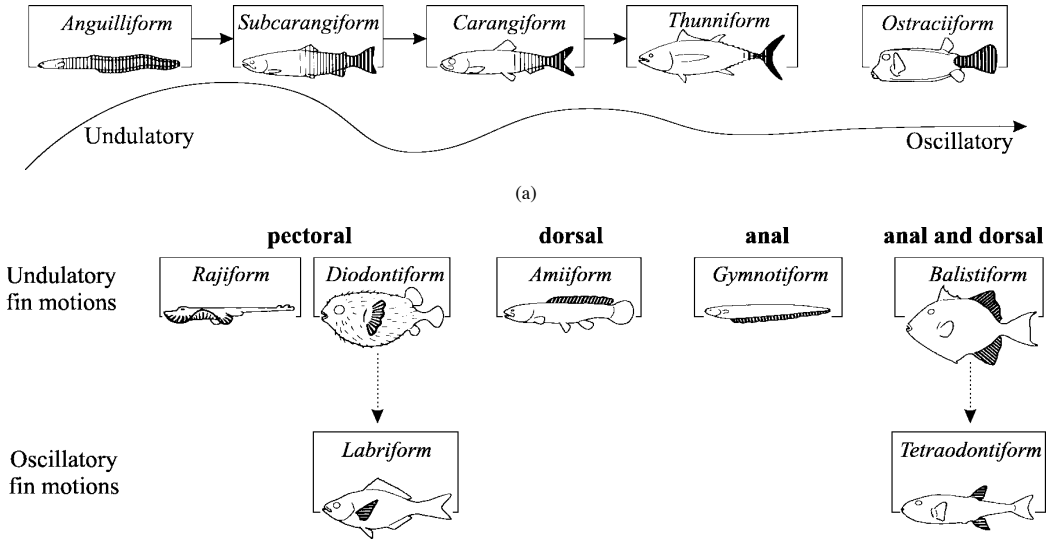

FIGURE 1.3: Fish classification based on BCF (top) and MPF (bottom) swimming techniques. Courtesy of [9].

[1]In fact this is not to be taken as a rigid dichotomy, since both swimming mode can be observed in the same species at different gaits.

employs the paired fins to generate thrust, which has proven to be less efficient than using the caudal fin, at least at cruising speeds; nonetheless MPF swimmers exhibit a remarkable maneuverability, especially at low speeds, and this is a more appealing quality for our purpose.

A further classification criterion concerns the type of movement observed in the propulsive structure: the motion is said to be *undulatory* if a waveform is visible along the propulsive structure; the motion is *oscillatory* if thrust is generated by the only oscillation about a fixed point of the propulsive structure. An overview of the different swimming modes is shown in Fig. 1.3.

1.1.2 The issue of stability

Besides the thrust generated by fins or body, fish are subjected to other forces and torques, mainly caused by hydrostatic restoring forces (i.e. gravity and buoyancy) [11].

One aspect worth of being stressed is that fish are statically unstable [3]: most fish are indeed negatively buoyant, that is they need to incessantly flap their fins not to sink. Moreover in most cases the center of buoyancy is located slightly below the center of mass [12], and this causes the body to have an unstable equilibrium (a minimum perturbation would provoke a roll movement, making the body drift away from the equilibrium position), thus a constant active fin control is needed in order to maintain a stable position. In addition to this, BCF swimming mode, having the thrust produced mainly by the posterior part of the body, is unstable in yaw [13], and even for straightforward motions a continuous yaw control (either with fins or with body undulations) is required. This is apparently a wasteful energy consumption, and one could wonder why fish are unstable and need to spend energy even just to hover and keep a horizontal position. The point is to be found in the trade-off between stability and maneuverability [14]: the instability is exploited to ease maneuvers. The same principle was kept in mind by the designers of aircraft Sukhoi Su-47 or Grumman X-29 (see Fig. 1.4), in which the forward-swept wings exploit the inherent aerodynamic instability to make the airplane extremely agile and maneuverable.

Thus in fish locomotion system, generally, more importance is given to maneuverability rather than to efficiency, and this is reasonable on account of the importance of being capable of rapid, sudden motions in underwater environment (e.g. for hunting or escaping, or feeding in turbulent waters or difficult locations such as coral reefs, etc..). Exploiting instability for the sake of maneuverability is a well known

FIGURE 1.4: Nasa x-29 forward swept wing aircraft. Its dynamic instability makes it highly maneuverable, even though a closed loop control is required to be constantly active.

issue in aerial vehicles control, and the risks related to the need of constantly rely on a feedback control for maintaining a stable posture are widely known as well [15].

Because of its strong influence on the dynamics of the AUV, the choice of the hydrostatic stability is one of the very first thing to be taken into account when designing the model, in conformity with the purpose the AUV is built for.

1.2 The boxfish

Among all the species of fish there is one which in the last few years attracted the interest of biologists and engineers: the boxfish[2]; its peculiarity and most interesting feature is that it's completely enclosed in a bony carapace, and this makes its shape

[2]With this term is commonly indicated the *Ostraciidae*, belonging to the order *Tetradontiformes*.

and hydrodynamic behavior very different from the one usually observed in streamlined, thunniform-like fishes. In particular we are interested in a genus of *Ostraciidae*, the *Ostracion meleagris*, also known as *whitespotted boxfish* (see Fig. 1.5).

FIGURE 1.5: A male specimen of whitespotted boxfish (*Ostracion meleagris*), depicted in his natural habitat, the coral reef.

1.2.1 Morphology

Boxfishes dwell in coral reefs and rocky, low depth environments, so they constantly cope with turbulent waters and need to maneuver and feed in narrow environments. To deal with these difficulties, they developed a passively stable shape, which makes them less sensitive to currents and disturbances. Even though different shapes have been developed among *Ostraciidae*, Bartol *et al.* pointed out some common aspects which underlie their hydrodynamic stability [16, 17]. In particular, from the analysis of the flow around the shape of stereolithographic models of different kinds of boxfishes, the stabilizing vortices produced by the dorsal and ventral keels have been observed both in pitch and yaw stabilization, even at wide angles of attack. The study was supported by PIV experiments on the real fish [18].

Despite the significant drag component related to its shape, recent studies surprisingly proved that hydrodynamic efficiency of boxfish is almost undistinguishable from that of most streamlined thunniform like swimmers [19, 20]; such a surprising discovery led Mercedes-Benz Technology Center to develop a high-efficiency

car based on the tropical fish's shape (see Fig. 1.6), with outstanding aerodynamic performances.

FIGURE 1.6: The bionic car inspired to the boxfish, developed in 2006 by Mercedes-Benz. Courtesy of [21].

As shown in Fig. 1.7, boxfishes make use of one pair of thin pectoral fins, inclined of about $-45°$ with respect to the horizontal, dorsal and anal fins, and a rather stiff caudal fin, used in a completely oscillatory mode. The next section describes how these fins are employed to produce thrust and maneuver.

1.2.2 Swimming style

Boxfishes present a varied swimming technique, depending on the speed they are cruising at; in particular, as observed by Hove *et al.* in [20], they employ three major gaits: at very low speeds ($< 1TL\text{s}^{-1}$, mainly adopted for hovering and feeding) the sole pectoral and anal fins are used (the caudal fin acts as a rudder); the trajectories are very irregular and unpredictable, this resulting in a quite complex combination of movements, with no evident patterns nor recognizable finbeat frequencies. The second and most used gait ($1 - 5TL\text{s}^{-1}$) basically makes use of a dorsal/anal fin combined movement to produce thrust, and the finbeat frequency increases linearly with speed. At higher speeds ($> 5TL\text{s}^{-1}$) fins are folded to reduce the drag, and swimming mode switches from MPF to BCF, thus using the only caudal fin to produce thrust in burst-and-coast mode.

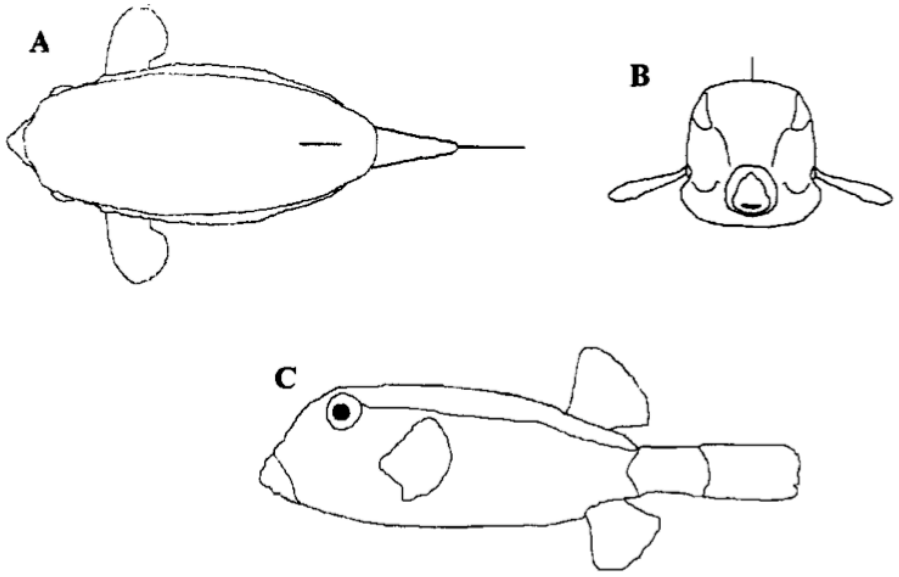

FIGURE 1.7: The whitespotted boxfish shape, in dorsal (A), frontal (B) and lateral (C) view.

In this work we will focus on the first gait, analyzing the use of pectoral fins for hovering and maneuvering.

1.3 State of the art

The extraordinary advance in biomimetic AUV design led to important results in underwater vehicles development; here we present a summary of the studies and of the experimental results achieved so far in AUV control theory. In particular, the focus is on bio-inspired propulsion mechanisms[3].

Undoubtedly the most adopted propulsion system in bio-inspired AUV locomotion is the carangiform like swimming mode, both for its efficiency and for its ease to be reproduced, even with a limited number of actuators (e.g. with a dual-link or three-link mechanism). Morgansen *et al.* in [25] and [26] proposed a rather simple model and a control algorithm for carangiform locomotion, and the results are validated through experiments on a fin-actuated AUV. Another excellent example is AUV Robotuna, developed by Triantafyllou *et al.* [27] at MIT laboratories (see Fig. 1.8): its six links are controlled through a genetic algorithm to mimic the thunniform

[3]Conventional underwater vehicles and their control is treated, for instance, in [22] for propeller-based AUV or in [23, 24] for gliders.

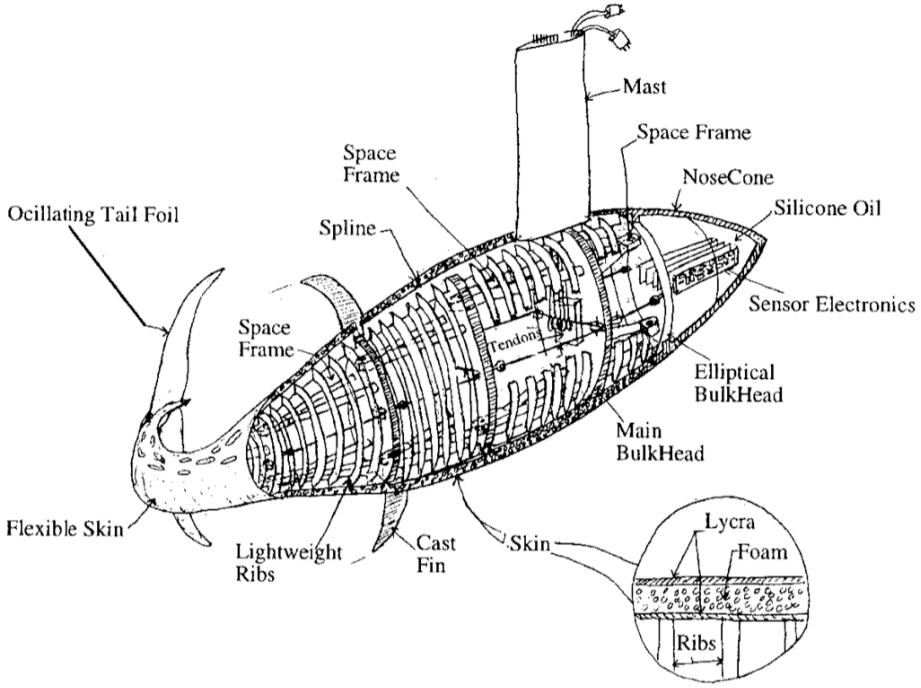

FIGURE 1.8: The AUV model Robotuna, developed at MIT laboratories. Courtesy of [27].

locomotion and improve efficiency. A similar model, based on the traveling wave's kinematics, is studied by Yu *et al.* in [28], who successfully adopted a point-to-point motion algorithm to control a four-link radio controlled biomimetic fish (see Fig. 1.9).

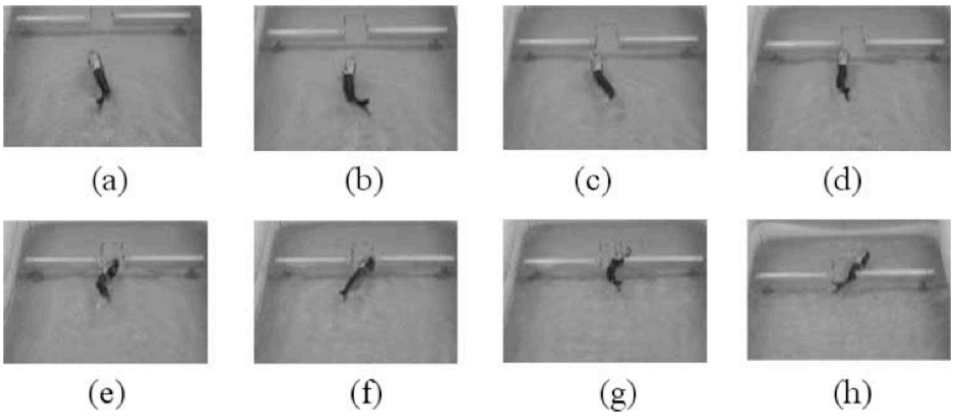

FIGURE 1.9: Sequence of images of the robotic fish passing through a hole. Courtesy of [28].

A different kind of biomimetic propulsion has been studied in [29], which the thrust is generated by a total body undulation (the realization of the robot is shown in Fig. 1.10); a model and a control algorithm for this kind of anguilliform-like AUV was proposed by McIsaac and Ostrowski in [30].

FIGURE 1.10: The lamprey robot designed by Ayers *et al.* in [29].

The approach adopted by Kato when designing "BASS III" AUV (see Fig. 1.11) focuses on the maneuverability of the vehicle which is controlled mainly by pectoral fins: in [31] a model was derived and a mechanical pectoral fin was built: a gimbal structure allows a three-degree-of-freedom motion (lead-lag, feathering and flapping), where each rotation is controlled by a different DC motor. Experimental tests proved the high maneuverability that can be achieved employing pectoral fins, both in ascending/descending maneuvers and in yaw control.

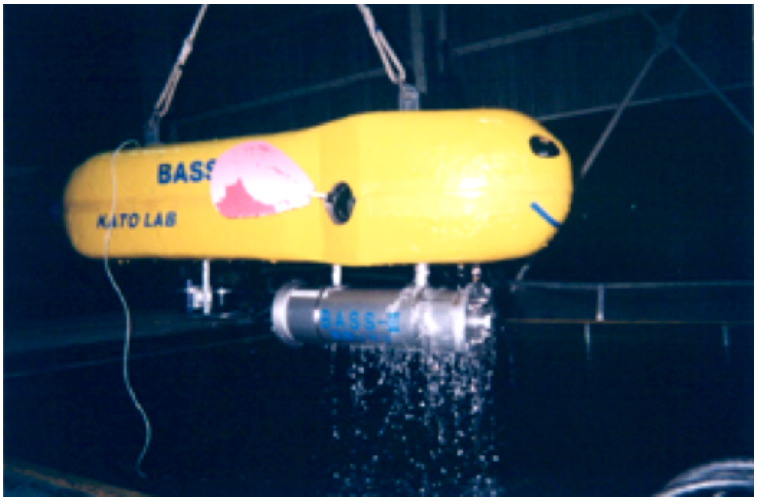

FIGURE 1.11: The 2.2m long AUV "BASS III", developed by Kato with Tokai University. Courtesy of [32].

Another interesting solution is proposed with the AUV AQUA, shown in Fig. 1.12, an hexapod robot which employs his six single-DoF paddles for propulsion and

maneuvering; its theoretical model is described and tested in a simulation environment by Georgiades *et al.* in [33] and [34].

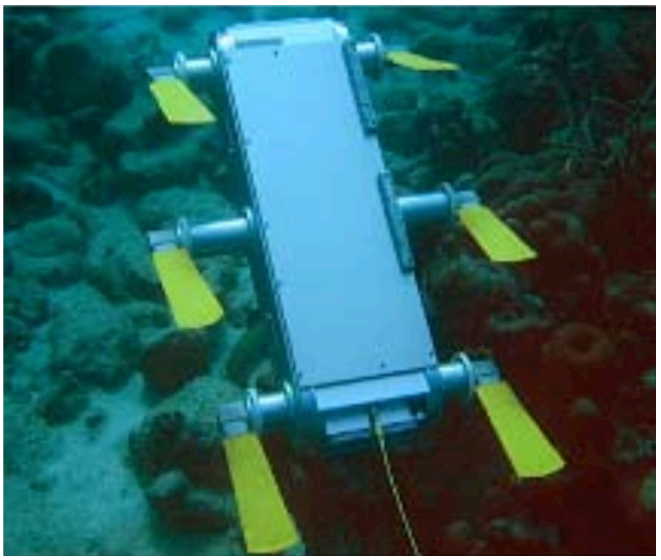

FIGURE 1.12: The hexapod underwater robot AQUA. Courtesy of [33].

Most of the propulsion systems discussed above employ electromagnetic actuators such as DC motors or servos to drive the links. Nevertheless there are some interesting options to these conventional kinds of actuators: recently, for instance, the introduction of "smart materials" gave birth to a new type of oscillating fins, based on ionic polymer actuators [5]. These materials are bent when a voltage is applied to its surfaces, with a displacement proportional to the electrical potential difference; the ease of realization for these kind of actuators allows a miniaturization of the AUV, as successfully done by Guo *et al.* in [35] and [36] (see Fig. 1.13).

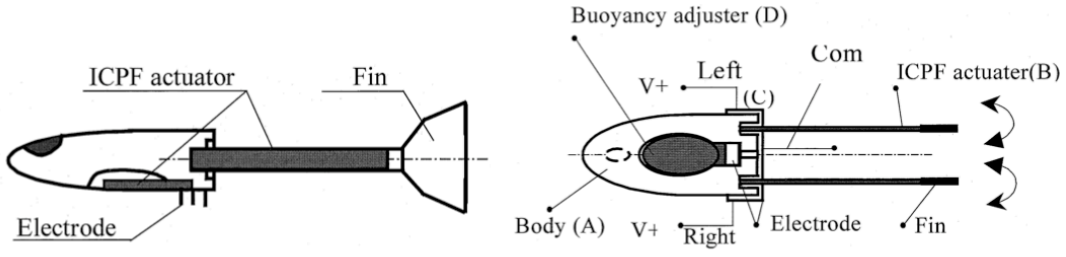

FIGURE 1.13: Side and top view of the 45mm long biomimetic AUV designed by Guo *et al.* in [35], employing a ionic polymer actuator for the tail fin.

Another mechanism that allows centimeter-scaled vehicles fabrication is piezoelectric actuation; its relatively fast response — up to 400Hz — makes it widely used, with different amplification mechanisms, in the design of mechanical flying insects (MFIs) [37]. as well as micro underwater vehicles [38].

The biomimetic tendon drive fish tail realized by Watts in [39] for the RoboSalmon is a smart solution to simplify the design and control of a ten joint mechanical tail: one single DC motor drives the joints through one pair of tendon wires attached to the front end of the tail, with good approximation of carangiform tail fin motion pattern.

As regarding ostraciiform AUV design, it recently became an active area of research, and this is to be ascribed to the simplicity of the model, the ease of reproduction and, as demonstrated in recent studies, its efficiency and maneuverability. Deng *et al.* focused on the modeling and construction of a centimeter-scale robotic boxfish [38] and on a 1:1 scale model with pectoral and caudal fins [40–42]. Lachat developed another example of bio-inspired osctraciiform AUV, BoxyBot [43], which

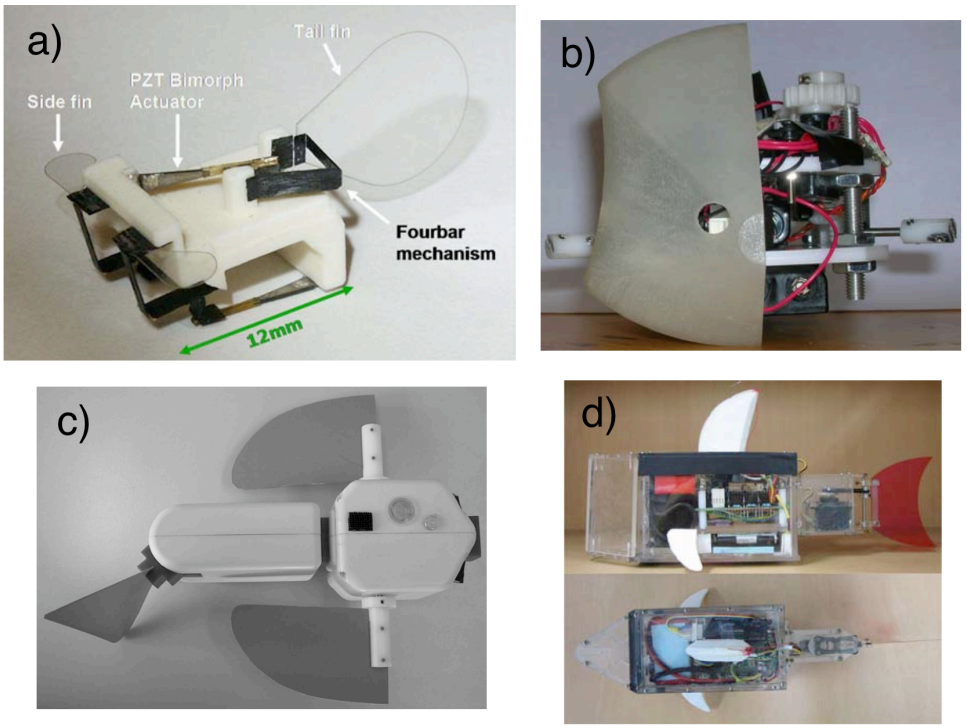

FIGURE 1.14: The four boxfishes model developed by: a) Deng [38], b) Kodati [40–42], c) Lachat [43], d) Chan [44].

is fully autonomous due to its light and water sensors, and it is controlled via a central pattern generator (CPG) that allows the AUV to perform maneuvers such as swimming forward, backward, up or down, turning, crawling or spinning about the roll axis. Finally, Chan *et al.* presented experimental results of yaw control using the tail fin mean angle as control variable [44], and recording the heading of the AUV through an onboard inertial measurement unit. The four robotic boxfishes discussed above are shown in Fig. 1.14.

1.4 Contribution

With the present work, a general approach to the problem of AUV modeling and control is presented, by analyzing bio-inspired propulsion and maneuvering mechanisms and related issues. The main goals can be summarized in what follows:

- A simple but still accurate (for control's sake) mathematical model for a finned AUV is proposed.
- Simulations of the presented model are performed in Matlab environment, and a control algorithm based on the complementary filter is tested as well.
- Sensor fusion algorithm for attitude estimation is experimentally validated on the boxfish model, proving the observer to be an excellent and robust state estimator capable of providing highly reliable data for feedback control.
- Attitude stabilization algorithms via pectoral fins are discussed, with the support of experimental data.

1.5 Thesis outline

In Chapter 2, after a brief introduction of some useful concepts, the AUV model is discussed: through a detailed explanation of the various forces acting on the vehicle, the full Newton-Euler equations are derived, in a form suitable for direct torque control. Although with some reasonable simplifications, the model takes into account the three dimensional body dynamics along with the hydrodynamics forces acting on the AUV due to pectoral and caudal fin oscillations.

Chapter 3 tackles the issue of attitude estimation and stabilization, by proving the validity of the geometric approach proposed by Campolo *et al.* in [45], which is tested and validated through a set of experimental data and realistic simulations

on the model proposed in Chapter 2. The encouraging results suggest that this control algorithm can be successfully adopted in many practical situations, due to its robustness and excellent performance.

In Chapter 4 different sets of experimental data, compared with numerical simulations, are reported to validate the proposed control algorithm for the attitude control via pectoral fins. In particular, this section focuses on the effectiveness of pectoral fin based control for the roll and yaw stabilization.

Chapter 5 summarizes the main aspects and results achieved in this work, discussing some open issues and fields of application for the presented results; possible future developments are outlined as well.

Chapter 2

Modeling

The study of vehicle dynamics in underwater environment is, by itself, a complex topic to tackle; hydrodynamics and unsteady mechanisms related to fin-based propulsion make the task of modeling a bio-inspired AUV even more challenging. Depending on the accuracy needed, the resulting model can greatly vary in complexity, nevertheless, some simple models were proven to be effective for many common applications, as well as for theoretical studies on AUV control and identification [46–48].

In the following sections the equations for the dynamical model of the AUV are derived, examining and discussing the most significant components and forces acting on the vehicle.

2.1 Basic notions

Some basic geometric concepts, useful to identify AUV position and orientation in the 3-D space, are now introduced (for a complete treatment of these topics the reader is referred to [12, 49–51]). Before proceeding, few words to explain the notation adopted throughout this chapter need to be spent.

2.1.1 Geometric representation

To model the AUV dynamics and kinematic, two frame of reference are of particular interest: the inertial frame (or space frame) $\{\mathcal{S}\}$ and the body frame $\{\mathcal{B}\}$; the former is assumed to be fixed to a point of the real world, while the latter has its origin in the AUV center of mass, and moves jointly with it. Both $\{\mathcal{S}\}$ and $\{\mathcal{B}\}$ are taken to be right-handed coordinate systems, with z-axis pointing downward (see Fig. 2.1).

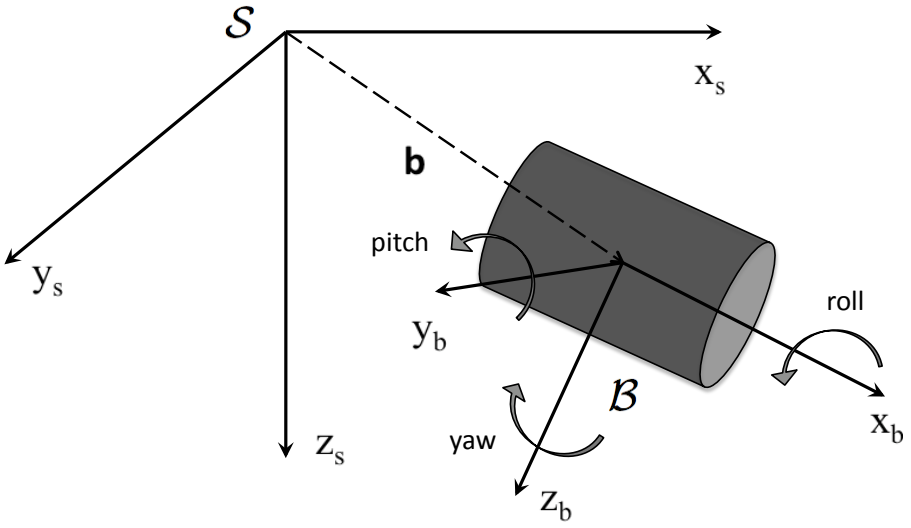

FIGURE 2.1: The inertial reference frame (or space frame) $\{\mathcal{S}\}$ and the body frame $\{\mathcal{B}\}$, assumed to move aligned with the center of mass of the body.

The superscript index $\mathbf{x}^s$ or $\mathbf{x}^b$ is used to indicate the reference frame a generic vector $\mathbf{x}$ is defined with respect to.

2.1.2 Rotations and rigid motions in $\mathbb{R}^3$

Every rotation of the body frame with respect to $\{\mathcal{S}\}$ can be described by a rotation matrix $R \in SO(3)$, where $SO(3)$ denotes the three-dimensional *special, orthogonal* space:

$$SO(3) = \left\{R \in \mathbb{R}^{3\times 3} : RR^T = I \wedge \det R = +1\right\} \tag{2.1}$$

Generally, any rotation can be thought of as a composition of three sequential rotations; depending on which axes these rotations are assumed to occur about, different representations are employed. In the present work ZYX Euler angles (also referred to as Tait- Bryan angles) are adopted, thus, denoting with ϕ, θ and ψ roll, pitch and yaw angles, respectively, any rotation $R_{\mathcal{SB}}$ from $\{\mathcal{S}\}$ to $\{\mathcal{B}\}$ can be written in the form

$$R_{\mathcal{SB}} = R_x(-\phi)R_y(-\theta)R_z(-\psi) \tag{2.2}$$

where

$$R_x = \begin{bmatrix} 1 & 0 & 0 \\ 0 & \cos\phi & -\sin\phi \\ 0 & \sin\phi & \cos\phi \end{bmatrix} R_y = \begin{bmatrix} \cos\theta & 0 & \sin\theta \\ 0 & 1 & 0 \\ -\sin\theta & 0 & \cos\theta \end{bmatrix} R_z = \begin{bmatrix} \cos\psi & -\sin\psi & 0 \\ \sin\psi & \cos\psi & 0 \\ 0 & 0 & 1 \end{bmatrix} \tag{2.3}$$

Hence the inverse map (from $\{\mathcal{B}\}$ to $\{\mathcal{S}\}$) is obtained by transposing Eqn. (2.2):

$$R = R_{\mathcal{SB}}^T = \begin{bmatrix} c_\psi c_\theta & -s_\psi c_\theta + c_\psi s_\theta s_\phi & s_\psi s_\phi + c_\psi s_\theta c_\phi \\ s_\psi c_\theta & c_\psi c_\theta + s_\psi s_\theta s_\phi & -c_\psi s_\phi + s_\psi s_\theta c_\psi \\ -s_\theta & c_\theta s_\phi & c_\theta c_\phi \end{bmatrix} \tag{2.4}$$

where s_ϕ and c_ϕ denote, respectively, $\sin\phi$ and $\cos\phi$, and so on.

Because this is a surjective map, with the only exception of the singularity in $\theta = \pm\pi/2$, one can directly evaluate ϕ, θ and ψ inverting Eqn. (2.4):

$$\begin{cases} \theta &= -\arcsin(r_{31}) \\ \phi &= \text{atan2}(\frac{r_{32}}{\cos(\theta)}, \frac{r_{33}}{\cos(\theta)}) \\ \psi &= \text{atan2}(\frac{r_{21}}{\cos(\theta)}, \frac{r_{11}}{\cos(\theta)}) \end{cases} \tag{2.5}$$

Besides rotations, in order to completely describe any rigid motion in $\mathbb{R}^3$, translations need to be considered: let $\mathbf{b} \in \mathbb{R}^3$ be the vector from the origin of $\{\mathcal{S}\}$ to the origin of $\{\mathcal{B}\}$ (as illustrated in Fig. 2.1) and $R \in SO(3)$ the rotation matrix relative to the orientation of $\{\mathcal{B}\}$ with respect to $\{\mathcal{S}\}$; then every possible configuration of the rigid body in $\mathbb{R}^3$ with respect to the space frame $\{\mathcal{S}\}$ can be expressed by the pair $(\mathbf{b}, R) \in SE(3)$, where $SE(3)$ denotes the *special Euclidean group*:

$$SE(3) = \{(\mathbf{b}, R) \,:\, \mathbf{b} \in \mathbb{R}^3, R \in SO(3)\} \tag{2.6}$$

2.2 Newton-Euler equations

Traditionally AUVs are modeled as rigid bodies surrounded by an irrotational, inviscid, incompressible fluid, and freely moving in a 3-D space (therefore with 6 degrees of freedom), with a set of nonlinear, first-order differential equations. For convenience the dynamics equations are considered with respect to the body-fixed frame, thus, combining Newton's second law for linear motion and Euler's equation for angular

motion, one gets:

$$\begin{bmatrix} mI & 0 \\ 0 & \mathcal{I} \end{bmatrix} \begin{bmatrix} \dot{\mathbf{v}}^b \\ \dot{\boldsymbol{\omega}}^b \end{bmatrix} + \begin{bmatrix} \boldsymbol{\omega}^b \times m\mathbf{v}^b \\ \boldsymbol{\omega}^b \times \mathcal{I}\boldsymbol{\omega}^b \end{bmatrix} = \begin{bmatrix} \mathbf{f}^b \\ \boldsymbol{\tau}^b \end{bmatrix} \tag{2.7}$$

being m the mass of the AUV, $I \in \mathbb{R}^{3\times3}$ the identity matrix, $\mathbf{v}^b$ and $\boldsymbol{\omega}^b$ respectively the linear and angular velocity in the body-fixed frame, $\mathcal{I}$ the inertia tensor (relative to the body frame), and $\mathbf{f}^b$ and $\boldsymbol{\tau}^b$ the external force and torque, applied to the center of mass of the AUV; the cross products represent the Coriolis effect due to the fact that $\{\mathcal{B}\}$ is not an inertial frame.

Let $\mathbf{v}^b$, $\boldsymbol{\omega}^b$, $\mathbf{f}^b$ and $\boldsymbol{\tau}^b$ be defined as follows:

$$\mathbf{v}^b = \begin{bmatrix} u \\ v \\ w \end{bmatrix} \quad \boldsymbol{\omega}^b = \begin{bmatrix} p \\ q \\ r \end{bmatrix} \quad \mathbf{f}^b = \begin{bmatrix} f_x \\ f_y \\ f_z \end{bmatrix} \quad \boldsymbol{\tau}^b = \begin{bmatrix} \tau_x \\ \tau_y \\ \tau_z \end{bmatrix} \tag{2.8}$$

Concerning the structure of the inertia matrix $\mathcal{I}$, since the body of the AUV is symmetrical with respect to the vertical plane, off-diagonal terms of the inertia tensor $\mathcal{I}$ are identically zero, except for the cross term I_{xz}. Hence $\mathcal{I}$ becomes

$$\mathcal{I} = \begin{bmatrix} I_{xx} & 0 & I_{xz} \\ 0 & I_{yy} & 0 \\ I_{xz} & 0 & I_{zz} \end{bmatrix} \tag{2.9}$$

and Eqn. (2.7) can be expanded as:

$$\begin{cases} m(\dot{u} - rv + qw) &= f_x \\ m(\dot{v} + ru - pw) &= f_y \\ m(\dot{w} - uq + pv) &= f_z \\ I_{xx}\dot{p} + rq(I_{zz} - I_{yy}) + I_{xz}(\dot{r} + qp) &= \tau_x \\ I_{yy}\dot{q} + rp(I_{xx} - I_{zz}) + I_{xz}(r^2 - p^2) &= \tau_y \\ I_{zz}\dot{r} + qp(I_{yy} - I_{xx}) + I_{xz}(\dot{p} - qr) &= \tau_z \end{cases} \tag{2.10}$$

The external wrench applied to the AUV, which is described in the right hand side of Eqn. (2.10), is briefly discussed in the next section.

2.3 External forces

External forces $\mathbf{f}^b$ and torques $\boldsymbol{\tau}^b$ are the combination of different factors acting on the AUV:

$$\mathbf{f}^b = \sum_{i=1}^{N} \mathbf{f}_i^b, \qquad \boldsymbol{\tau}^b = \sum_{i=1}^{N} \boldsymbol{\tau}_i^b \tag{2.11}$$

The most significant components are due to the effect of the forces considered below.

2.3.1 Gravity

According to *Newton's second law*, the force exerted by gravity at the center of mass of the AUV can be expressed in the inertial frame $\{\mathcal{S}\}$ as $\mathbf{f}^s = m\mathbf{g}$ where $\mathbf{g}$ is the gravitational acceleration vector expressed in space frame coordinate: $\mathbf{g} = [0\ 0\ g]^T = [0\ 0\ 9.8]^T$. Operating a change of reference via R^T yields:

$$\mathbf{f}_g^b = R^T \mathbf{f}_g^s = mR^T \mathbf{g} = mg \begin{bmatrix} -\sin\theta \\ \cos\theta \sin\phi \\ \cos\theta \cos\phi \end{bmatrix} \tag{2.12}$$

which is the gravity force vector with respect to the body frame $\{\mathcal{B}\}$. Notice that the force is considered to be applied at the AUV center of mass, hence the resulting torque $\boldsymbol{\tau}_g^b$ is identically zero.

2.3.2 Buoyancy

The other hydrostatic force acting on any body submerged in a fluid is buoyancy, a force pointing upward and whose magnitude, according to *Archimede's principle* is equal to the weight of the fluid displaced by the body itself. This force acts at the center of buoyancy of the AUV (which is taken to be different from the center of mass); the displacement between these two points gives raise to a restoring momentum, and their relative position is the crucial parameter which determines AUV hydrostatic stability [11].

Let $\mathbf{x}_b = [x_b\ y_b\ z_b]^T$ be the coordinate of the center of buoyancy with respect to the body frame, then $\mathbf{f}_b^c$, which denote the buoyancy force acting at the center of buoyancy, is equal to

$$\mathbf{f}_b^c = -\rho V \mathbf{g} \tag{2.13}$$

where ρ represents the density of the fluid in which the AUV is submerged, V is the volume of the displaced fluid and g is the gravity vector in space frame coordinate. Since the AUV is considered to be symmetric in the x-z plane, it is reasonable to assume that the center of buoyancy lies along the same plane, hence $y_b = 0$, and the resulting force and torque written in body coordinate system become:

$$\begin{cases} \mathbf{f}_b^b = R^T \mathbf{f}_b^c = \rho V g \begin{bmatrix} \sin\theta \\ -\cos\theta \sin\phi \\ -\cos\theta \cos\phi \end{bmatrix} \\ \boldsymbol{\tau}_b^b = \mathbf{x}_b \times \mathbf{f}_b^b = \rho V g \begin{bmatrix} -z_b \cos\theta \sin\phi \\ -z_b \sin\theta - x_b \cos\theta cos\phi \\ x_b \cos\theta \sin\phi \end{bmatrix} \end{cases} \tag{2.14}$$

2.3.3 Hydrodynamic forces

The motion of a body immersed in a fluid is the result of a countless number of forces and mutual interactions between body and fluid, and trying to take all these effects into account would yield a considerably involved model, which is not the purpose of this work. On the other hand, by oversimplifying the AUV hydrodynamic, the model would diverge from reality, becoming misleading and useless even for a theoretical study. A brief summary of the basic definitions is reported in Appendix A, while for an exhaustive treatment of the hydrodynamics concepts hereafter mentioned the reader is referred to [11, 12]). Thus the proposed model aims at a trade-off between complexity and accuracy; some widely adopted assumptions regarding the nature of the surrounding fluid are taken to be valid [12]. In particular, the flow is assumed to be inviscid, irrotational and incompressible, and therefore

2.3.3.1 Body added mass

The movement of a submerged body results in a displacement of a portion of the surrounding fluid, namely part of the fluid moves together with the body. This phenomenon can produce consequential effects on the submerged body dynamics, depending on its physics and geometry, hence it needs to be taken into account by modifying the mass and inertia tensor of the AUV [52].

In general, for every external force or torque applied to the body of the AUV, the added mass effect produces forces and torques with components in all the 3 axes

of the body frame (i.e. even along normal directions with respect to the applied force). Considering the general formulation of Newton-Euler equations, the added mass effect can be modeled as an additive component in the mass and inertia tensor and in the Coriolis matrix, thus Eqn. (2.7) can be rewritten as:

$$\left(\underbrace{\begin{bmatrix} mI & 0 \\ 0 & \mathcal{I} \end{bmatrix}}_{\triangleq \mathcal{M}_b} + \underbrace{\begin{bmatrix} M_{A1} & M_{A2} \\ M_{A3} & M_{A4} \end{bmatrix}}_{\triangleq \mathcal{M}_a} \right) \begin{bmatrix} \dot{\mathbf{v}}^b \\ \dot{\boldsymbol{\omega}}^b \end{bmatrix} + \underbrace{\begin{bmatrix} 0 & C_{A2} \\ C_{A2} & C_{A3} \end{bmatrix}}_{\triangleq \mathcal{C}_a} \begin{bmatrix} \mathbf{v}^b \\ \boldsymbol{\omega}^b \end{bmatrix} + \\ + \begin{bmatrix} \boldsymbol{\omega}^b \times m\mathbf{v}^b \\ \boldsymbol{\omega}^b \times \mathcal{I}\boldsymbol{\omega}^b \end{bmatrix} = \begin{bmatrix} \mathbf{f}^b \\ \boldsymbol{\tau}^b \end{bmatrix} \tag{2.15}$$

where $\mathcal{M}_a$ and $\mathcal{C}_a$ indicate respectively the added mass inertia and Coriolis tensors. Let $\mathcal{M}_a$ be defined as follows:

$$\mathcal{M}_a = \begin{bmatrix} m_{11} & m_{12} & \dots & m_{16} \\ m_{21} & \vdots & \dots & \vdots \\ \vdots & \vdots & \ddots & \vdots \\ m_{61} & \dots & \dots & m_{66} \end{bmatrix} \tag{2.16}$$

where m_{ij} represents the added mass coefficient in the *i-th* direction induced by an acceleration in the *j-th* direction. The evaluation of this $\mathbb{R}^{6\times6}$ matrix can be fairly complex, but, assuming that some simplifying hypotheses hold, then the number of coefficients to be evaluated can considerably decrease. First, the added mass inertia matrix is supposed to be symmetric [1], hence only 21 coefficients needs to be calculated; moreover, geometric symmetry further reduces the number of parameters: the shape of the AUV is for convenience modeled as a cylinder with two fins, as depicted in Fig. 2.2, thus both *x-z* and *x-y* are plane of symmetry for the body. Hence, due to *x-z* symmetry, for any linear combination of the acceleration along the x, z and ψ directions the induced force along y, ϕ and θ is zero, that is

$$m_{ij} = 0, \qquad i \in \{2, 4, 6\},\ j \in \{1, 3, 5\} \tag{2.17}$$

and in similar fashion, due to *x-y* symmetry,

$$m_{ij} = 0, \qquad i \in \{3, 4, 5\},\ j \in \{1, 2, 6\} \tag{2.18}$$

[1] This hypothesis is based on a potential flow assumption; for more details the reader is referred to [52]

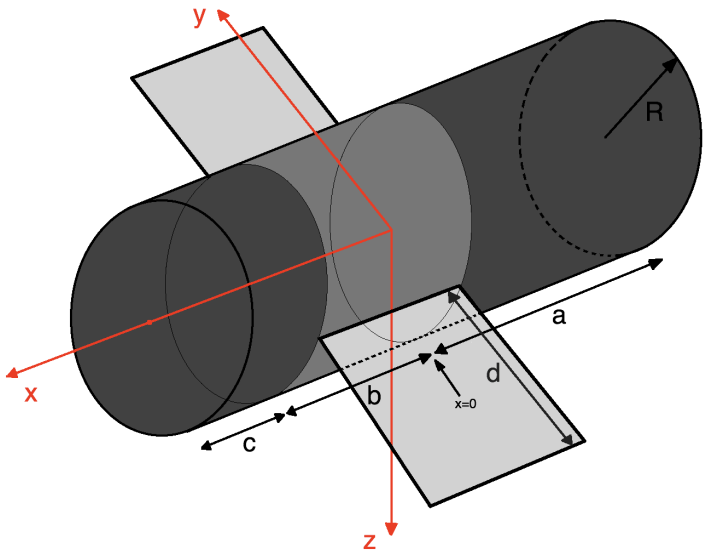

FIGURE 2.2: For the evaluation of added mass components the AUV body is approximated as a cylinder with radius R and two pectoral fins aligned with the center of mass; each fin is modeled as a flat plate with length d and width b.

The symmetric counterpart of these components should be zero as well, being $\mathcal{M}_a$ symmetric, hence only 10 components need to be actually evaluated, and the added mass matrix becomes:

$$\mathcal{M}_a = \begin{bmatrix} m_{11} & 0 & 0 & 0 & 0 & 0 \\ 0 & m_{22} & 0 & 0 & 0 & m_{26} \\ 0 & 0 & m_{33} & 0 & m_{35} & 0 \\ 0 & 0 & 0 & m_{44} & 0 & 0 \\ 0 & 0 & m_{53} & 0 & m_{55} & 0 \\ 0 & m_{62} & 0 & 0 & 0 & m_{66} \end{bmatrix} \tag{2.19}$$

Supposing the AUV is a slender body, i.e. its longitudinal length − among x axis − is appreciably larger than other dimensions, then strip theory can be applied to compute the 3-dimensional added mass coefficients m_{ij}. The key idea is to use the well known 2-dimensional added mass coefficients a_{ij} of simple 2D shapes and then integrate the result throughout the length of the body; according to slender body

theory $\mathcal{M}_a$ has the following structure

$$\begin{bmatrix} m_{11} & 0 & 0 & 0 & 0 & 0 \\ 0 & \int_B a_{22}(x)\,dx & 0 & 0 & 0 & \int_B -xa_{22}(x)\,dx \\ 0 & 0 & \int_B a_{33}(x)\,dx & 0 & \int_B xa_{33}(x)\,dx & 0 \\ 0 & 0 & 0 & \int_B a_{44}(x)\,dx & 0 & 0 \\ 0 & 0 & \int_B xa_{33}(x)\,dx & 0 & \int_B x^2a_{33}(x)\,dx & 0 \\ 0 & \int_B -xa_{22}(x)\,dx & 0 & 0 & 0 & \int_B x^2a_{22}(x)\,dx \end{bmatrix}$$

To explicitly compute the 2-D coefficients a_{ii}, the model illustrated in Fig. 2.2 is considered; three cylindrical sections with the same radius R compose the body, one of which has two fins attached along the horizontal plane. The two-dimensional added mass coefficients for the respective vertical sections, namely for a circle and for a finned circle (see Fig. 2.3) can be found in [12] and [52]:

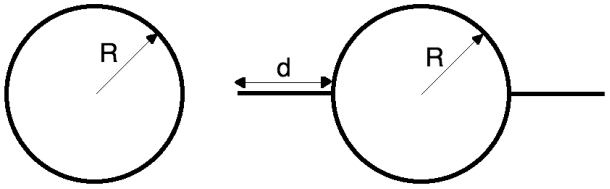

FIGURE 2.3: Vertical strips of the cylindrical (left) and finned (right) sections of the AUV body.

$$\begin{cases} a_{22} = \pi\rho R^2 \\ a_{33} = \pi\rho R^2 \\ a_{44} = 0 \end{cases} \tag{2.20}$$

$$\begin{cases} a_{22}^f = \pi\rho\left[R^2 + \left(\frac{d(2R+d)}{R+d}\right)^2\right] \\ a_{33}^f = \pi\rho R^2 \\ a_{44}^f = \frac{2}{\pi}(R+d)^4\left(\frac{\csc^4\alpha}{\pi}[2\alpha^2 - \alpha\sin 4\alpha + \frac{1}{2}\sin^2 2\alpha] - \frac{\pi}{2}]\right) \end{cases} \tag{2.21}$$

in which a_{44}^f is taken from [53], being $\sin\alpha = \frac{2R(d+R)}{R^2+(d+R)^2}$, and $\pi/2 < \alpha < \pi$. By summing the contributions of each section and properly integrating along body length

according to the structure of $\mathcal{M}_a$ reported above, it follows:

$$\begin{cases} m_{22} = -\int_a a_{22}\,dx + \int_b a^f_{22}\,dx + \int_c a_{22}\,dx \\ m_{26} = m_{62} = \int_a x a_{22}\,dx - \int_b x a^f_{22}\,dx - \int_c x a_{22}\,dx \\ m_{33} = -\int_a a_{33}\,dx + \int_b a^f_{33}\,dx + \int_c a_{33}\,dx \\ m_{35} = m_{53} = -\int_a x a_{33}\,dx + \int_b x a^f_{33}\,dx + \int_b x a_{33}\,dx \\ m_{44} = -\int_a a_{44}\,dx + \int_b a^f_{44}\,dx + \int_c a_{44}\,dx \\ m_{55} = -\int_a x^2 a_{33}\,dx + \int_b x^2 a^f_{33}\,dx + \int_c x^2 a_{33}\,dx \\ m_{66} = -\int_a x^2 a_{22}\,dx + \int_b x^2 a^f_{22}\,dx + \int_c x^2 a_{22}\,dx \end{cases} \tag{2.22}$$

Nevertheless slender body theory does not provide information about the x-direction added mass components; thus to evaluate m_{11} a different approach is required. A widely adopted technique is that of considering the AUV as an ellipsoid with length l_e and diameter d_e, and calculate the added mass coefficient as follows:

$$m_{11} = \frac{K\pi\rho l_e d_e^2}{6} \tag{2.23}$$

where K is an empirical function of the ratio l_e/d_e as depicted in Tab. 2.1.

l_e/d_e	1.00	1.50	2.00	2.51	2.99	3.99	4.99	6.01	6.97	8.01	9.02	9.97
K	.500	.305	.209	.156	.122	.082	.059	.045	.036	.029	.024	.021

TABLE 2.1: Empirical values for the parameter K as the ratio l_e/d_e varies. Courtesy of [52]).

The Coriolis added mass matrix $\mathcal{C}_a$ as defined in Eqn. (2.15) can be easily derived from $\mathcal{M}_a$: let the vectors $\mathbf{a} \in \mathbb{R}^3$ and $\mathbf{b} \in \mathbb{R}^3$ be defined as below:

$$\begin{bmatrix} \mathbf{a} \\ \mathbf{b} \end{bmatrix} = \mathcal{M}_a \begin{bmatrix} \mathbf{v}^b \\ \boldsymbol{\omega}^b \end{bmatrix} \tag{2.24}$$

and let the *hat* operator be defined, for a generic vector $\mathbf{v} = [v_1\ v_2\ v_3]^T$ as

$$\hat{\mathbf{v}} = \begin{bmatrix} 0 & -v_3 & v_2 \\ v_3 & 0 & -v_1 \\ -v_2 & v_1 & 0 \end{bmatrix} \tag{2.25}$$

Then $\mathcal{C}_a$ becomes

$$\mathcal{C}_a = \begin{bmatrix} 0 & C_{A2} \\ C_{A2} & C_{A3} \end{bmatrix} = \begin{bmatrix} 0 & \hat{\mathbf{a}} \\ \hat{\mathbf{a}} & \hat{\mathbf{b}} \end{bmatrix} \tag{2.26}$$

and its components C_{A2} and C_{A3} can be written explicitly as:

$$C_{A2} = \begin{bmatrix} 0 & -m_{33}w - m_{35}q & m_{22}v + m_{26}r \\ m_{33}w + m_{35}q & 0 & -m_{11}u \\ -m_{22}v - m_{26}r & m_{11}u & 0 \end{bmatrix}$$
$$C_{A3} = \begin{bmatrix} 0 & -m_{26}v - m_{66}r & m_{35}w + m_{55}q \\ m_{26}v + m_{66}r & 0 & -m_{44}p \\ -m_{35}w - m_{55}q & m_{44}p & 0 \end{bmatrix} \tag{2.27}$$

2.3.3.2 Control force and torque: fins hydrodynamics

Among all different kinds of actuators that have been proposed and employed to produce thrust in marine locomotion, propellers are perhaps the most popular; examples of propeller-driven vehicles are the MAYA AUV [54, 55] or the MARIUS AUV [22], in which the posterior propulsion is supported by a passive system of rudders, ailerons and elevators properly maneuvered for the attitude control. Propellers can also be used to actively generate a control torque, as for the AUV VideoRay [56], whose three thrusters perform along different axes an active control on the vehicle orientation. Modeling the thrust produced by propellers is relatively simple, since, to a first approximation, the correspondence between the propeller revolution rate and the force and torque produced is straightforward, and no complex hydrodynamic relations are involved [57].

Recently however the interest toward bio-inspired propulsion is greatly increased, chiefly due to the considerable maneuverability which can be achieved; though the unsteady hydrodynamics principles and the large variety of techniques employed by fish in fin- based propulsion and control maneuvers are fairly difficult to model, the good results attained in the development of such locomotion systems are promising [4, 58, 59].

This works focuses on the control of an AUV − modeled as a rigid body − propelled and controlled via one pair of pectoral fins and a caudal fin − modeled as rigid, two-dimensional hydrofoils −, therefore lifting surface theory is applied to derive the equations governing the interactions between fluid and fins, as well as forces and moments involved.

In particular, the tail fin is free to rotate about the vertical axis, whereas pectoral fins present a 2 degree-of-freedom motion, commonly referred to as feathering and lead-lag motion [60] (see Fig. 2.4).

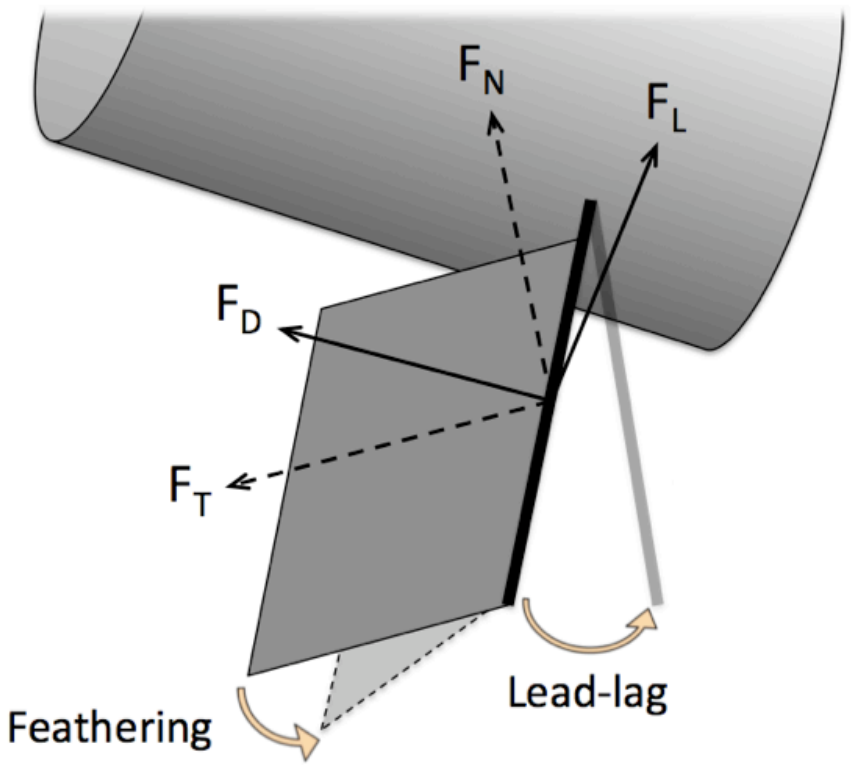

FIGURE 2.4: Particular of the right pectoral fin of the AUV, showing lead-lag (about the vertical axis) and feathering (about) motions.

For the sake of simplicity, every fin is supposed to have a large aspect ratio, therefore two-dimensional strip theory can be applied; the resulting forces are then integrated spanwise to get the total force acting on the fin.

Consider the model depicted in Fig. 2.4: traditionally the total force acting on the fin (i.e. the sum of the forces produced by each blade element) is supposed to act at the center of pressure of the fin, and it is divided into two orthogonal components; depending on the notation adopted these forces are referred to as *lift* and *drag* (respectively normal and tangential w.r.t. the flow stream) or *normal* and *tangential* forces (w.r.t. the surface of the fin). In this work the latter will be used for the evaluation of hydrodynamic forces. To locate the center of pressure of the fin the following formula can be used:

$$\hat{r}_{CP}^2 = \frac{\int_0^S c(r) r^2 \, dr}{S^2 A^2} \tag{2.28}$$

where $\hat{r}$ indicates the normalized center of pressure.

If steady-state assumption holds, then normal and tangent force components per unit length can be written as:

$$\begin{cases} F_N = \frac{1}{2} C_N(\alpha) \rho c U^2 \\ F_T = \frac{1}{2} C_T(\alpha) \rho c U^2 \end{cases} \tag{2.29}$$

where α denotes the hydrodynamic angle of attack, ρ the density of the fluid, c the chord length and U the velocity of the fin with respect to the fluid; C_N and C_T are the normal and tangential coefficients, which depend on the instantaneous angle of attack α. In airfoil theory these coefficients are usually linearized for small values of α; on the other hand, since we shall cope with greater angles of attack, a model empirically evaluated for insect wings will be adopted [37], assuming that its validity holds underwater. The coefficients, shown in Fig. 2.5 are calculated as follows:

$$\begin{cases} C_N(\alpha) = 3.4 \sin \alpha \\ \\ C_T(\alpha) = \begin{cases} 0.4 \cos^2(2\alpha) & \text{for } 0 \leq \alpha \leq \pi/4 \\ 0 & \text{otherwise} \end{cases} \end{cases} \tag{2.30}$$

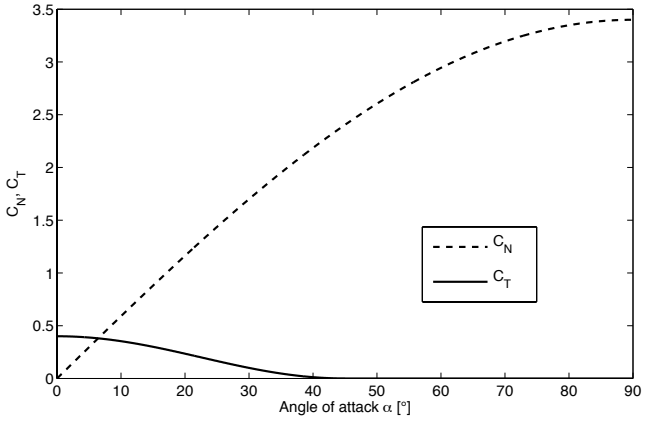

FIGURE 2.5: Normal and tangential adimensional coefficients experimentally obtained in [37].

According to 2-D hydrofoil theory, the total force acting on each fin blade is equal to

$$\begin{cases} dF_N(t,r) = \frac{1}{2} C_N(\alpha(t)) \rho c(r) U^2(t,r) dr \\ dF_T(t,r) = \frac{1}{2} C_T(\alpha(t)) \rho c(r) U^2(t,r) dr \end{cases} \tag{2.31}$$

and, by integrating the above relation along the span length, one gets:

$$\begin{cases} F_N(t,r) = \int_0^S dF_N(t,r)dr = \frac{1}{2}\rho A C_N(\alpha(t)) U_{CP}^2(t) \\ F_T(t,r) = \int_0^S dF_T(t,r)dr = \frac{1}{2}\rho A C_T(\alpha(t)) U_{CP}^2(t) \end{cases} \tag{2.32}$$

being S the span length, A the area of the fin and U_{CP} the fin velocity at its center of pressure with respect to the flow stream.

With no much effort lift and drag forces can be evaluated from F_N and F_T, through the trigonometric function of the instantaneous angle of attack α, as reported below:

$$\begin{cases} F_L(t) = F_N(t)\cos(\alpha(t)) - F_T(t)\sin(\alpha(t)) \\ F_D(t) = F_N(t)\sin(\alpha(t)) + F_T(t)\cos(\alpha(t)) \end{cases} \tag{2.33}$$

Consider now the two pectoral fins, and suppose that the following assumptions hold:

- The two fins have identical rectangular shape of length S (spanwise) and width C (chordwise), and are symmetrically placed in body frame with respect to the vertical plane $y^b = 0$.
- The stroke plane is horizontal with respect to the body frame, parallel to the plane $z^b = 0$.
- The bases of the two fins lie in the same point, vertically aligned with the AUV center of mass, and which corresponds to the origin of the right-handed reference frame $\{\mathcal{F}\}$, as shown in Fig. 2.6; therefore the two fins rotate about the same axis z^f.

For the sake of clarity superscript indices will be used to designate the corresponding reference frame (namely, ^{s} will be used for the inertial frame $\{\mathcal{S}\}$, ^{b} for the body frame $\{\mathcal{B}\}$ and ^{f} for the pectoral fins frame $\{\mathcal{F}\}$). By applying Eqn. (2.28) one finds that the center of pressure is placed at a distance equal to

$$r_{CP} = \frac{1}{\sqrt{3}} S \tag{2.34}$$

from the origin of $\{\mathcal{F}\}$. If the AUV swims in a still fluid (i.e. flow velocity at infinite distance from the AUV is zero), then the velocity of the center of pressure of the fins U_{CP} relative to the fluid depends only on the angular velocity of the fin and on the body velocity; for the attitude stabilization it can be assumed that the body velocity is sufficiently small compared to the velocity of the fins at their center of pressure,

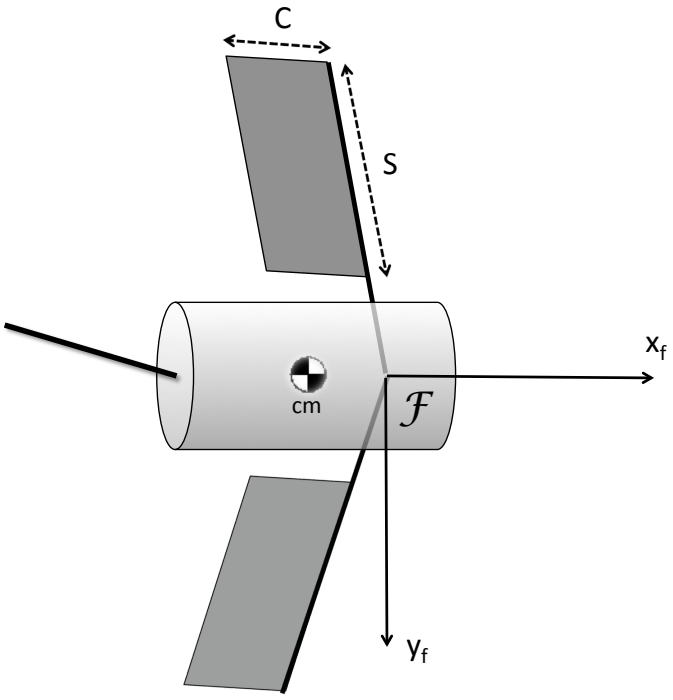

FIGURE 2.6: Top view of the AUV: the reference frame $\{\mathcal{F}\}$ can be obtained by translating $\{\mathcal{B}\}$ from the center of mass to the bases of the two fins (z_f axis pointing downward).

and therefore it can be neglected. Accordingly, U_{CP} can be written as

$$U_{CP} = \hat{r}_{CP} S \dot{\beta}(t) \tag{2.35}$$

Clearly this assumption no longer holds for cruising speeds; in this case a different approach is required, and Eqn. (2.35) should be substituted with

$$U_{CP} = \hat{r}_{CP} S \dot{\beta}(t) + v_b^f \tag{2.36}$$

where v_b^f represents the body velocity relative to the space frame, written in the fin coordinate system. Nevertheless, at such speeds hydrodynamic stability becomes a more important issue than maneuverability, therefore the considered feathering and lead-lag motion would be less effective. In fact the boxfish, when cruising at high speed gaits, folds every fin and exploits the intrinsic stability of its shape and self-correcting vortices, using the only tail fin to produce thrust. Hence maneuvering via pectoral fins will be hereafter considered for low speeds of the AUV (compared to the velocity of the fin at its center of pressure).

Now let $\mathbf{f}_p^f$ and $\boldsymbol{\tau}_p^f$ be, respectively, the total force and torque expressed in $\{\mathcal{F}\}$; since lift and drag forces can be readily evaluated via Eqn. (2.33), then it is possible to write explicitly $\mathbf{f}_p^f$ and $\boldsymbol{\tau}_p^f$ as follows:

$$\begin{cases} \mathbf{f}_p^f &= \begin{bmatrix} -F_{D,\ell}\cos\beta_\ell - F_{D,r}\cos\beta_r \\ F_{D,\ell}\sin\beta_\ell - F_{D,r}\sin\beta_r \\ -F_{L,\ell} - F_{L,r} \end{bmatrix} \\ \boldsymbol{\tau}_p^f &= \hat{r}_{CP} S \begin{bmatrix} F_{L,\ell}\cos\beta_\ell - F_{L,r}\cos\beta_r \\ -F_{L,\ell}\sin\beta_\ell - F_{L,r}\sin\beta_r \\ -F_{D,\ell} + F_{D,r} \end{bmatrix} \end{cases} \tag{2.37}$$

where the subscript indices $_\ell$ and $_r$ stand for left and right fin. The last step is to write the above forces and torques in body frame; as $\{\mathcal{F}\}$ and $\{\mathcal{B}\}$ have the same orientation, the rotation matrix between the two frames is the identity $I \in \mathbb{R}^{3\times3}$, consequently $\mathbf{f}_p^b$ and $\boldsymbol{\tau}_p^b$ can be written as:

$$\begin{bmatrix} \mathbf{f}_p^b \\ \boldsymbol{\tau}_p^b \end{bmatrix} = \begin{bmatrix} I & 0 \\ \hat{\mathbf{r}}_{CM} & I \end{bmatrix} \begin{bmatrix} \mathbf{f}_p^f \\ \boldsymbol{\tau}_p^f \end{bmatrix} \tag{2.38}$$

where $\mathbf{r}_{CM}$ is the center of mass of the AUV expressed in $\{\mathcal{F}\}$ coordinates.

As regarding the tail fin, its different purpose and functioning require a different model to be considered. In literature, the efficiency of vehicles propelled by oscillating foils is a widely studied issue: an overview of different kinds of fish-like propulsion systems is outlined by Tzeranis *et al.* in [61], while the common dual link, carangiform-like tailfin model is discussed, e.g., in [25, 26, 62, 63] and in [64].

In the present work, a simpler model is considered, with one degree of freedom represented by the geometric angle θ between the fin plate and the x-axis, as shown in Fig. 2.7 (an exaustive overview of tail fin's principal parameters can be found in the work by Anderson *et al.* [65]). Although the tail fin can be used as a rudder to control the yaw angle (e.g., by using its mean angle as control variable), in the present work the only purpose assigned to the tail fin is the production of forward thrust, thus its model is calculated accordingly.

First, let us consider two right-handed reference frames: the body fixed frame $\mathcal{B}$, whose origin is at the center of mass of the vehicle, and the tail fin reference frame

$\mathcal{T}$, which has the same orientation as $\mathcal{B}$ and whose origin is at the joint of the tail fin. Thus it rotates about the z_t axis, which is pointing inside the page, and positive angles θ are clockwise, according to the right handedness of $\mathcal{T}$; now consider the model sketched in Fig. 2.7: let U_∞ be the flow speed at an infinite distance from the

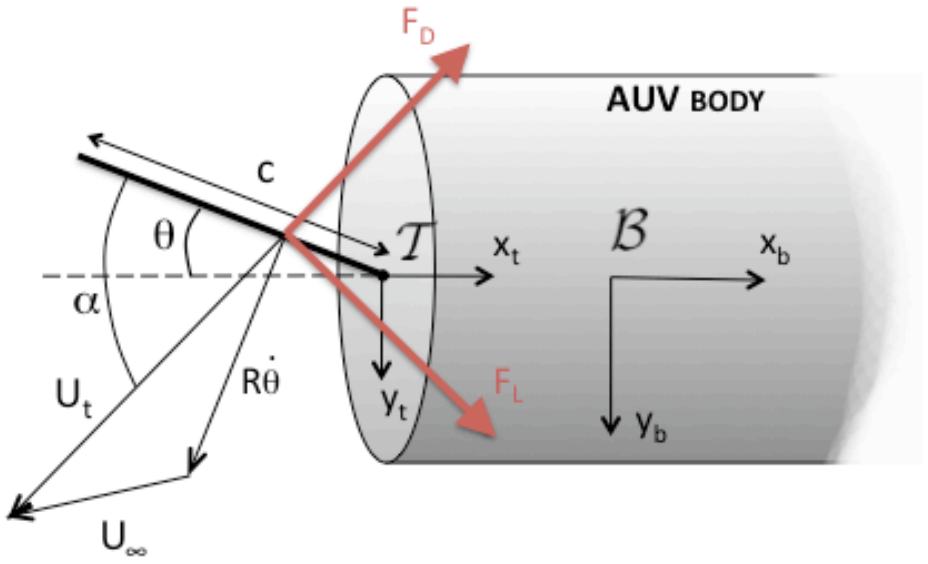

FIGURE 2.7: A top view of the tailfin highlighting its geometrical parameters: the fin orientation θ w.r.t. $\mathcal{T}$, the hydrodynamic angle of attack α, fin velocity U_t and its chord length c.

AUV, and U_t the total velocity of the fin with respect to the flow, defined as the sum of fin's normal velocity $R\dot{\theta}$ at its quarter chord point and U_∞; let then α denote the hydrodynamic angle of attack, that is, the angle between total fin velocity U_t and the x_t axis, positive clockwise. The angle θ, as previously stated, denotes the orientation of the fin w.r.t. both fin and body reference frames.

As traditionally done in hydrofoil theory, force modeling is considered at the quarter chord point of the foil; in particular, the total force generated by the interaction between the moving fin and the surrounding fluid can be written as the sum of lift (F_L) and drag (F_D) components (respectively perpendicular and in line with the the total velocity vector U_t), described, according to [66], by the relations below:

$$\begin{cases} F_L = \frac{1}{2}\rho A U_t^2 C_{L\,max} \sin 2\alpha \\ F_D = \frac{1}{2}\rho A U_t^2 C_{D\,max}(1 - \cos 2\alpha) \end{cases} \tag{2.39}$$

where ρ is the density of the fluid, A is the fin area and $C_{L\,max}$, $C_{D\,max}$ are, respectively, the maximum lift and drag coefficients, which varies as function of the geometric angle of attack α as shown in Fig. 2.8. Since we are mainly interested in

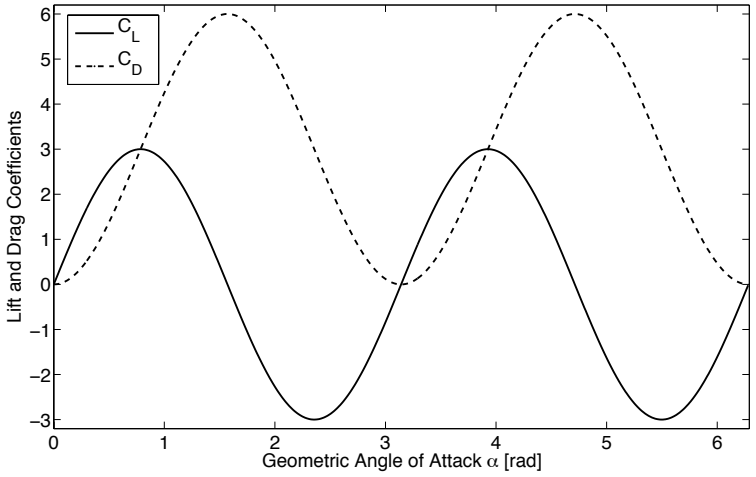

FIGURE 2.8: Lift and drag coefficients as function of the angle of attack α.

the expression of hydrodynamic forces with respect to body fixed frame, lift and drag are to be rewritten in axial coordinates, through the following trigonometric function of fin orientation θ:

$$\begin{cases} F_x = F_D \cos\xi + F_L \sin\xi \\ F_y = F_L \cos\xi - F_D \sin\xi \end{cases} \tag{2.40}$$

where the angle ξ is defined as $\xi \triangleq \alpha - \theta$. The joint at the basis of the fin is actuated in a harmonic fashion with the following kinematics:

$$\theta(t) = \theta_0 + A_t \sin 2\pi f_t t \tag{2.41}$$

As a result, since the states θ, $\dot{\theta}$ are known at any time, it is possible through Eqn. 2.39 to compute the lift and drag produced by the tail fin. In order to fit these forces into the overall model, we shall rewrite these relations in terms of force and momentum generated at the center of mass of the vehicle: let $\mathbf{r}_t$ be the vector expressing the origin of $\mathcal{T}$ in $\mathcal{B}$ coordinate system, and assume that the tail fin joint is in the x_b-z_b plane (i.e. $\mathbf{r}_t = [x_t\ 0\ z_t]$); then the total force $\mathbf{f}_t^b$ and momentum $\boldsymbol{\tau}_t^b$ applied at the

center of mass of the AUV is given by the following set of equations:

$$\begin{cases} \mathbf{f}_t^b = \begin{bmatrix} F_D \cos\xi + F_L \sin\xi \\ F_L \cos\xi - F_D \sin\xi \\ 0 \end{bmatrix} \\ \boldsymbol{\tau}_t^b = \mathbf{r}_t \times \mathbf{f}_t^b = \begin{bmatrix} -(F_L \cos\xi - F_D \sin\xi) z_t \\ (F_D \cos\xi + F_L \sin\xi) z_t \\ (F_L \cos\xi - F_D \sin\xi) x_t \end{bmatrix} \end{cases} \tag{2.42}$$

The model presented is rather simple, but suitable for the purpose of this work; nevertheless, the reader interested in the flapping foil thrust efficiency issue can find a flourishing literature about the subject. In particular, one of the major developments in flapping foil propellers concerns the flexibility of the fins, which recently turned out to be a prolific research field. The relation between flexibility and efficiency in tailfin-propelled vehicles has been analyzed by Chaithanya and Venkatraman in [67], where the thrust coefficient and the efficiency are presented by introducing in the hydrodynamics equations the equation of motion of the deformable beam. Experimental results to prove the efficiency are presented in [69] and [41].

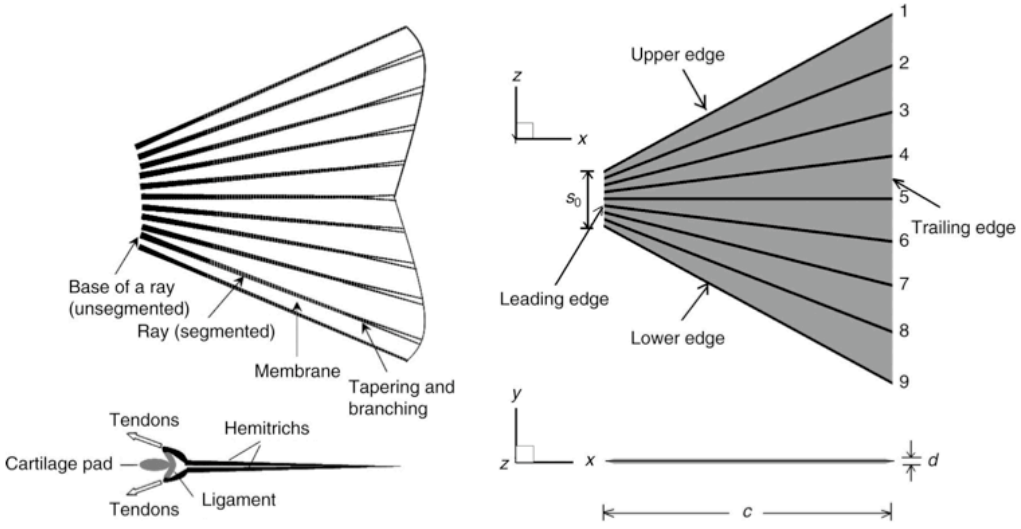

FIGURE 2.9: Many fishes can actively control their fins through tendon-controlled flexible rays, and this greatly increases their efficiency and maneuverability. Courtesy of [68].

2.3.3.3 Body drag

As stated in the previous section, the resistance exerted by the fluid to the motion of the AUV depends in a somehow complex way on the velocity of the body, besides other parameters. The general formula which describes the total drag force acting on a moving submerged body is the following:

$$\mathbf{f}_d = \frac{1}{2} C_d A \rho \, |\mathbf{v}_{bf}|^2 \tag{2.43}$$

being C_d the drag coefficient, A the area of the cross section of the body perpendicular to the flow, ρ the density of the fluid and v_r the relative speed of the body with respect to the fluid. As regards the equation which governs the drag force (2.43), the evaluation of the drag coefficient C_d (and therefore of the related force and torque) in a suitable form to be fit in the Newton-Euler equations can be a complex issue. To overcome this problem some considerations about the drag coefficient behavior at different Reynolds numbers needs to be done. At very low Reynolds numbers (namely, for $Re < 1$), C_d is almost inversely proportional to the velocity of the body, and, by substituting this relation in Eqn. (2.43), one finds that the drag force exerted on the body is approximately proportional to its velocity:

$$\mathbf{f}_d \approx k\mathbf{v} \tag{2.44}$$

On the other hand, at high Reynolds number regime, the drag coefficient remains approximately constant, thus the resulting drag force becomes:

$$\mathbf{f}_d \approx \underbrace{\frac{1}{2} C_d A \rho}_{constant} |\mathbf{v}|^2 \tag{2.45}$$

Thus, according to Eqn. (2.44) and Eqn. (2.45), drag force can be decomposed in the three linear and angular directions as follows:

$$\begin{cases} \mathbf{f}_d^b = K_v \mathbf{v}^b + K_{v|v|} |\mathbf{v}^b| \mathbf{v}^b \\ \boldsymbol{\tau}_d^b = K_\omega \boldsymbol{\omega}^b + K_{\omega|\omega|} |\boldsymbol{\omega}^b| \boldsymbol{\omega}^b \end{cases} \tag{2.46}$$

where $K_v = diag\{k_u, k_v, k_w\}$, $K_\omega = diag\{k_p, k_q, k_r\}$, $K_{v|v|} = diag\{k_{u|u|}, k_{v|v|}, k_{w|w|}\}$ and $K_{\omega|\omega|} = diag\{k_{p|p|}, k_{q|q|}, k_{r|r|}\}$ are appropriate constant matrices, with the values k_i representing the linear drag component, and $k_{i|i|}$ referred to as the quadratic drag component.

2.3.4 Kinematic equations

Since external forces and torques depend on Euler angles ϕ, θ and ψ, in order to solve (2.10) and evaluate AUV dynamics, the following relation, which governs $(\mathbf{b}, R) \in SE(3)$, is needed:

$$\begin{cases} \dot{R} = R\hat{\boldsymbol{\omega}}^b \\ \dot{\mathbf{b}} = R\mathbf{v}^b \end{cases} \tag{2.47}$$

where $\hat{\cdot}$ indicates the *hat* operator, which can be thought of as an isomorphism which maps any vector $\mathbf{v} = [v_1\ v_2\ v_3]^T$ from $\mathbb{R}^3$ to $\mathfrak{so}(3)$, the Lie algebra associated to $SO(3)$, as follows:

$$\hat{\cdot}, \mathbf{v} : \mathbb{R}^3 \longrightarrow \mathfrak{so}(3) : \begin{bmatrix} v_1 \\ v_2 \\ v_3 \end{bmatrix} \longrightarrow \begin{bmatrix} 0 & -v_3 & v_2 \\ v_3 & 0 & -v_1 \\ -v_2 & v_1 & 0 \end{bmatrix} \triangleq \hat{\mathbf{v}} \tag{2.48}$$

Besides Eqn. (2.47), there exists a linear relation between space frame and body frame angular rates, which can be expressed via the $W_{\mathcal{SB}}$ matrix transformation as follows:

$$\begin{bmatrix} \dot{\phi} \\ \dot{\theta} \\ \dot{\psi} \end{bmatrix} = W_{\mathcal{SB}} \begin{bmatrix} p \\ q \\ r \end{bmatrix} = \begin{bmatrix} 1 & \sin\phi\tan\theta & \cos\phi\tan\theta \\ 0 & \cos\phi & -\sin\phi \\ 0 & \frac{\sin\phi}{\cos\theta} & \frac{\cos\phi}{\cos\theta} \end{bmatrix} \begin{bmatrix} p \\ q \\ r \end{bmatrix} \tag{2.49}$$

This relation can also be inverted, obtaining

$$\begin{bmatrix} p \\ q \\ r \end{bmatrix} = W_{\mathcal{BS}} \begin{bmatrix} \dot{\phi} \\ \dot{\theta} \\ \dot{\psi} \end{bmatrix} \tag{2.50}$$

where

$$W_{\mathcal{BS}} = W_{\mathcal{SB}}^{-1} = \begin{bmatrix} 1 & 0 & -\sin\theta \\ 0 & \cos\phi & \sin\phi\cos\theta \\ 0 & -\sin\phi & \cos\phi\cos\theta \end{bmatrix} \tag{2.51}$$

A final remark about the Euler angles representation: 3-dimensional representations of $SO(3)$ indeed always presents a singularity, thus they should be trated as only local parameterizations, with no global character. Euler angles (ZYX, as defined in Eqn. (2.4)) are not an exception: rotation matrix R becomes singular for $\theta = \pm\pi/2$, thus some complications in the angular position conversions (namely, from

R to Euler angles) there exist. On the other hand, during usual maneuvers or standard testing operations, the AUV pitch angle seldom reaches a vertical orientation, therefore, at least in the present work, the singularity in Euler angles representation can be neglected. For practical applications where more robustness is required, then a different representation, such as quaternions, should be adopted.

2.3.5 The dynamic model

Now that the governing equations for all the forces and torques acting on the AUV have been written explicitly, it is possible to derive the extended Newton-Euler dynamic equation:

$$\mathcal{M}\begin{bmatrix}\dot{\mathbf{v}}^b\\ \dot{\boldsymbol{\omega}}^b\end{bmatrix}+\Big(\mathcal{C}_a-\mathcal{D}_L\Big)\begin{bmatrix}\mathbf{v}^b\\ \boldsymbol{\omega}^b\end{bmatrix}+\begin{bmatrix}\boldsymbol{\omega}^b\times m\mathbf{v}^b\\ \boldsymbol{\omega}^b\times\mathcal{I}\boldsymbol{\omega}^b\end{bmatrix}-\mathcal{D}_Q\begin{bmatrix}|\mathbf{v}^b|\,\mathbf{v}^b\\ |\boldsymbol{\omega}^b|\,\boldsymbol{\omega}^b\end{bmatrix}= \begin{bmatrix}(m-\rho V)R^T\mathbf{g}\\ \mathbf{x}_b\times\rho VR^T\mathbf{g}\end{bmatrix}+\begin{bmatrix}I & 0\\ \hat{\mathbf{r}}_{CM} & I\end{bmatrix}\begin{bmatrix}\mathbf{f}_p^f(\alpha,\beta,\dot{\beta})\\ \boldsymbol{\tau}_p^f(\alpha,\beta,\dot{\beta})\end{bmatrix} \tag{2.52}$$

being $\mathcal{M}=\mathcal{M}_b+\mathcal{M}_a$ the mass and inertia matrix (including added mass), and $\mathcal{D}_L$ and $\mathcal{D}_Q$ respectively the linear and quadratic drag coefficient matrices.

For control purposes the dynamic equations are often decoupled and then linearized around a set point, assuming to operate on a plane (i.e. on the diving plane or on the steering plane); if we suppose that the preceding hypotheses regarding the vehicle symmetry and buoyancy hold, then it is possible from Eqn. (2.52) to derive the following relations for the diving and steering plane dynamics[2].

2.3.5.1 Diving plane dynamics

Considering the AUV to be free to move in the diving plane only (with respect to body frame $\mathcal{B}$), then the state variables v, r and p are identically zero; also, let the forward speed u be fixed to a constant positive value U, then it is possible to rewrite the dynamic − derived from Eqn. (2.52) − and kinematic − derived from Eqn. (2.47)

[2]The only further assumption to simplify equations is that the center of buoyancy lies in the z axis, and therefore $x_b=0$.

− equations for the vehicle as follows:

$$Dynamics \begin{cases} (m+m_{33})\dot{w} + m_{35}\dot{q} &= k_w w + (m-m_{11})Uq + f_{p,z} \\ (I_y+m_{55})\dot{q} + m_{35}\dot{w} &= k_q q + (m_{11}-m_{33})Uw - m_{35}Uq + \\ & \qquad -\rho V g z_b \sin\theta + \tau_{p,\theta} \end{cases} \tag{2.53}$$

$$Kinematics \begin{cases} \dot{z} &= -U\sin\theta + w\cos\theta \\ \dot{\theta} &= q \end{cases} \tag{2.54}$$

where m_{ij} represent the added mass components, ρ denotes the fluid density, V is the AUV volume, g is the gravitational force (scalar), z_b the z component of the center of buoyancy (in body frame) and $f_{p,z}$ and $\tau_{p,\theta}$ are, respectively, the force and torque applied on the AUV due to the pectoral fin motion and interaction with the surrounding fluid. Now let $\mathbf{x}_d$ be the state vector, defined as:

$$\mathbf{x}_d = \begin{bmatrix} w \\ q \\ z \\ \theta \end{bmatrix} \tag{2.55}$$

and let us consider, at first, the system being directly actuated by the control force and torque $f_{p,z}$ and $\tau_{p,\theta}$ (that is, the control input is $\mathbf{u}(t) = [f_{p,z}\ \tau_{p,\theta}]^T$); then the system described by Eqs. (2.53−2.54) can be linearized around the equilibrium point $\mathbf{x}_0 = [0\ 0\ 0\ 0]^T$; as a result, the linear system $\Sigma_d = \{F_d, G_d, H_d\}$ is obtained:

$$\begin{cases} \dot{\mathbf{x}}_d = F_d\mathbf{x}_d + G_d\mathbf{u} \\ \mathbf{y}_d = H_d\mathbf{x}_d \end{cases} \tag{2.56}$$

in which matrices F_d, G_d and H_d are readily computed from (2.53) and (2.54). By substituting the physical parameters with the ones derived for the boxfish model, the eigenvalues for the state space matrix F_d take the following values:

$$\lambda_i = \begin{bmatrix} 0 \\ -1.659 + 2.928j \\ -1.659 - 2.928j \\ -0.190 \end{bmatrix} \tag{2.57}$$

Although the position of the poles in the complex plane is influenced by a large number of parameters, some basic facts hold regardless of the variation of these parameters in a wide range; in particular, the presence of a pole in zero makes the overall system not BIBO stable, and, therefore, the design of a controller to restore stability is required. As regards the other three poles, one is real negative, the others

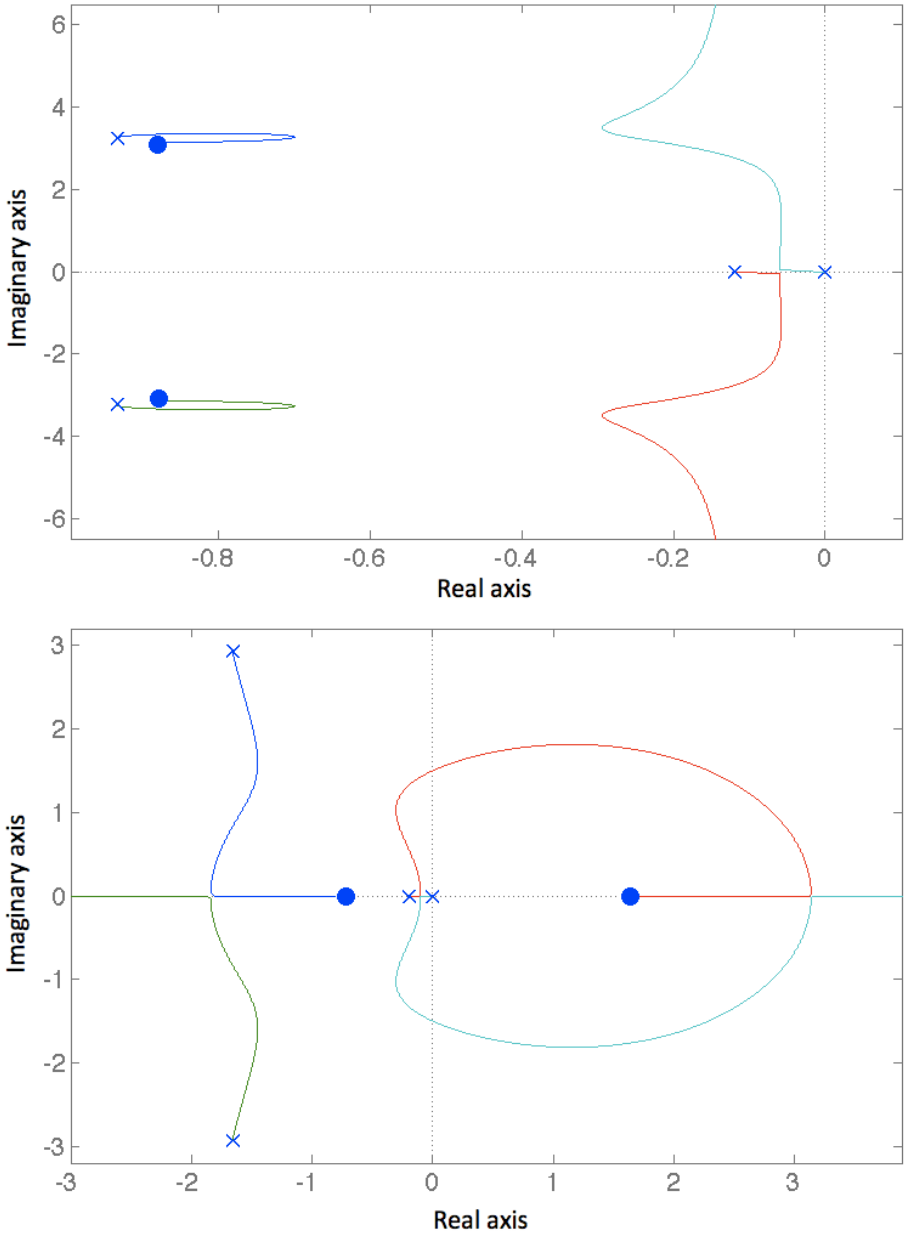

FIGURE 2.10: Root locus of the linear system Σ_d for transfer function $\mathbf{y} - f_{p,z}$ (*top*) and for transfer function $\mathbf{y} - \tau_{p,\theta}$ (*bottom*).

become complex conjugated above a certain value of the forward speed U[3]. Fig. 2.10 shows the root loci of the considered linear system for the transfer functions between the vehicle's depth z and the two inputs $f_{p,z}$ and $\tau_{p,\theta}$.

2.3.5.2 Steering plane dynamics

In a similar fashion, the steering plane dynamic model can be calculated from (2.52); first, consider the following sets of equations describing the dynamic and kinematic behavior of the AUV in the steering plane (again, we assume that the preceding hypotheses hold, and that the forward speed − i.e. along the x direction − is fixed at the constant value U):

$$Dynamics \begin{cases} (m+m_{22})\dot{v}+m_{26}\dot{r} &= k_v v+(m_{11}-m)Ur+f_{p,v} \\ (I_{zz}+m_{66})\dot{r}+m_{26}\dot{v} &= k_r r+(m_{22}-m_{11})Uv+ \\ & \quad +m_{26}Ur+\tau_{p,\psi} \end{cases} \tag{2.58}$$

$$Kinematics \begin{cases} \dot{y} &= U\cos\psi - v\sin\psi \\ \dot{\psi} &= r \end{cases} \tag{2.59}$$

In this case, velocities w, p and q are considered identically zero, and the 4th order linear system derived from Eqs. (2.58−2.59) can be written in the form:

$$\begin{cases} \dot{\mathbf{x}}_s = F_s\mathbf{x}_s + G_s\mathbf{u} \\ \mathbf{y}_s = H_d\mathbf{x}_s \end{cases} \tag{2.60}$$

where state variable $\mathbf{x}_s$ and control input $\mathbf{u}$ are defined as follows:

$$\mathbf{x}_s = \begin{bmatrix} v \\ r \\ y \\ \psi \end{bmatrix} \qquad \mathbf{u} = \begin{bmatrix} f_{p,v} \\ t_{p,\psi} \end{bmatrix} \tag{2.61}$$

As a result, linear control techniques can be applied to stabilize the AUV orientation: for instance, Maurya *et al.* in [55] adopt a LQR method, by including in the cost function depth z and its integral $\int z$, and present good results for depth

[3]In the present simulation, forward speed U was set to 0.3m/s, a fair value for a typical cruising mode.

control both in simulation and practical application. In [70] the dynamics of the tracking error is used to stabilize the vehicle on the desired trajectory.

Further examples of generic AUV steering and diving plane models can be found in [71–75] where nonlinear control techniques are adopted.

Chapter 3

Attitude estimation and control

3.1 Attitude estimation via sensor fusion

Estimating a vehicle's orientation is a central issue both for UUV and for UAV control, but not an easy task to perform. Often the readouts from the sensors are too noisy to provide useful information about the vehicle's attitude and orientation; moreover many kinds of sensors commonly used for this purpose (e.g. gyroscopes or accelerometers), even if properly calibrated, are not suitable to provide any kind of angular or linear position by integration, since even a small offset in the readouts would result in a positional drift, making the estimation totally useless. For these reasons our approach towards attitude estimation is based on sensor fusion, i.e. on the fusion of redundant information about the same variable from different sensors [45].

Again, this technique is widely adopted in nature, among many kinds of flying and swimming animals. It follows a summary of the basic sensors employed in nature and the artificial devices inspired by them.

- *eyes*: sight is the most important source of information regarding position and orientation, at least among shallow-waters dwellers. In artificial vehicles visual information is important as well, and therefore different kinds of cameras (e.g., digital cameras, infrared cameras, light polarization sensors, etc.) are often mounted onboard for several purposes such as attitude estimation (through the horizon line, for instance), obstacle identification, or to collect and transmit information about visited places.

- *halteres*: a sensory organ often employed by insects to detect gyroscopic forces and evaluate body orientation accordingly. They are placed behind the wings, and composed by several mechanoreceptors to detect angular rotations, by oscillating in counter phase with respect to wings (for more information see [76] and the references found therein). By processing the information collected from these sensors it is possible to compute the angular velocity $\boldsymbol{\omega}$, which is artificially obtained through the use of gyroscopes.

- *lateral line system*: a very common sense organ among fishes[1], used for various purposes, such as hearing, touch, temperature, electrical and magnetic field perception as well as equilibrium and balancing aid.

- *inner ears*: used by fishes both for hearing sounds and for perceiving angular acceleration and gravity, for equilibrium and balancing.

This approach can be successfully adopted in AUV control as well, as shown in the next sections, by equipping the vehicle with a similar sensor suite. In particular, we demonstrate how a sensor suite composed by gyroscopes, accelerometers and magnetic sensors can be successfully used to produce a highly reliable and precise attitude estimation for any kind of flying or swimming vehicle.

3.1.1 The sensor fusion algorithm

The filter implemented for the robotic fish attitude estimation is based on the work by Campolo *et al.*, who in [45] demonstrated that using the gyroscopes readouts $\boldsymbol{\omega}_{gyr} \in \mathbb{R}^3$ and the readings of at least two other independent vectors $\mathbf{v}_i \in \mathbb{R}^3$ (e.g. gravity and earth magnetic field) it is possible to asymptotically track $R(t)$ through the following observer:

$$\begin{cases} \dot{R}^* &= R^* \hat{\boldsymbol{\omega}}^* \\ \boldsymbol{\omega}^* &= \boldsymbol{\omega}_{gyr} + \sum_{i=1}^{N} k_i (\mathbf{v}_i \times \mathbf{v}_i^*) \\ \mathbf{v}_i^* &= R^{*T} \mathbf{v}_{0i} \end{cases} \tag{3.1}$$

where k_i are the filter gains and $\mathbf{v}_{0i} \in \mathbb{R}^3$ is the representation in space frame $\{\mathcal{S}\}$ of the vector field object of measurement (therefore $\mathbf{v}_{0i}$ is a known, time-invariant vector). The block diagram of the observer is shown in Fig. 3.1.

[1] It consists of a series of fluid-filled canals, running lengthwise down each side of fish's body. In *Teleostei* these canals are placed just below the skin, communicating with the surrounding environment via canal pores.

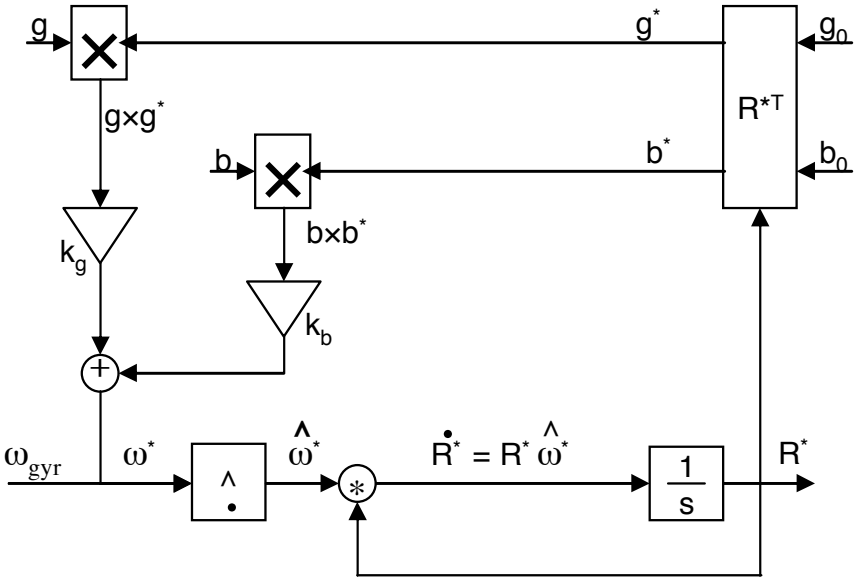

FIGURE 3.1: Block diagram of the estimator (taken from [45]).

3.1.1.1 Numerical Implementation

The numerical errors introduced in the discrete time implementation of the algorithm could drive $R^*(k+1)$ away from the space $SO(3)$; to avoid this, Rodrigues' formula [51] has been adopted for the evaluation of the rotation matrix $R^*(k+1)$:

$$\begin{cases} \boldsymbol{\omega}^*(k) &= \boldsymbol{\omega}_{gyr}(k) + \sum_{i=1}^{N} k_i(\mathbf{v}_i(k) \times R^{*T}(k)\mathbf{v}_{0i}) \\ \alpha(k) &= \sin\|\Delta T\widehat{\boldsymbol{\omega}}^*(k)\| \,/\, \|\Delta T\widehat{\boldsymbol{\omega}}^*(k)\| \\ \beta(k) &= (1-\cos\|\Delta T\widehat{\boldsymbol{\omega}}^*(k)\|) \,/\, \|\Delta T\widehat{\boldsymbol{\omega}}^*(k)\|^2 \\ R^*(k+1) &= R^*(k)\left(I + \alpha(k)\Delta T\widehat{\boldsymbol{\omega}}^*(k) + \beta(k)\Delta T^2\widehat{\boldsymbol{\omega}}^{*2}(k)\right) \end{cases} \tag{3.2}$$

where ΔT is the sampling interval.

The matrix $R^T(t)R^*(t)$ is guaranteed to converge to the identity matrix I for any suitable initial condition, i.e. the estimated orientation $R^*(t)$ converges to the true orientation $R(t)$.

3.1.2 Simulation results

The AUV model proposed in §2.3.5 was implemented in Matlab to compute the dynamics of the vehicle and the corresponding hydrodynamic forces; as for the attitude estimation, three independent sensors are considered: a 3-axis gravitomer which

measures the gravity vector[2] components with respect to the body frame, a 3-axis magnetometer which measures the geomagnetic field vector[3], and a 3-axis gyroscope which measures the angular velocity vector. In order to obtain a realistic set of data from the sensors, readouts from gravitometer, magnetometer and gyroscope are simulated as follows:

$$\begin{aligned} \boldsymbol{\omega}_{gyro} &= \boldsymbol{\omega}(t) + \mathbf{w}_1(t) \\ \mathbf{g}_{meas}(t) &= P(s)R^T(t)\mathbf{b}_0 + \mathbf{w}_2(t) \\ \mathbf{b}_{meas}(t) &= R^T(t-\tau_d)\mathbf{g}_0 + \mathbf{w}_3(t) \end{aligned} \tag{3.3}$$

where $\boldsymbol{\omega}(t)$ and $R(t)$ obey to Eqn. (3.9), $\mathbf{w}_i(t) \in \mathbb{R}^3$ are zero-mean independent additive gaussian noises with variance $\sigma_1^2 = 0.6$, $\sigma_2^2 = \sigma_3^2 = 0.2$. With a little abuse of notation we indicate with $\mathbf{z}(t) = P(s)\mathbf{y}(t)$ the filtered version of the signal $\mathbf{y}(t)$ where $P(s)$ is the transfer function of a second order low-pass filter which models the dynamics of the accelerometers inside the gravitometer:

$$P(s) = \frac{\omega_n^2}{s^2 + 2\xi\omega_n s + \omega_n^2} \tag{3.4}$$

where $\omega_n = 30, \xi = 0.5$. The variable τ_d (set to 30ms in the simulation) represents a delay in the magnetic sensor outputs which models possible HW/SW measurement signal processing time.

Some closed loop simulation results are shown in Figg. 3.2, 3.3.

The initial condition for the estimated orientation was set to $R^*(0) = I$, i.e. $\phi_0^* = \theta_0^* = \psi_0^* = 0$, whereas the actual orientation of the AUV was initially set to $[\phi_0\ \theta_0\ \psi_0] = [\pi/3\ \pi/4\ \pi/2]$; this significant divergence allows to evaluate the transient of the observer (see Fig. 3.4) for different values of the filter gains denoted as k_i in Eqn. (3.1), namely k_g for the gravitometer and k_b for the magnetic sensor[4].

Note that by increasing the two gains the estimation settles more rapidly to the actual value, but the overall signal is more noisy; this fact requires to choose the proper trade-off according to the quality of the measured data.

[2]Gravity vector in the right-handed space reference frame is equal to $g_0 = [0\ 0\ 9.8]^T$.

[3]Magnetic field vector is normalized without loss of generality to $b_0 = [1\ 0\ 0]^T$.

[4]The gain k_b is taken about 10 times greater than k_g to take into account the gain difference between $\mathbf{b}_0$ and $\mathbf{g}_0$.

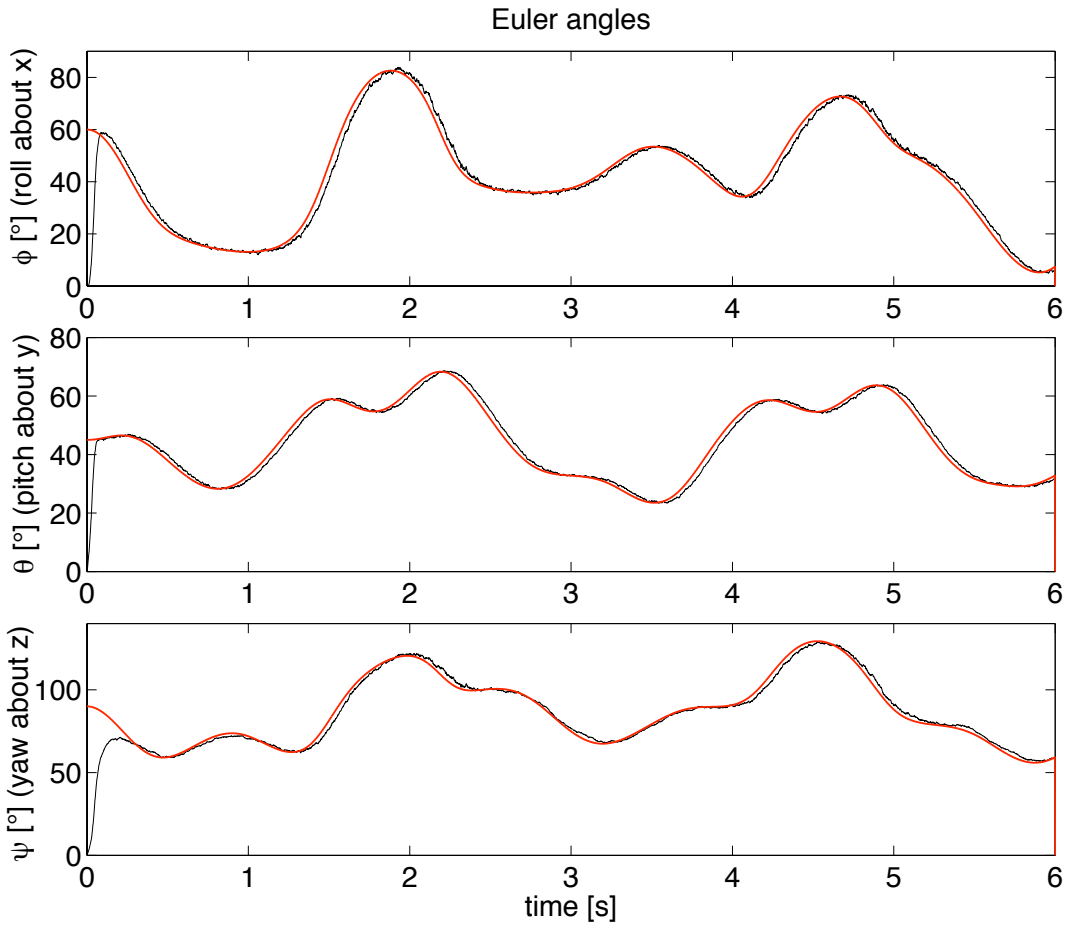

FIGURE 3.2: Actual Euler angles (*red* lines), compared with their estimation (*black* lines) in a 6s simulation. Filter gains were set to $k_g = 1$ for gravity and $k_b = 10$ for the magnetic filed.

3.1.3 Experimental results

In this section some experimental results relative to attitude estimation via complimentary filter are presented, to validate the effectiveness of the algorithm.

The boxfish model described in Appendix B, equipped with two dual-axes gyroscopes and a 3-axes accelerometer, was employed to collect the data for the attitude estimation. The model was mounted on a holder and set free to rotate about the roll (x) and pitch (y) axis (see Fig. 3.5). The holder included two MAE-3 US-Digital angular sensors to measure exact angular displacement. The accelerometers were used to measure the static gravity acceleration, while the gyroscopes provided the angular rate with respect to the three axes in the body reference frame.

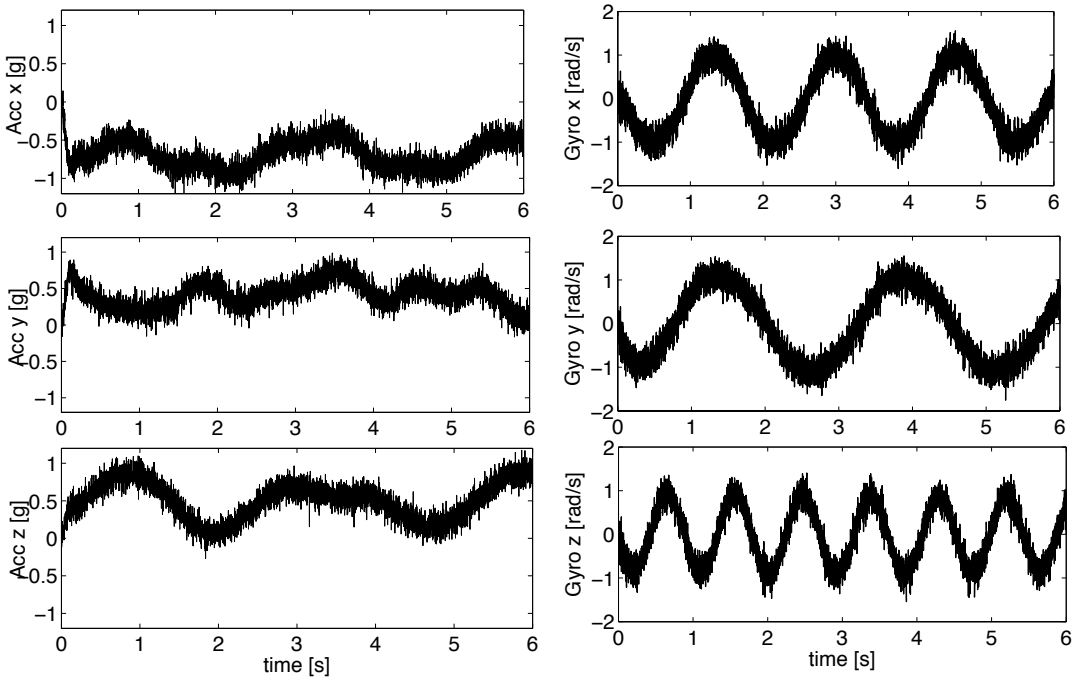

FIGURE 3.3: Data measured from the simulated accelerometers (on the *left*) and gyroscopes (on the *right*).

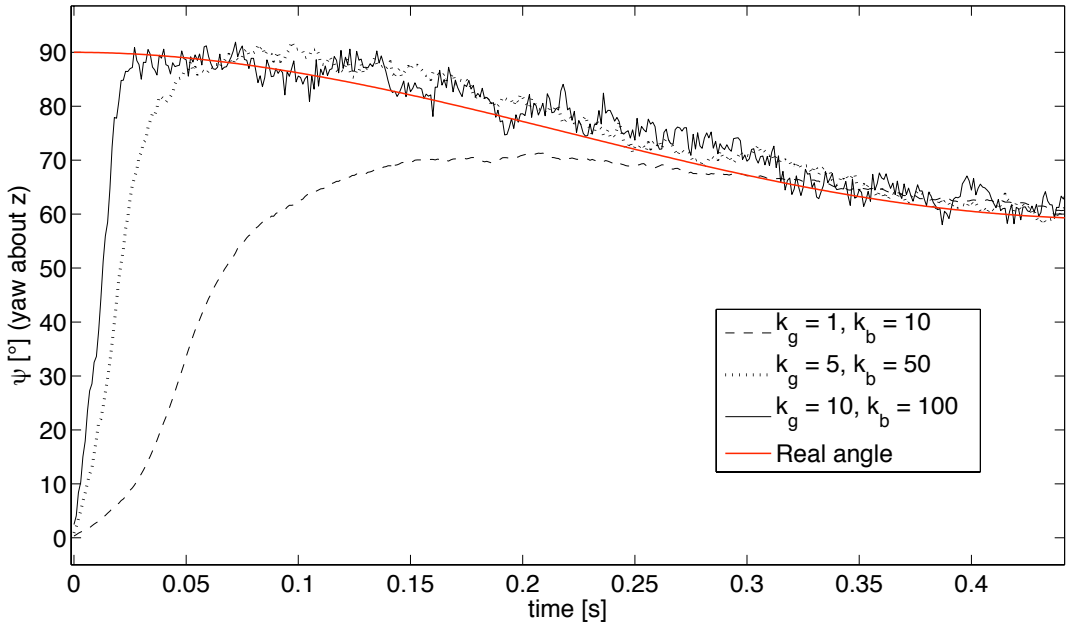

FIGURE 3.4: Transient of the filter for different values of the gains k_g and k_b.

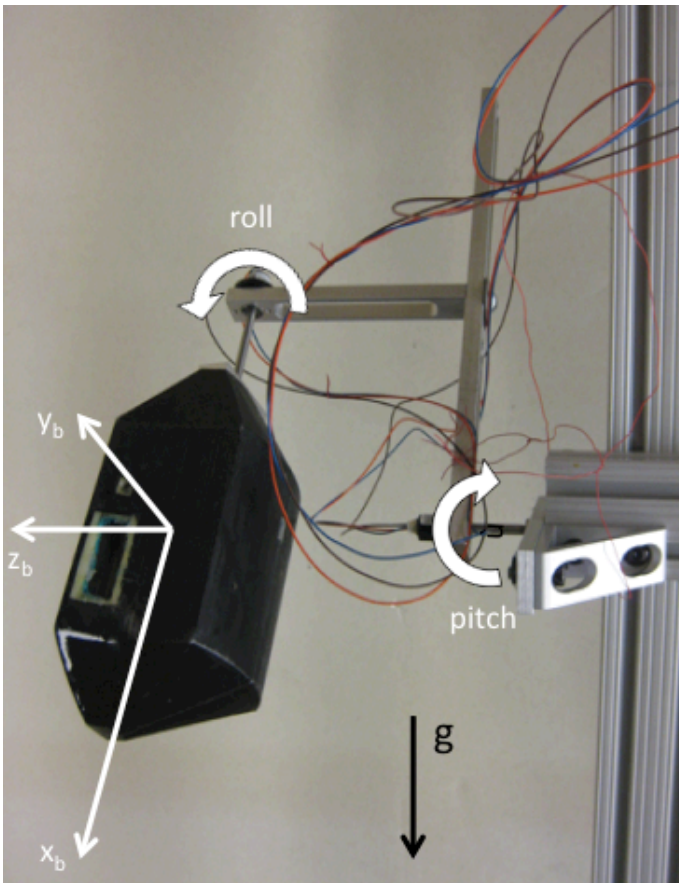

FIGURE 3.5: The support used to perform the combined roll/pitch motion. The body-fixed coordinate system is also shown.

The results of attitude estimation from the complementary filter are shown in Fig. 3.6 and the associated sensor readouts are shown in Fig. 3.7 and 3.8. The plots show rapid convergence of the estimated angles to the true angles in the first half second of the experiments when the body frame is kept fixed, and then they remain very close to the true angles also during the body motion.

The effectiveness of sensor fusion is best appreciated by removing either the gyros or the accelerometers from the filter. In the first case, the removal of the gyros results in an evident low pass behavior of the estimated angles which exhibit a time lag as compared to the true angle. Differently, if only gyros are used, the estimated angles have rapid response to body motion, but they incurs in a drift that overtime leads to large offsets as compared to the true angles. The complementary filter, as explained above, fuse the benefits from both sensor modality giving rise to a filter with a very high bandwidth.

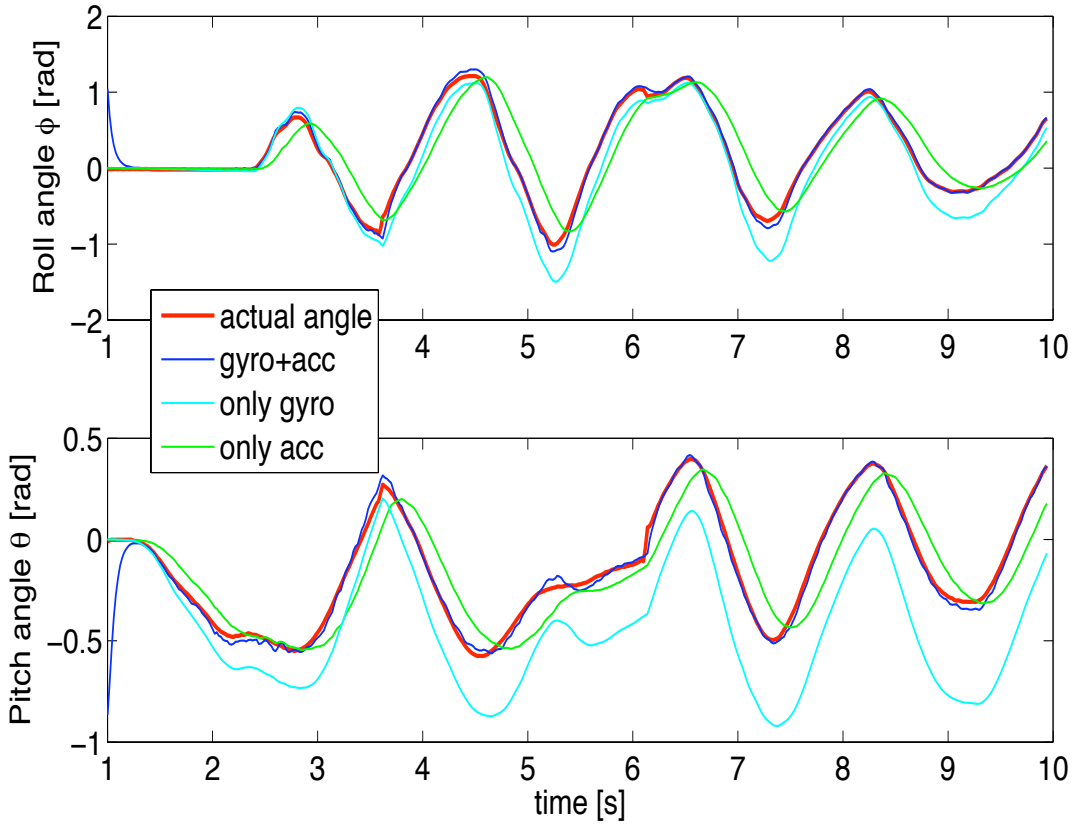

FIGURE 3.6: Comparison between the actual roll angle (*top*) and pitch angle (*bottom*) and three different estimations evaluated using the only accelerometers data, the only gyroscopes data or both.

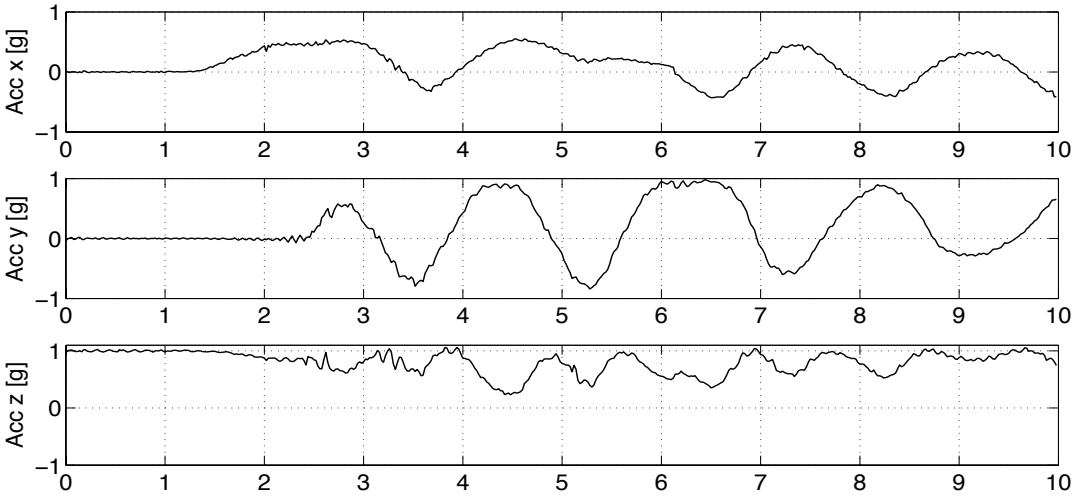

FIGURE 3.7: Accelerometers readouts. Readings are normalized with respect to gravity acceleration g.

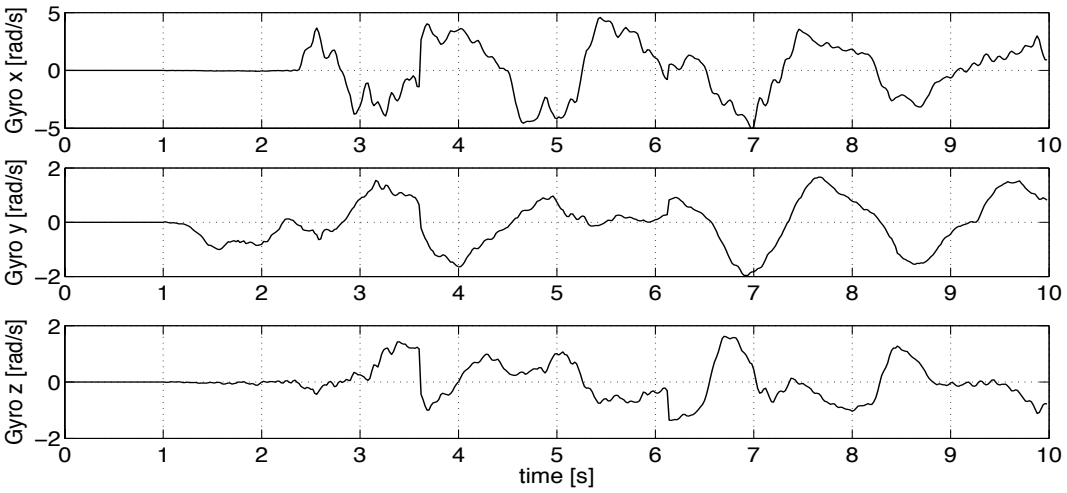

FIGURE 3.8: Gyroscopes readouts.

3.2 Attitude control

The good performance and the high degree of reliability and noise rejection of the complementary filter discussed above can be effectively exploited for control purpose: in the present section the control algorithm proposed by Campolo *et al.* in [45] is considered and validated through a realistic simulation of the AUV dynamics in Matlab environment. Some geometrical concepts shall be used in this section; for the reader who is not familiar with the geometric approach to control, we refer to excellent textbooks [49, 77, 78].

3.2.1 Control algorithm

The control law implemented for the attitude stabilization is obtained by combining the complementary filter discussed in the previous section with a particular implementation in $SO(3)$ of the *intrisic*[5] controller discussed in [79, 80] for a generic class of mechanical systems on Lie groups. In particular, assuming the system to be fully actuated, the control torque for the feedback stabilization takes the form:

$$\boldsymbol{\tau}_{FB}(R, \boldsymbol{\omega}) = -\mathcal{I}\left(R^T \mathtt{grad}U + k_{\boldsymbol{\omega}}\widehat{\boldsymbol{\omega}}\right)^{\vee} \tag{3.5}$$

[5]That is, it does not depend on the contingent choice of configuration coordinates (in our case, $SO(3)$).

where $U : SO(3) \longrightarrow \mathbb{R}$ is the error function and k_ω is the gain for the Rayleigh dissipative term. The *vee* operator $(\cdot)^\vee : \mathfrak{so}(3) \longrightarrow \mathbb{R}^3$ denotes the inverse of the *hat* operator introduced in Section §2.3.4, defined, for a generic vector $\mathbf{v} = [v_1 \ v_2 \ v_3]^T$ such that $\hat{\mathbf{v}} \in \mathfrak{so}(3)$, as follows:

$$(\cdot)^\vee, \hat{\mathbf{v}} : \mathfrak{so}(3) \longrightarrow \mathbb{R}^3 : \begin{bmatrix} 0 & -v_3 & v_2 \\ v_3 & 0 & -v_1 \\ -v_2 & v_1 & 0 \end{bmatrix} \longrightarrow \begin{bmatrix} v_1 \\ v_2 \\ v_3 \end{bmatrix} \triangleq (\hat{\mathbf{v}})^\vee \tag{3.6}$$

As for $U(R)$, different choices of the error function have been proposed in literature (see, e.g. [81]); in the present work the error function proposed by Koditschek (named *navigation function* in his original work [82]) is adopted, thus $U(R)$ is defined as:

$$U(R) \triangleq \frac{1}{2}\mathtt{tr}\{K(I - \bar{R}^T R)\} \tag{3.7}$$

with $K \in \mathbb{R}^{3\times3}$ positive definite symmetric matrix. By calculating its gradient as suggested in [81] one gets the feedback control law

$$\boldsymbol{\tau}_{FB}(R, \boldsymbol{\omega}) = \mathcal{I}\left(\frac{1}{2}\mathcal{I}^{-1}(K\bar{R}^T R - R^T \bar{R} K^T) + k_\omega \hat{\boldsymbol{\omega}}\right)^\vee \tag{3.8}$$

By coupling this feedback control law and the dynamic observer discussed above through the separation principle, it is possible to write the full dynamic equations as follows [45]:

$$\begin{cases} \dot{R} = R\,\widehat{\boldsymbol{\omega}} \\ \dot{\boldsymbol{\omega}} = J^{-1}(\boldsymbol{\tau}_{FB}(R^*, \boldsymbol{\omega}^*) - \boldsymbol{\omega} \times J\boldsymbol{\omega}) \end{cases} \quad attitude \ \ controller$$
$$\begin{cases} \dot{R}^* = R^*\,\widehat{\boldsymbol{\omega}}^* \\ \boldsymbol{\omega}^* = \boldsymbol{\omega}_{gyr} + k_b(\mathbf{b} \times \mathbf{b}^*) + k_g(\mathbf{g} \times \mathbf{g}^*) \end{cases} \quad dynamic \ \ observer \tag{3.9}$$

In fact a discrete-time version of this algorithm is used, operating a discretization via the Rodrigues' formula of Eqn. 3.2 to guarantee $R(t)$ and $R^*(t)$ not to drif from $SO(3)$. In what follows the attitude control algorithm is validated through simulations.

3.2.2 Simulation results

Similarly to §2.3.5, Matlab simulation environment was used to compute the dynamics and hydrodynamics equations which describe the AUV model; the control algorithm

described above was then introduced in a control loop as illustrated in the block diagram of Fig. 3.9. As regards data from sensors, on board accelerometers and

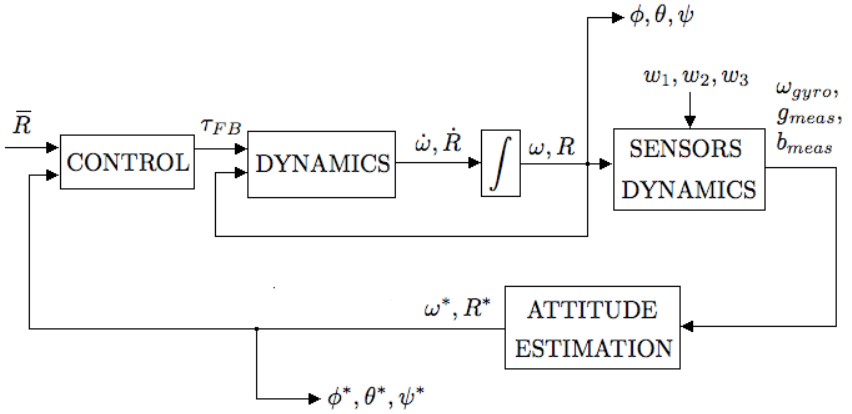

FIGURE 3.9: Schematic design of the control algorithm implementation.

gyroscopes were simulated according to Eqn. 3.3, and the same parameters used in §2.3.5 were adopted.

During the simulation the AUV body, starting from an orientation $R(0) \neq I$, namely $\phi_0 = \pi/4$, $\theta_0 = \pi/4$, $\psi_0 = \pi/6$, is driven by the control torque to the desired position $\overline{R}(t) = I$; no information about the initial orientation of the vehicle is provided to the observer (whose initial condition is conventionally set to $R^*(0) = I$), thus the estimation initially differs from the actual position, and a transient in the attitude estimation is observed (see Fig. 3.11). Also, a 0.2N force is constantly applied along x direction to produce forward motion, and a 5N disturbance lasting 0.2s is introduced along the same direction at time $t_1 = 2$s[6]; as a result, the estimated orientation is miscalculated, i.e. the acceleration is interpreted as a pitch-down rotation, therefore the controller produces a wrong pitch-up control input which creates a temporary displacement from the equilibrium position. Nonetheless, as soon as the disturbance disappears, the observer promptly settles on the correct value, and the disturbance is effectively compensated for by the control algorithm. Simulation results are shown in Figg. 3.10, 3.11, 3.12.

[6]This kind of disturbance is frequently encountered in practice as the effect of a sudden acceleration, which typically occurs, for example, when switching from hovering to cruising mode, or when performing a firm deceleration; for this reason the robustness of the algorithm is such a crucial issue.

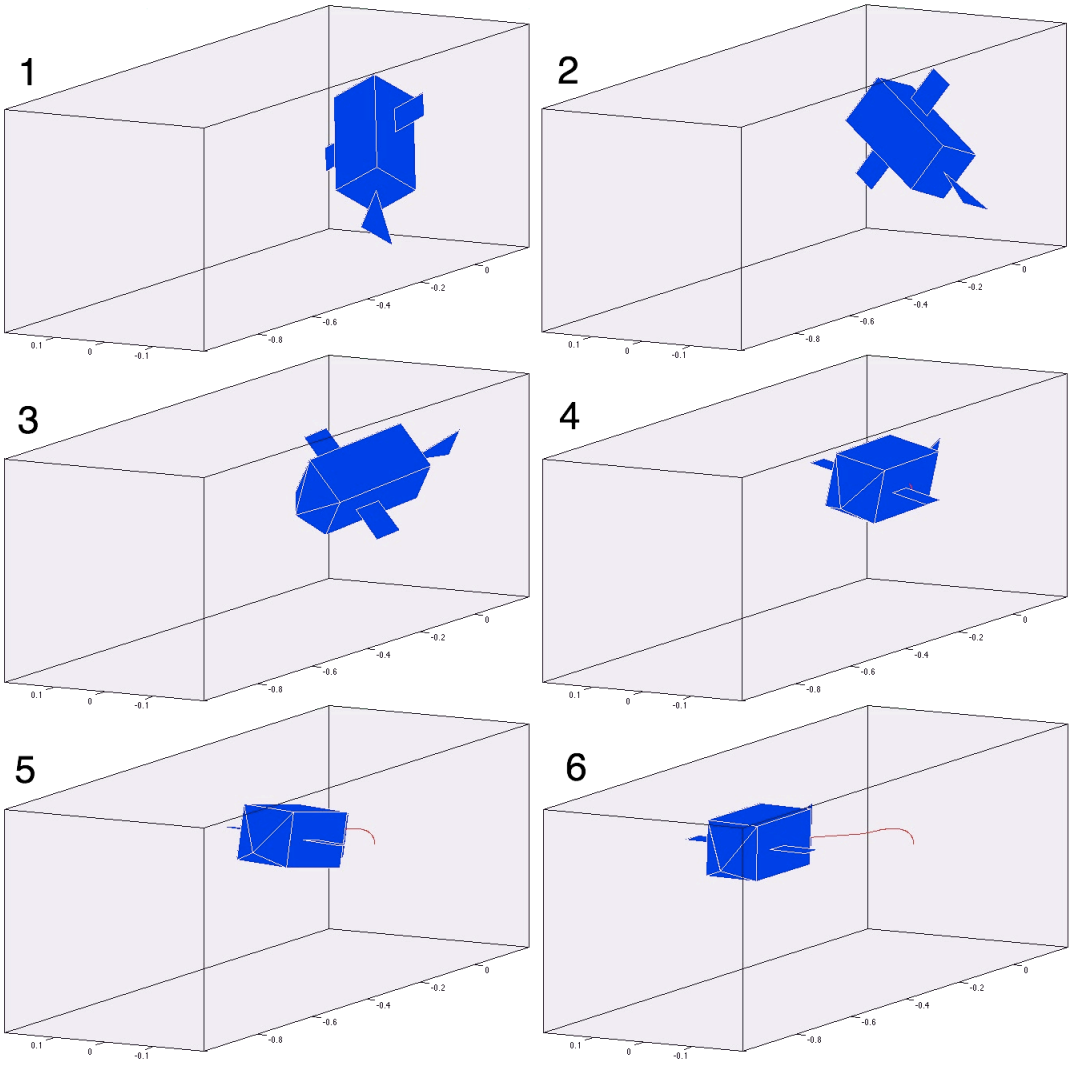

FIGURE 3.10: A sequence of pictures showing the trajectory of the boxfish during the attitude control simulation; the pitch-up movement as effect of the disturbance is shown in frame 5.

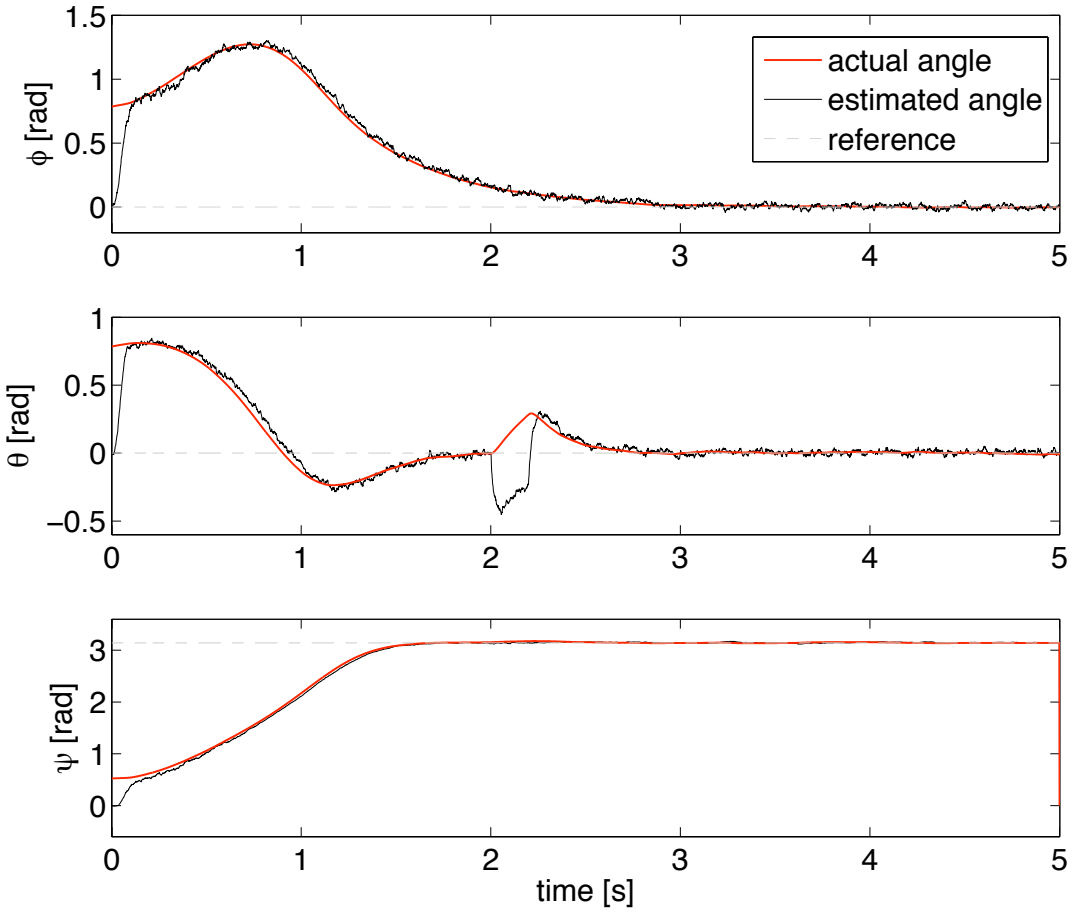

FIGURE 3.11: Euler angles (actual in *red*, estimated in *black*) for the attitude control simulation. A 5N disturbance was applied between $t_1 = 2$s and $t_2 = 2.2$s.

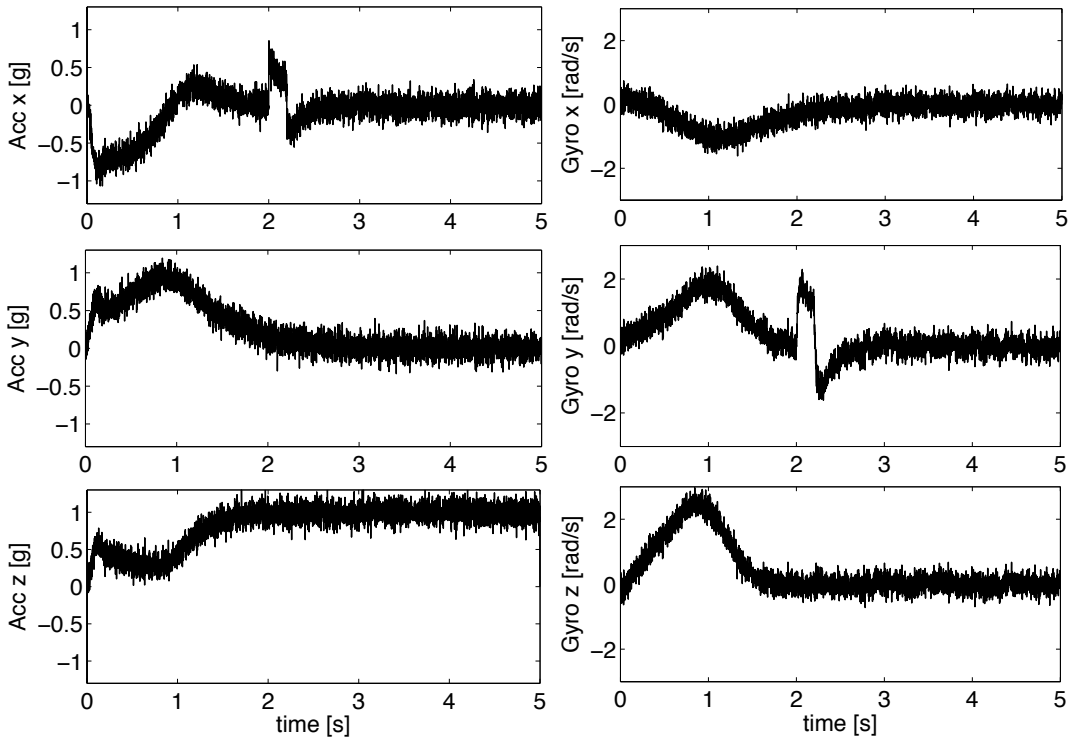

FIGURE 3.12: Data measured by the simulated sensors (accelerometers readouts on the *left* gyroscpe readouts on the *right*).

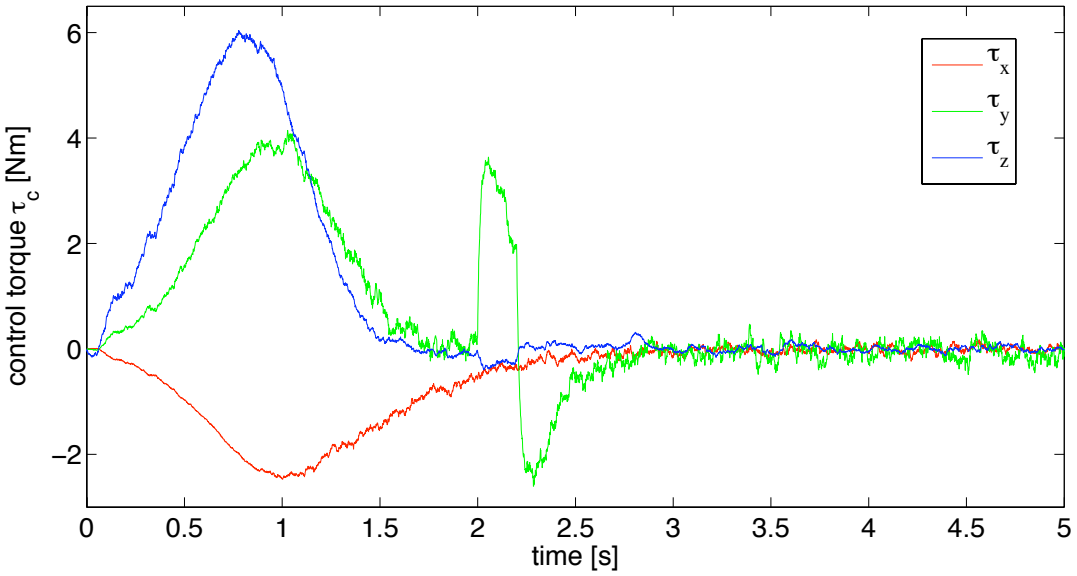

FIGURE 3.13: Control torque applied to the simulated model.

Chapter 4

Roll stability

The conceptual intent which underlies the design of most underwater and aerial vehicles typically moves toward a stable roll dynamics, i.e. restoring forces are traditionally exploited to make the roll angle $\phi = 0$ a stable equilibrium; this is done basically by choosing an appropriate body shape and a convenient reciprocal position for center of mass and center of buoyancy. Besides these intrinsic forces, the dynamics of the AUV is affected by the control torque τ_x, whose qualities depend on the kind of actuator adopted. The following sections focus on the effectiveness of a pectoral fin based control for the roll stabilization, and a simple control algorithm is proposed and validated through a set of experimental results.

4.1 Roll stability for the boxfish

The particular shape of the boxfish allows a stable, smooth motion even at cruising speeds, due to the stabilizing effect of the self-correcting vortices shed from its keels. Bartol *et al.* focused on the effect of these vortices [16–18] primarily in regard to pitch stabilization; however, the presence of self-correcting vortices shed by dorsal and ventral keels was observed by studying via the model detailed in Appendix B through PIV analysis: a sequence of three images showing velocity field and vorticity is presented in Fig. 4.1.

The experimental tests were performed on the model developed by Kodati *et al.* in [40, 83]: the model was set to be neutrally buoyant, therefore no restoring forces were acting on the model, and a constant flow was simulated by dragging the model along the tank with a linear stage, as shown in Fig. 4.2; the laser sheet was

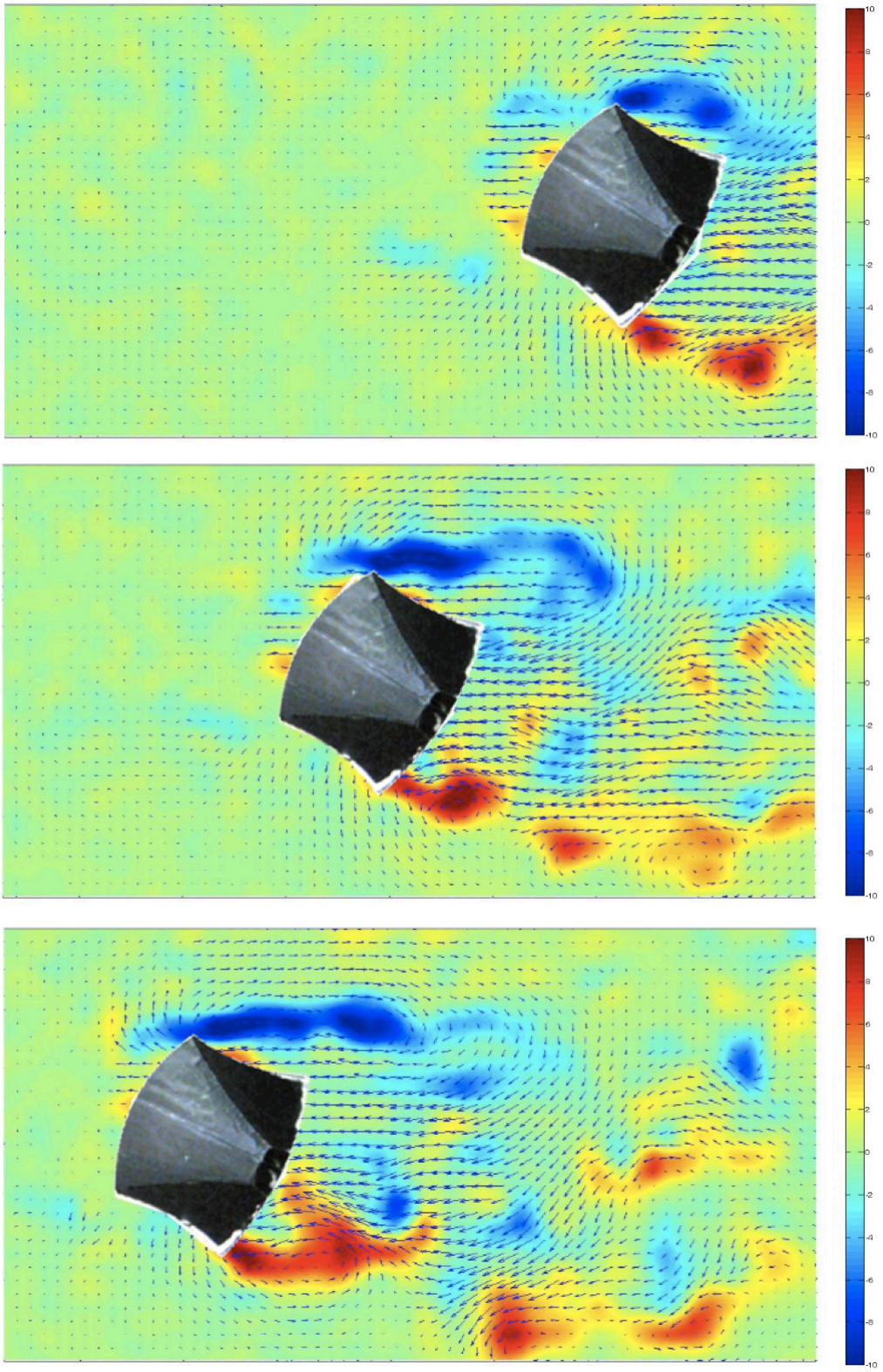

FIGURE 4.1: Front view of the model in a sequence of three images showing PIV analysis for roll vorticity (negative vorticity is clockwise, positive counterclockwise).

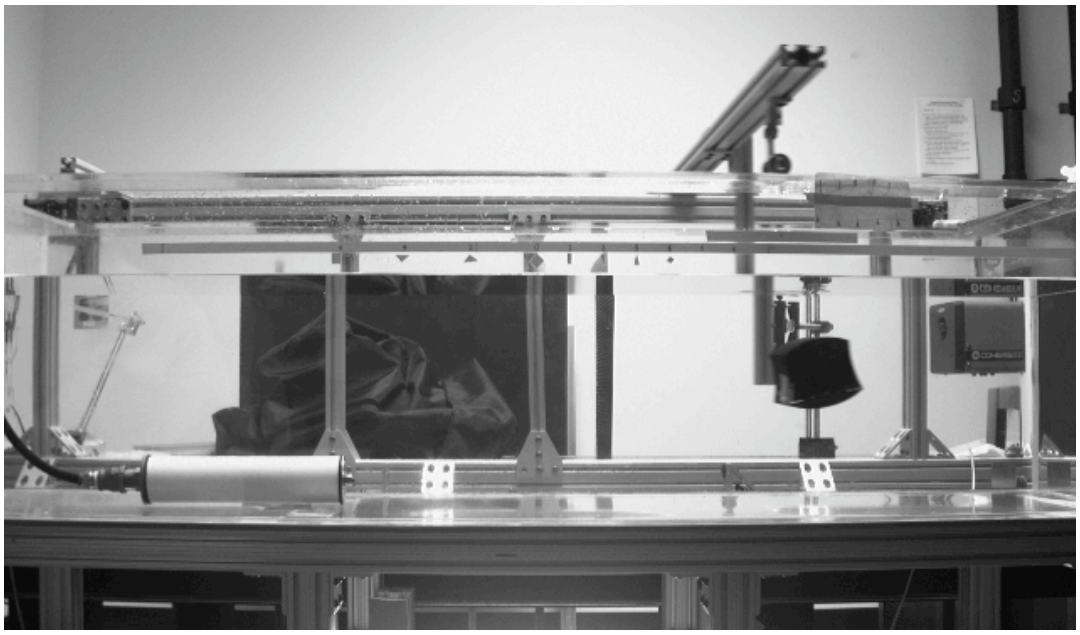

FIGURE 4.2: Experimental setup: the model is dragged along the tank with a linear stage, being free to rotate about the roll axis.

pointed at the model parallel to its cross-sectional plane (for a detailed analysis of PIV technique the reader is referred to [84]).

4.2 Roll dynamics

For a clear analysis of the issue, a simple dynamic model, derived from Eqn. (2.52), is now proposed: consider the one-degree-of-freedom motion about the x axis, where the velocities along any other direction are set to zero, and the pitch angle is taken to be $\theta = 0$. Then one gets the following dynamics:

$$(I_{xx} + m_{44})\dot{p} = k_p p + k_{|p|p}|p|p - \rho V g z_b \sin\phi + \tau_x \tag{4.1}$$

where τ_x indicates the control torque applied through pectoral fins. For small perturbations about $\phi = 0$ (which is a typical operating point for many AUVs) it is possible to consider the linearized system:

$$\begin{bmatrix} \dot{p} \\ \dot{\phi} \end{bmatrix} = \begin{bmatrix} \frac{k_p}{I_{xx}+m_{44}} & \frac{-\rho V g z_b}{I_{xx}+m_{44}} \\ 1 & 0 \end{bmatrix} \begin{bmatrix} p \\ \phi \end{bmatrix} + \begin{bmatrix} \frac{1}{I_{xx}+m_{44}} \\ 0 \end{bmatrix} \tau_x \tag{4.2}$$

Since the linear drag coefficient k_p is negative, by applying Routh stability criterion it is clear that the stability of system 4.2 only depends on the relative position of the center of buoyancy with respect to the center of mass: for $z_b > 0$ the equilibrium point $\phi = 0$ is asymptotically stable whereas $\phi = \pi/2$ is unstable; conversely, for $z_b > 0$ (i.e. if the center of buoyancy lies below the center of gravity), the equilibrium property is inverted. Thus, due to the torque produced by gravity, an oscillatory motion about the equilibrium is observed.

Obviously this simple system does not provide an exhaustive description of the AUV dynamics, nor is this its purpose; nevertheless, it can be usefully taken as a model to come up with an effective control law for its attitude stabilization.

4.3 Stabilization via pectoral fin control

Pectoral fins plays an important role in fish locomotion, especially during hovering and low speed maneuvering. In fact they are often employed as thrusters as well (see e.g. the slowest gait of the boxfish [20]). In the present chapter the use of pectoral fins both to produce forward thrust and to control the AUV attitude is analyzed.

4.3.1 Thrust production

One of the main shortcomings of tail fin propulsion is the recoil movement which inevitably affects the attitude of the vehicle, especially in the yaw plane. Differently, a

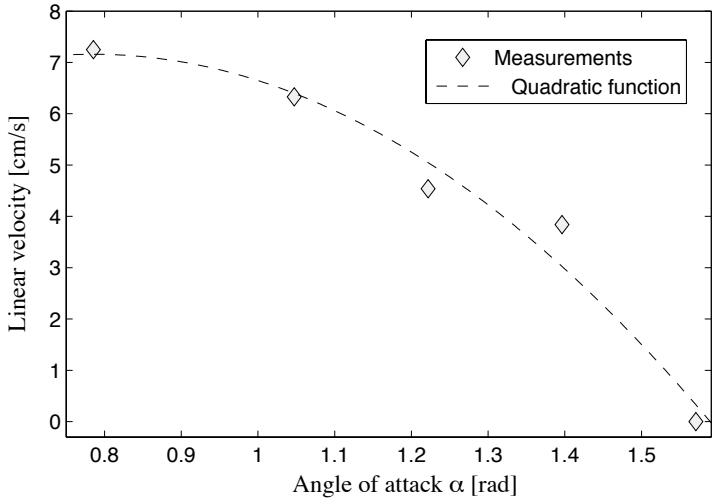

FIGURE 4.3: AUV linear velocity vs pectoral fins angle of attack. The measures were taken along a 75 cm long path, with fins beating at 3Hz.

pectoral fin based propulsion would not suffer this kind of problem, since the symmetric force generation compensates for and balances the yaw plane recoil movements. The thrust produced depends on the angle of attack of the fins: different tries were made for angles of attack varying between 0 and $\pi/2$, with pectoral fins beating at 3Hz with amplitude $A = \pi/4$, and the results are shown in Fig. 4.3. By increasing the angle of attack the thrust efficiency is reduced, whereas maneuverability and roll controllability increase significantly. This fact is confirmed by the experimental results shown in Fig. 4.4: the roll angle convergency to the reference is faster as the angle of attack increases.

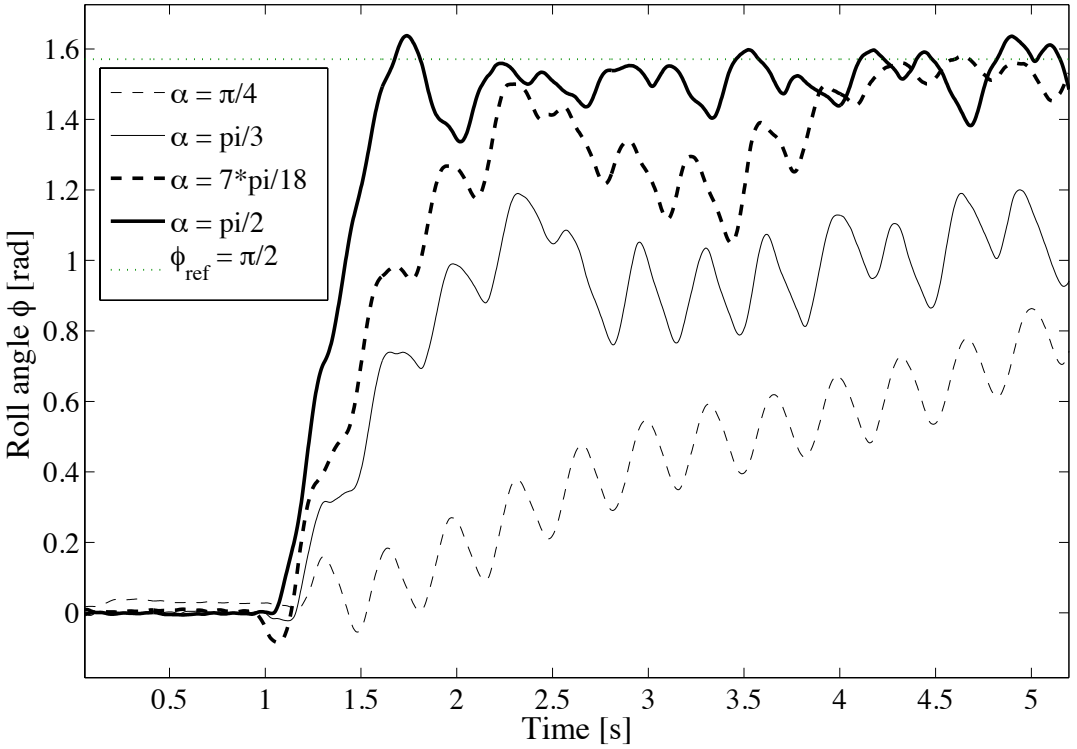

FIGURE 4.4: Estimated roll angles different roll control experiments: four different angles of attack α were chosen for pectoral fins, and the reference roll angle was set to $\phi_{ref} = \pi/2$. Between $t_0 = 0$s and $t_1 = 1$s an automatic calibration was performed on the AUV sensors.

4.3.2 Control law

In the present section a motion pattern for the two pectoral fins to control the roll stability is derived. Consider the paired fins discussed in Section 2.3.3.2; for the

purpose of control it is reasonable to base the fin oscillations on a periodic pattern. In particular, the lead-lag motion can be parameterized as follows:

$$\begin{cases} \beta_\ell(t) &= \beta_{\ell 0} + A_\ell \sin(\omega t + \phi_\ell) \\ \beta_r(t) &= \beta_{r0} + A_r \sin(\omega t + \phi r) \end{cases} \tag{4.3}$$

where β_ℓ and β_r denote, respectively, the left and right fin stroke angle.

Some commonly adopted control variables for the attitude stabilization are the mean angles $\beta_{\ell 0}$, β_{r0}, the finbeat amplitudes A_ℓ, A_r or the finbeat frequency $f = \omega/2\pi$; in the present work a different approach is pursued, which focuses on the ratio between the amplitude of the two fins to control the roll angle. To this end, Eqn. 4.3 is rewritten introducing the control variable $u(t)$:

$$\begin{cases} \beta_\ell(t) &= A(0.5 - u(t)) \sin(\omega t) \\ \beta_r(t) &= A(0.5 + u(t)) \sin(\omega t) \end{cases} \qquad u(t) \in [-0.5,\ 0.5] \tag{4.4}$$

For the sake of simplicity, it is assumed that the fish is hovering (i.e. body linear velocities are sufficiently small) and that the angle of attack of the fins remains constant. Under these assumptions, hydrodynamic forces acting on pectoral fins can be directly evaluated from the kinematic equations, and therefore it is possible to simulate the dynamics of the linear model described by Eqn. 4.2.

4.3.3 Simulation

The linear model was implemented in Matlab using the following control law:

$$u(t) = -k(\phi_{ref} - \phi(t)) \tag{4.5}$$

where ϕ_{ref} is the reference roll angle. For the simulation the finbeat frequency f was set to 2Hz, and the amplitude A to $\pi/4$. Two simulations were performed (see Fig. 4.5): in the first one the center of buoyancy was taken coincident with the center of mass − thus gravity had no influence on p dynamics −, while in the second one z_b was set to 0.04m (the case $z_b = -0.04$m was analogous by symmetry, therefore was omitted for clarity). The greater is z_b, the stronger is the control torque needed to keep a desired position different from the equilibrium (both for positive and negative z_b values).

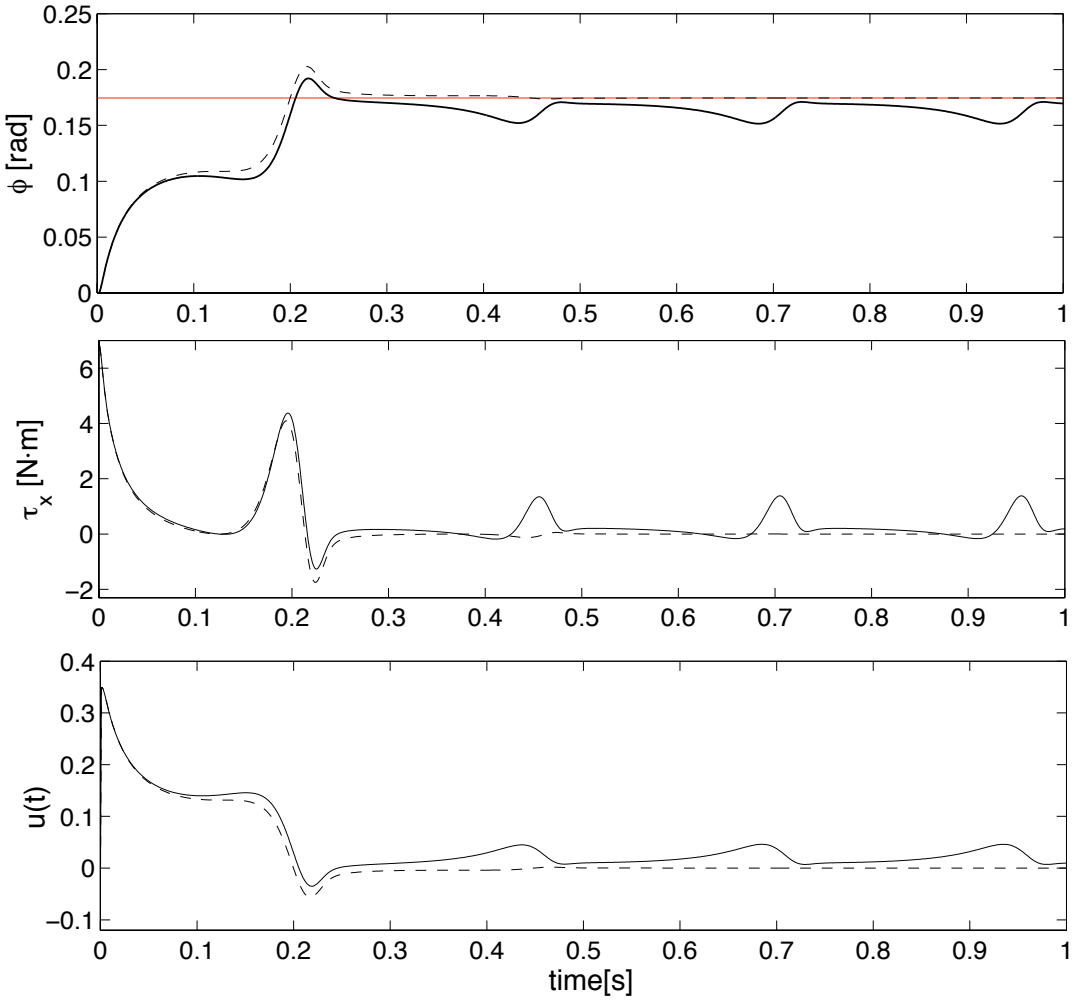

FIGURE 4.5: Simulation results for the roll control of model 4.2; from *top* to *bottom*: roll angle $\phi(t)$, control torque $\tau_x(t)$ and control input $u(t)$ for the neutrally buoyant case (dashed line) and for the bottom-heavy case (solid line).

4.3.4 Experimental results

In the following sections the results of two different sets of experiments are discussed, to validate the efficiency of the proposed control algorithm.

4.3.4.1 Experimental setup

The experiments were performed in a tank filled with mineral oil ($\rho = 1001$ kg/m^3); a one degree-of-freedom holder was built to constrain the model to rotate about the x axis only. Also, in order to validate the dynamic observer discussed in the previous chapter, the model was equipped with the sensor suite detailed in Appendix B, and

the control law was evaluated on the basis of the estimated state:

$$u(t) = -k(\phi_{ref} - \hat{\phi}(t)) \tag{4.6}$$

where $\hat{\phi}$ represents the roll angle computed through the sensor fusion algorithm. An automated routine for the sensors calibration was run before the beginning of each experiment, in order to guarantee a precise estimation of the state variable; a comparison with the real values of ϕ was provided by US-Digital MAE-3 angular position sensor, which has been placed at the joint of the holder rod. For both the experiments the control gain k in Eqn. 4.6 was set to 2, while fins were flapping at frequency $f = 2$Hz, with amplitude $A = \pi/3$ at constant angle of attack $\alpha = 2\pi/5$. Lastly, the model was made slightly bottom-heavy by adding some weight on the bottom part of the hull.

4.3.4.2 Results

As for the first set of experiments, different roll angles were chosen as reference: roll

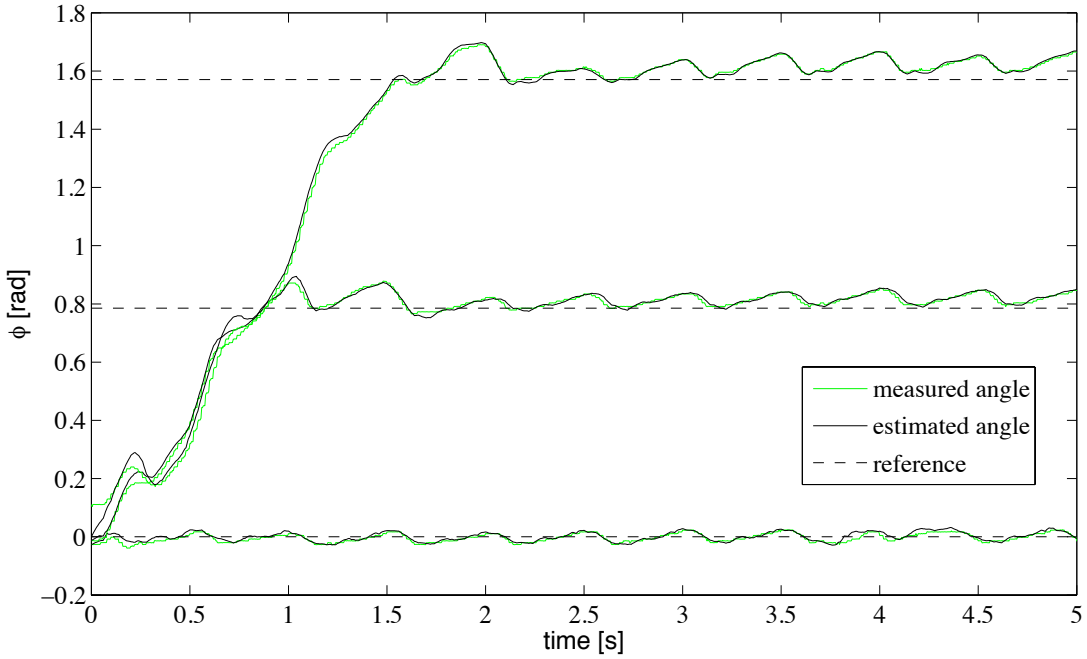

FIGURE 4.6: Data collected during three roll stabilization experiments, respectively at $\phi_{ref} = 0$, $\phi_{ref} = \pi/4$ and $\phi_{ref} = \pi/2$ (*dashed lines*). The estimation (*black lines*) calculated in real time via the sensor fusion algorithm is compared to the actual angle (*green lines*), measured on the holder with MAE-3 angular sensor.

stabilization was performed about $\phi_{ref} = 0$, $\phi_{ref} = \pi/4$ and $\phi_{ref} = \pi/2$ (see in Fig. 4.6). Note that the convergency speed (estimated around 1.1 rad/s) does not depend on the reference angle, since during the transient the control variable $u(t)$ reaches its maximum at ± 0.5, that is, one fin is flapping with maximum amplitude A, the other is at rest.

The aim of the second experiment is that of testing the control algorithm in presence of disturbances: the model was dragged along the tank with constant speed $v = 0.3$m/s, and the streamflow produced a disturbance torque which displaced the body from its equilibrium position. In Fig. 4.7 (*top*) the behavior of the system both with pectoral fin control and without it (i.e. with zero finbeat amplitude) is shown.

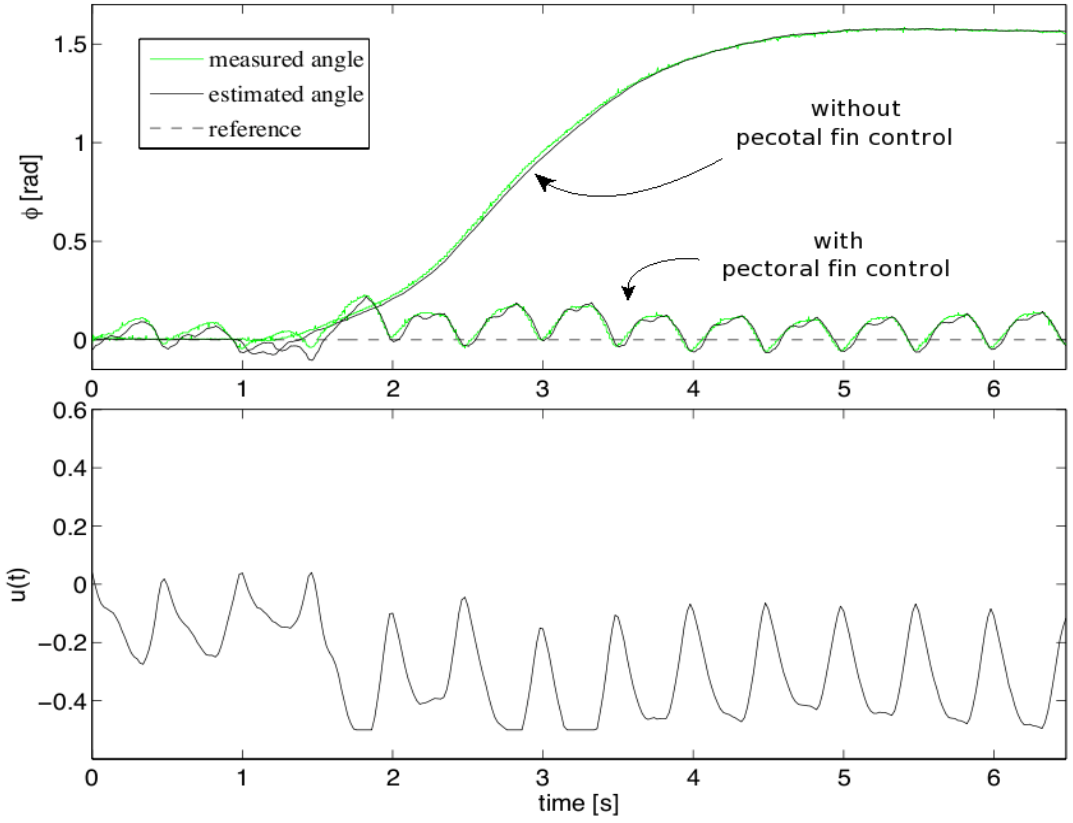

FIGURE 4.7: *Top*: measured (*green lines*) and estimated (*black lines*) roll angles of the model dragged along the tank at 0.3m/s for two different tries, respectively with and without pectoral fin control. *Bottom*: the corresponding control variable $u(t)$.

The good performance of the overall system, whose control input only depends on the estimated data, is due to the accurate agreement between real and estimated angle; furthermore, the proportional control law 4.6 seems to be effective for the

considered system, therefore it is likely that roll dynamics can be properly described by a linear model such the one reported in Eqn. 4.2.

4.3.5 Control with 6 degrees of freedom

The results presented above, even if promising and encouraging, are limited to the single degree of freedom movement, and consequently their validity needs to be proved in the case of a freely moving AUV as well. Therefore it is important to state whether the proposed pectoral fin control introduces any recoil movement by influencing the overall attitude or not.

In fact an evident correlation between roll and yaw angles was experimentally observed. This is primarily to be attributed to the lift force generated by pectoral fins when the AUV is tilted in the roll axis and the gravity force does not completely compensate for it. In Fig. 4.8 the estimated Euler angles of the freely moving AUV

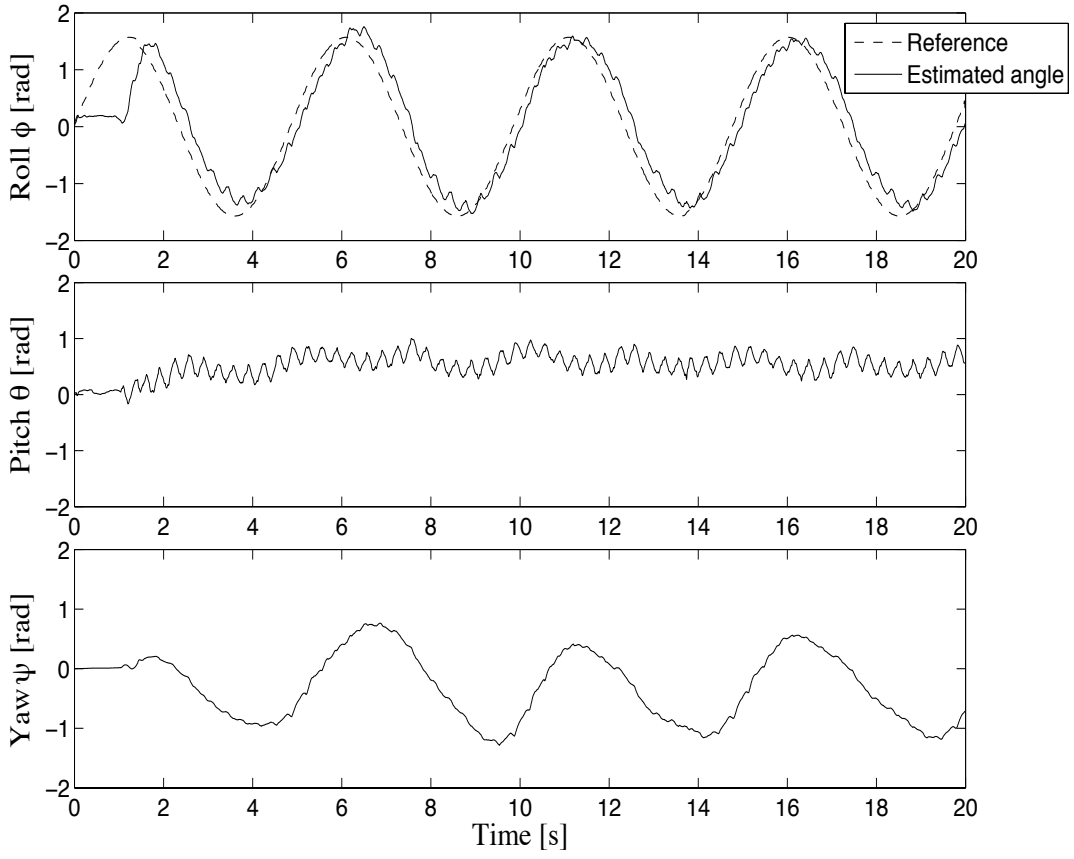

FIGURE 4.8: Euler angles estimated with the sensor fusion algorithm in the 6 dof roll control experiment, with a sinusoidal signal as a reference. Between $t_1 = 0s$ and $t_2 = 1s$ sensors calibration is performed.

during a 20 seconds experiment are shown: the linear controller presented in the previous paragraph was used to track the following roll angle

$$\phi_{ref}(t) = \frac{\pi}{2} \sin 2\pi f t \tag{4.7}$$

whose frequency f was set to 0.2Hz. The relation between rolling oscillations and yaw orientation suggests the the possibility to control the AUV in the steering plane through the roll angle; this means that the control of a neutrally buoyant AUV in the steering plane would be possible with the only use of pectoral fins. This possibility is discussed and validated in the following section.

4.4 Combined roll-yaw control

The evidence of a precise relation between roll angle and yaw rate was experimentally observed and reported in Fig. 4.9: the AUV was mounted on an apposite holder with

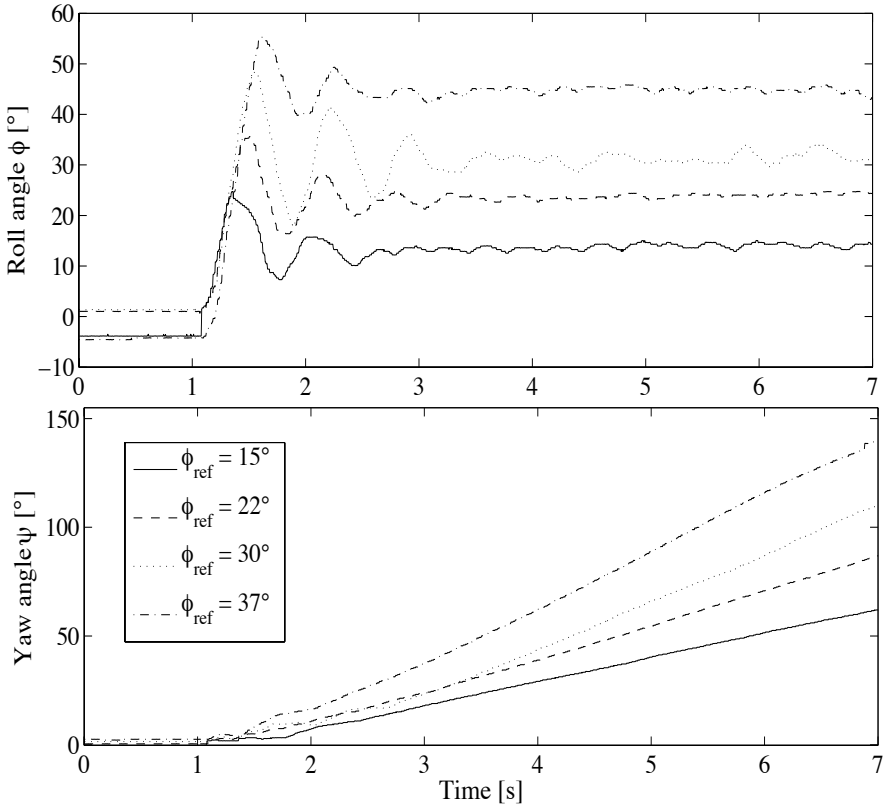

FIGURE 4.9: Roll (*top*) and yaw (*bottom*) angles measured by the respective angular position sensors in four different roll control experiments: the yaw angle varies in a linear fashion, with slope proportional to the relative roll angle.

two degrees of freedom, equipped with two angular position sensors. By controlling the roll angle with pectoral fins it can be noticed that the yaw angle increases linearly, with a constant rate proportional to the relative roll angle. Assuming that this linear relation holds, it is therefore possible to control the AUV orientation in the yaw plane through its roll angle, as demonstrated by the results shown in Fig. 4.10. Four

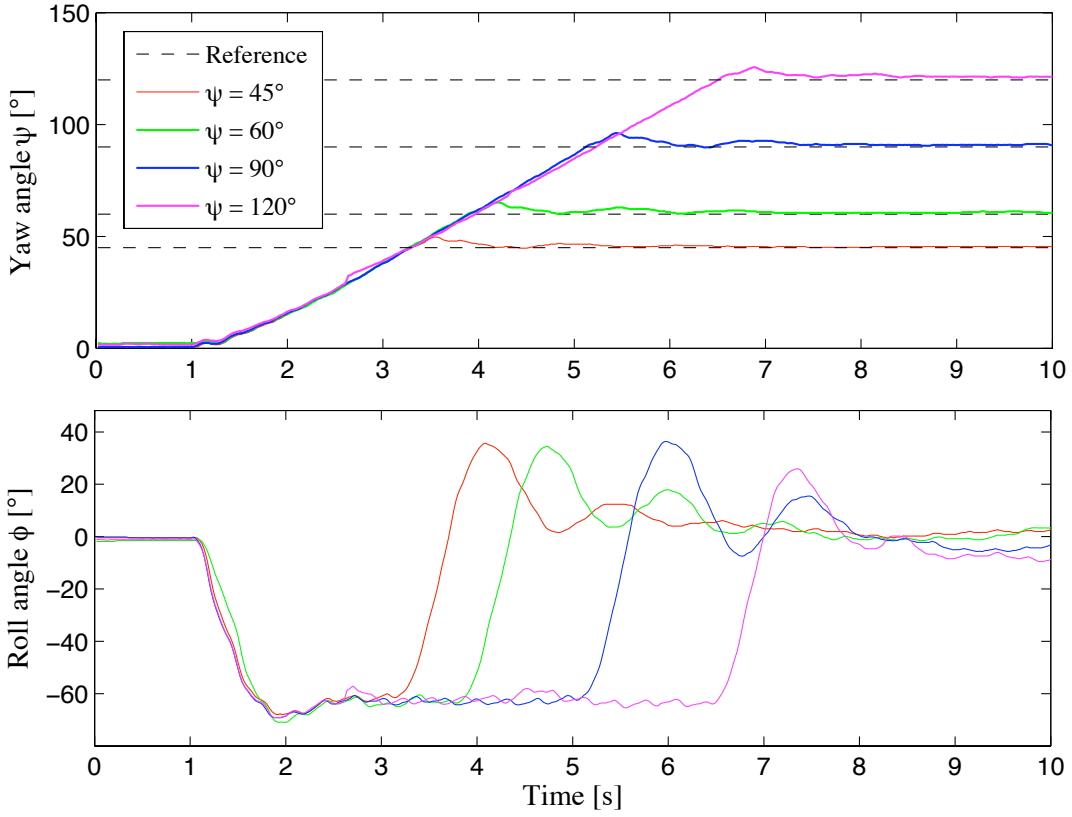

FIGURE 4.10: Yaw (*top*) and roll (*bottom*) angles in 4 tries with different reference angles ψ. The rolling movement is used to control the AUV orientation in the steering plane.

different setpoints were chosen as reference for the yaw angle, and the roll control angle was saturated at $\phi_{sat} = \pi/3$, this producing a constant yaw rate before settling to the setpoint.

Chapter 5

Conclusion

In this work a complete mathematical model for the boxfish AUV was derived, and experimental results of its attitude estimation and control through oscillating fins were presented. As a main result, a simple pectoral fin controller was designed and practically implemented, by following the biological and hydrodynamic principles which underlie the boxfish efficiency and maneuverability, which recently attracted the interest of biologists and engineers. Indeed these new kinds of fin-based propulsion mechanisms, especially for small scale AUVs, provide both an efficient thrust production and the capability of turning and maneuvering with surprising agility.

Though the model is derived *ad hoc* on the boxfish morphology, the results achieved have a more general validity, as they can be extended to the generic class of oscillating fin biomimetic underwater vehicles, with slight adjustments in the parameters. A 3-D simulation environment was set up in Matlab to test the model and design the controller, showing good agreement with experimental results. Diving and steering plane dynamics were then analyzed separately by linearizing the model equation around traditional equilibrium points, and a simple proportional controller showed good performance in the roll stabilization. Moreover, the AUV onboard sensors suite was accurately modeled, in order to test the performance of the complementary filter employed for the attitude estimation and control. Even though the geometric approach adopted in the attitude controller design can not be directly applied to the AUV actuation system (i.e. pectoral and caudal fins), its promising results suggest the integration of such algorithm with fins hydrodynamic equations as a possible future work.

As regarding the practical aspects, the estimator used in the control loop to compute the AUV state variables proved to be very precise and reliable, and its

robustness and computational ease makes it a valid option for many time-critical underwater as well as aerial applications.

The actuation system is based on PWM controlled servos driving the respective fin, which oscillate in a sinusoidal fashion. In particular, it was demonstrated how pectoral fins can be successfully used both to control the AUV orientation and to provide forward thrust at the same time; in fact such a pectoral fin dominant motion pattern was observed among boxfishes when hovering or cruising at low speeds.

Another important aspect considered is the possibility to accurately control the yaw orientation through the roll angle, and this provides a full control of the AUV in the yaw plane by using the only two pectoral fins.

5.1 Future directions

The results achieved in this work suggest some possible developments and directions to follow in biomimetic AUV design and control; in particular, an integration between the geometric control law for the AUV attitude stabilization and the fin actuation seems to be the natural continuation of the work done so far. This requires control law 3.9 to be rewritten taking into account the hydrodynamics of the fins. Also, in order to obtain good results, a precise parametrization of fin hydrodynamic coefficients should be done, possibly by calculating the specific lift and drag coefficients through nonlinear identification techniques.

Another interesting issue which, to the best author's knowledge, has not been formalized yet, is the study of possible interactions between pectoral and caudal fins, due to the short distance between them. In other terms, is it possible to exploit the vortices generated by pectoral fins, for instance, to produce torques in the steering or diving plane? PIV analysis of different motion patterns could yield interesting results.

Finally, sensory system can be further improved, with the introduction, for instance, of magnetic or light sensors: in fact the only gyroscopes and accelerometers can not provide reliable information about the heading of the AUV, which can only be estimated through the integration of gyroscopes data, with inevitable drift error. In order to reduce these errors, an estimator should be designed to compute the offsets in the sensor data, thus making measures more reliable.

Appendix A

Hydrodynamics basic concepts

To discuss the AUV dynamics and to derive its model, the reader should be familiar with some basic hydrodynamic notions. In the present section these concepts are only briefly introduced, with no pretension for completeness; for an exhaustive treatment the reader is referred to hydrodynamics textbooks such as [11] and [12]. Throughout the work some basic hypotheses regarding the fluid are assumed to hold, in order to simplify the model derivation. In particular, the flow is considered to be inviscid, irrotational and incompressible, and therefore potential flow approximation can be used.

A.1 Dimensionless parameters

The following non dimensional parameters are often used in hydrodynamics, to describe the flow regime and the related viscous effects.

- *Reynolds number.* It represents the ratio between inertial and viscous forces, as it involves the forward speed[1] of the considered body U, the characteristic length of the body l (e.g. the fin length), and the kinematic viscosity ν of the fluid in which the body is submerged. It is defined as

$$Re = \frac{Ul}{\nu} \tag{A.1}$$

  This non dimensional parameter is only an approximation to describe the relative importance of inertial forces with respect to viscous forces, nevertheless it is very useful, especially because it distinguishes the laminar flow, turbulent flow

[1] In the case of fins, this parameter is replaced by ωl, where ω is the fin beat natural frequency and l the length of the fin.

or transition flow (where both regimes are found). Moreover, it is an important factor to take into account when scaling the model for tests and practical experiments (e.g. in wind tunnels or small scale reproductions of bigger vehicles): the parameters should be scaled in order to provide the same Reynolds number as the original model, so that a similar behavior is expected.

- *Froude number*. Similar to the previous one, it defines the ratio of inertial and gravitational forces, and it is defined as follows:

$$Fr = \frac{U}{\sqrt{gl}} \tag{A.2}$$

where g is the gravity force; again, if oscillating fins are considered, then the body velocity U is to be replaced with the fin velocity ωl.

- *Strouhal number*. It refers to oscillating flow with a periodic pattern, as, for instance, the vorticity generated by oscillating fins. In particular, it is defined as:

$$St = \frac{fl}{U} \tag{A.3}$$

where f is the fin beat frequency and U is the velocity of the fluid. It is mostly used in unsteady flow calculations, as for Von Karman vortex streets.

A.2 Geometry of the fin

Some basic elements and terminology about fin shape and geometry are now introduced; as an illustrative example, consider the fin shape depicted in Fig. A.1, in which some basic geometrical quantities, such as chord length, span length and and leading and trailing edge are illustrated. Since the vehicle is assumed to cruise at a speed considerably slower compared with the velocity of the pectoral fins, then the angle of attack can be defined as the geometric angle between the stroke plane and the fin plate. Another important geometric fin parameter is the aspect ratio, defined as:

$$AR \triangleq \frac{s^2}{S} \tag{A.4}$$

where s is the fin span and S is the projection of the fin surface on the y_f-z_f plane.

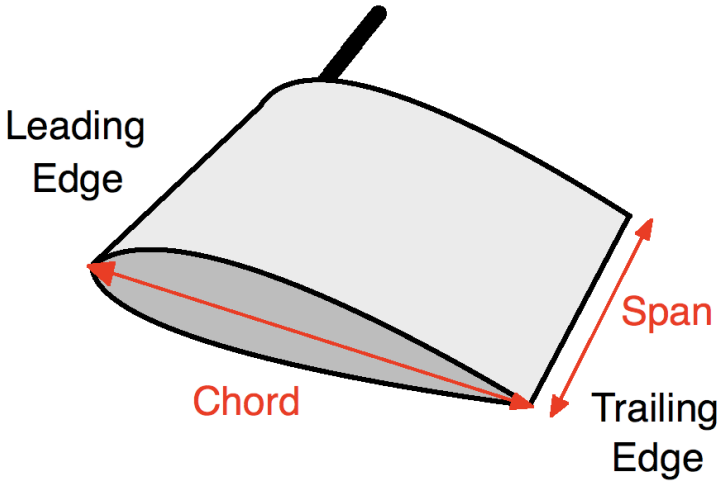

FIGURE A.1: Sketch of the left pectoral fin.

A.3 Fin hydrodynamics

Any submerged body is subject to two hydrodynamic forces when the fluid flows past it: *drag* and *lift*; conventionally, drag acts in the same direction as the free stream, while lift acts in orthogonal direction, regardless of the angle of attack. The equation governing these hydrodynamic forces are traditionally written as:

$$\begin{cases} F_L = \frac{1}{2}\rho A U^2 C_L \\ F_D = \frac{1}{2}\rho A U^{"} C_D \end{cases} \tag{A.5}$$

where ρ is the density of the fluid in which the body is submerged, A is the body surface, U the flow speed and C_L and C_D are, respectively, the lift and drag coefficients, which typically depend on the angle of attack α, on the Reynolds number and on the geometry of the fin.

Though the inviscid flow hypothesis remains valid, viscous effects cannot be completely disregarded, as they have a strong influence in drag and lift generation[2]; therefore the Kutta condition is supposed to be valid, and this lets the main viscous effects to be taken into account, confining them at the same time to a thin boundary layer. According to Kutta condition the flow is considered to leave smoothly the trailing edge, that is without creating vortices (the starting vortex which forms at

[2]According to D'Alembert paradox, an inviscid, irrotational and incompressible fluid would produce no drag, in contrast with what is observed in reality

the trailing edge is neglected). However, if the trailing edge is sufficiently sharp, a net circulation is generated around the fin, and this produces, according to Kutta-Joukowsky theorem, a lift force at the center of pressure of the fin.

Appendix B

The experimental setup

The model used to collect the experimental data and to test the control algorithms was developed at University of Delaware on the work by Kodati *et al.* [40, 83]. The model which houses the electronics — that is, the control board, the sensory system and the actuators, see Fig. B.1 — is encased in a rigid hull, fabricated with

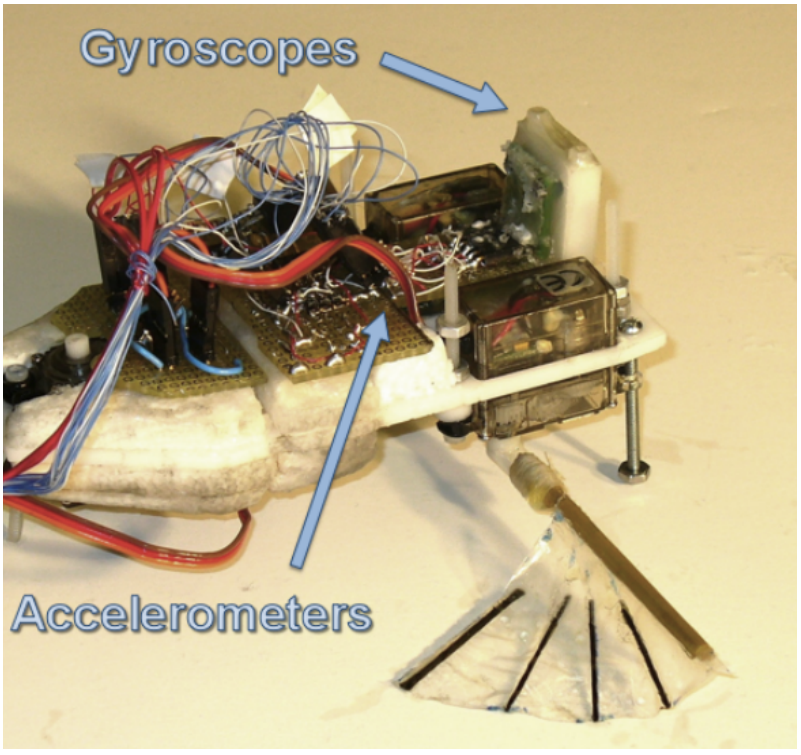

FIGURE B.1: The model in which the circuit board, the actuators and the sensory system are installed.

stereolithographic techniques on the basis of the real boxfish carapace shape (shown in Fig. B.2).

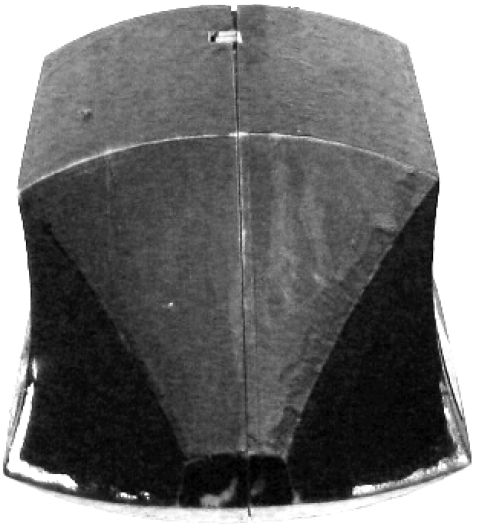

FIGURE B.2: Front view of the rigid hull encasing the model.

B.1 Sensor Suite

The AUV is equipped with a ADXL330 3-axis accelerometer by Analog Devices, capable of measuring both static and dynamic acceleration; its main purpose is that of measuring the gravity acceleration in body frame in order to provide the gravity vector $\mathbf{g}^*$ for the sensor fusion algorithm.

Two dual axis gyroscopes IDG-300 by InvenSense are mounted onboard to collect the angular rate in the three body frame axes, i.e. the angular velocity vector $\boldsymbol{\omega}_{gyr}$.

B.2 Actuators

Three Pololu GWSPARK HPXF servos are employed to drive the two pectoral fins and the tail fin, through a pulse width modulation (PWM) signal generated in Labview environment. The angle of attack of the pectoral fins can be set arbitrarily through a small screw placed at the basis of the fin. Fins are made with a 0.51mm thick polycarbonate foil, cut in a rectangular fashion with area $A_p = 0.0057m^2$.

B.3 Control

The whole control loop is implemented in Labview, according to the block diagram shown in Fig B.3. Sensory data is acquired by the control board at high sampling rate

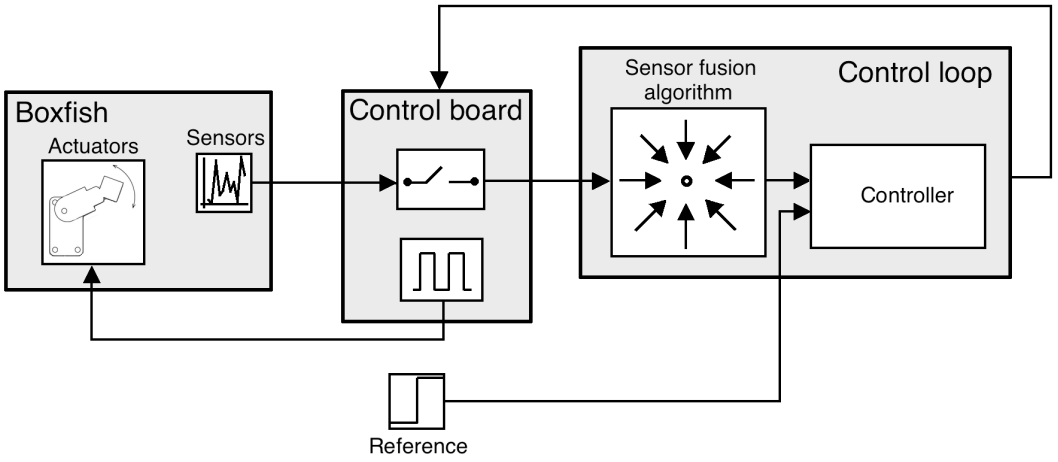

FIGURE B.3: Schematic of the boxfish control system.

(100kHz), to allow a first thermal noise filtering, whereas the frequency of the control loop and of the PWM signals for the servos is set to 50Hz. The synchronization of the whole control platform is performed through the digital counter mounted on the control board.

Bibliography

[1] M. Dickinson, C. Farley, R. Full, M. Koehl, R. Kram, and S. Lehman. How animals move: an integrative view. *Science*, 288(5463):100–106, 2000.

[2] M. Sfakiotakis, D. Lane, and B. Davies. Review of fish swimming modes for aquatic locomotion. *IEEE Journal of Oceanic Engineering*, 24(2):237–252, 1999.

[3] G. Lauder and P. Madden. Learning from fish: kinematics and experimental hydrodynamics for roboticists. *International Journal of Automation and Computing*, 3(4):325–335, 2006.

[4] J. Tangorra, S. Davidson, I. Hunter, P. Madden, G. V. Lauder, H. Dong, M. Bozkurttas, and R. Mittal. The development of a biologically inspired propulsor for unmanned underwater vehicles. *IEEE Journal of Oceanic Engineering*, 32(3):533–550, 2007.

[5] E. Mbemmo, Z. Chen, S. Shatara, and X. Tan. Modeling of biomimetic robotic fish propelled by a ionic polymer-metal composite actuator. In *IEEE International Conference on Robotics and Automation*, pages 689–694, 2008.

[6] U. K. Müller, E. J. Stamhuis, and J. J. Videler. Hydrodynamics of unsteady fish swimming and the effects of body size: comparing the flow fields of fish larvae and adults. *Journal of Experimantal Biology*, 203:193–206, 2000.

[7] M. S. Triantafyllou, G. S. Triantafyllou, and D. K. P. Yue. Hydrodynamics of fishlike swimming. *Annual Reviews Fluid Mechanics*, 32:33–53, 2000.

[8] R. Alexander. Optimization and gaits in the locomotion of vertebrates. *Physiological Reviews*, 69:1199–1227, 1989.

[9] C. C. Lindsey. Form, function and locomotory habits in fish. *Fish Physiology*, 7, 1978.

[10] E. Colgate and K. Lynch. Mechanics and control of swimming: a review. *IEEE Journal of Oceanic Engineering*, 29(3):660–673, 2004.

[11] W.P. Boyle. *Applied fluid mechanics*. McGraw-Hill Education, 1987.

[12] J. N. Newman. *Marine hydrodynamics*. MIT Press, 1977.

[13] D. Weish. Stability versus maneuverability in aquatic locomotion. *Integrative and Comparative Biology*, 42:127–134, 2002.

[14] P. Webb. Maneuverability - General issues. *IEEE Journal of Oceanic Engineering*, 29(3):547–555, 2004.

[15] G. Stein. Respect the unstable. *IEEE Control System Magazine*, 23(4):12–25, August 2003.

[16] I. K. Bartol, M. S. Gordon, M. Gharib, J. R. Hove, P. Webb, and D. Weish. Flow patterns around the carapace of rigid-bodied, multi-propulsor boxfishes (Teleostei: Ostraciidae). *Integrative and Comparative Biology*, 42:971–980, 2002.

[17] I. K. Bartol, M. Gharib, P. W. Webb, D. Weish, and M. S. Gordon. Body-induced vortical flows: a common mechanism for self-corrective trimming control in boxfishes. *Journal of Experimantal Biology*, 208:327–344, 2005.

[18] I. K. Bartol, M. S. Gordon, P. Webb, and M. Gharib. Evidence of self-correcting spiral flows in swimming boxfishes. *Bioinspiration and Biomimetics*, 3:1–7, 2008.

[19] M. S. Gordon, J. R. Hove, P. Webb, and D. Weish. Boxfishes as unusually well-controlled autonomous underwater vehicles. *Phisiological and Biochemical Zoology*, 73(6):663–671, 2000.

[20] J. R. Hove, L. M. O'Brian, M. S. Gordon, P. W. Webb, and D. Weish. Boxfishes (Teleostei: Ostraciidae) as a model system for fishes swimming with many fins: kinematics. *Journal of Experimantal Biology*, 204:1459–1471, 2001.

[21] URL `http://www.emercedesbenz.com/Images/Nov05/17BionicCarPhotos/BionicCar1.jpg`.

[22] P. Egeskov, A. Bjerrum, A. Pascoal, C. Silvestre, C. Aage, and L. W. Smitt. Design, contruction and hydrodynamic testing of the AUV MARIUS. *Proceedings of the 1994 Symposium on Autonomous Underwater Vehicle Technology*, pages 199–207, 1994.

[23] P. Bhatta and N. Leonard. Stabilization and coordination of underwater gliders. In *Proceedings of the 41st IEEE Conference on Decision and Control*, pages 1–6, 2002.

[24] J. Graver, J. Liu, C. Woolsey, and N. Leonard. Design and analysis of and underwater vehicle for controlled gliding. In *Proceedings of the 1998 Conference on Information Science and Systems*, pages 801–806, 1998.

[25] K. A. Morgansen, P. A. Vela, and J. W. Burdick. Trajectory stabilization for a planar carangiform robot fish. In *Proceedings of the 2002 IEEE International Conference on Robotics and Automation*, volume 1, pages 756–762, 2002.

[26] K. A. Morgansen, T. M. La Fond, and J. X. Zhang. Agile maneuvering for fin-actuated underwater vehicles. In *Proceedings of the 2006 Second International Symposium on Communications, Control and Signal Processing*, 2006.

[27] D. Barrett, M. Grosenbaugh, and M. Triantafyllou. The optimal control of a flexible hull robotic undersea vehiclepropelled by an oscillating foil. In *Proceedings of the 1996 Symposium on Autonomous Underwater technology*, pages 1–9, 1996.

[28] J. Yu, M. Tan, S. Wang, and E. Chen. Development of a biomimetic robotic fish and its control algorithm. *IEEE Transactions on Syatems, Man, and Cybernetics, Part B*, 34(4):1798–1810, 2004.

[29] J. Ayers, C. Wilbur, and C. Olcott. Lamprey robots. In *Proceedings of the International Symposium on Aqua Biomechanisms*, pages 1–6, 2000.

[30] K. A. McIsaac and J. P Ostrowski. Motion planning for anguilliform locomotion. *IEEE Transactions on Robotics and Automation*, 19(4):637–652, 2003.

[31] N. Kato, B. W. Wicaksono, and Y. Suzuki. Development of biology-inspired autonomous underwater vehicle "BASS III" with high maneuverability. In *Proceedings of the 2000 International Symposium on Underwater technology*, pages 84–89, 2000.

[32] URL `http://www.naoe.eng.osaka-u.ac.jp/~kato/fin.html`.

[33] C. Georgiades. Simulation and control of an underwater hexapod robot. Master's thesis, Department of Mechanical Engineering McGill University, Montreal, 2005.

[34] C. Georgiades, M. Buehler, and M. Nahon. Simulation of an underwater hexapod robot. In *Proceedings of the 14th Symposium on Unmanned Untethered Submersible Technology*, volume 36, pages 39–47, 2005.

[35] S. Guo, T. Fukuda, and K. Asaka. A new type of fish-like underwater microrobot. *IEEE/ASME Transactions on Mechatronics*, 8(1):136–141, 2003.

[36] X. Ye, Y. Su, S. Guo, and L. Wang. Design and realization of a remote control centimeter-scale robotic fish. In *Proceedings of the 2008 IEEE/ASME International Conference on Advanced Intelligent Mechatronics*, pages 25–30, 2008.

[37] X. Deng, L. Schenato, W. C. Wu, and S. Sastry. Flapping flight for biomimetic robotic insects: part I - system modeling. *IEEE Transactions on Robotics*, 22 (4):776–788, 2006.

[38] X. Deng and S. Avadhanula. Biomimetic micro underwater vehicle with oscillating fin propulsion: system design and force measurement. In *Proceedings of the 2005 IEEE International Conference on Robotics and Automation*, pages 3312–3317, 2005.

[39] C. Watts and E. Macauley. Modelling and control of a biomimetic underwater vehicle with a tendon drive propulsion system. *Oceans 2007 - Europe*, pages 1–6, 2007.

[40] P. Kodati and X. Deng. Towards the body shape design of a hydrodynamically stable robotic boxfish. In *Proceedings of the 2006 IEEE/RSJ International Conference on Intelligent Robots and Systems*, pages 5412–5417, 2006.

[41] P. Kodati. Biomimetic micro underwater vehicle with ostraciiform locomotion: system design, analysis and experiments. Master's thesis, University of Delaware, 2006.

[42] P. Kodati and X. Deng. Experimental studies on the hydrodynamics of a robotic ostraciiform tail fin. In *Proceedings of the 2006 IEEE/RSJ International Conference on Intelligent Robots and Systems*, pages 5418–5423, 2006.

[43] D. Lachat, A. Crespi, and A. J. Ijspeert. Boxybot: a swimming and crawling fish robot controlled by a central pattern generator. In *The First IEEE/RAS-EMBS International Conference on Biomedical Robotics and Biomechatronics*, pages 643–648, 2006.

[44] W. L. Chan, T. Kang, Y. J. Lee, S. K. Sung, and K. J. Yoon. Swimming study on an ostraciiform fish robot. In *International Conference on Control, Automation and Systems*, pages 700–705, 2007.

[45] D. Campolo, L. Schenato, L. Pi, X. Deng, and E. Guglielmelli. Multimodal sensor fusion for attitude estimation of micromechanical flying insects: A geometric approach. In *IEEE/RSJ International Conference on Intelligent Robots and Systems*, pages 3859–3864, 2008.

[46] M. Nahon. A simplified dynamics model for autonomous underwater vehicles. In *Proceedings of the 1996 Symposium on Autonomous Underwater technology*, pages 373–379, 1996.

[47] A. Alessandri, M. Caccia, G. Indiveri, and G. Veruggio. Application of LS and EKF techniques to the identification of underwater vehicles. In *Proceedings of the IEEE International Conference on Control Applications*, volume 2, pages 1084–1088, 1998.

[48] N. Patel, S. Gano, and J. Renaud. Simulation model of an autonomous underwater vehicle for design optimization. In *45th AIAA/ASME/ASCE/AHS/ASC Structures, Structural Dynamics and Materials Conference*, 2004.

[49] S. Sastry. *Nonlinear systems*. Springer, 1999.

[50] B. Siciliano, L. Sciavicco, L. Villani, and G. Oriolo. *Robotics - modelling, planning and control*. Springer, 2009.

[51] R. M. Murray, Z. Li, and S. S. Sastry. *A mathematical introduction to robotic manipulation*. CRC Press, 1994.

[52] C. E. Brennen. A review of added mass and fluid inertial forces. Technical report, Naval Civil Engineering Laboratory, 1981.

[53] J. N. Newman. The added moment of inertia of two-dimensional cylinders. *Journal of Ship Research*, 23:1–8, 1979.

[54] R. Madhan, Elgar Desa, S. Prabhudesai, Ehrlich Desa, A. Mascarenhas, Pramod Maurya, G. Navelkar, S. Afzulpurkar, S. Khalap, and L. Sebastiao. Mechanical design and development aspects of a small AUV - Maya. In *7th IFAC Conference MCMC2006 (Maneuvering and Control of Marine Craft)*, 2006.

[55] P. Maurya, E. Desa, A. Pascoal, E. Barros, G. Navelkar, R. Madhan, A. Mascarenhas, S. Prabhudesai, S. Afzulpurkar, A. Gouveia, S. Naroji, and L. Sebastiao. Control of the MAYA AUV in the vertical and horizontal planes: theory and practical results. In *7th IFAC Conference MCMC2006 (Maneuvering and Control of Marine Craft)*, 2006.

[56] W. Wang and C. M. Clark. Modeling and simulation of the VideoRay Pro III underwater vehicle. *Oceans 2006 - Asia Pacific*, pages 1–7, 2007.

[57] T. I. Fossen. *Guidance and control of ocean vehicles.* John Wiley and Sons, England, 1994.

[58] K. Low, S. Prabu, J. Yang, S. Zhang, and Y. Zhang. Design and initial testing of a single-motor-driven spatial pectoral fin mechanism. *Proceedings of the 2007 IEEE International Conference on Mechatronics and Automation*, pages 503–508, 2007.

[59] N. Kato and M. Furushima. Pectoral fin model for maneuver of underwater vehicles. *Proceedings of the 1996 Symposium on Autonomous Underwater Vehicle Technology*, pages 49–56, 1996.

[60] F. Chiu, C. Chen, and J. Guo. A practical method for simulating pectoral fin locomotion of a biomimetic autonomous underwater vehicle. *Symposium on Underwater Technology*, pages 323–329, 2004.

[61] D. Tzeranis, E. Papadopoulos, and G. S. Triantafyllou. On the design of an autonomous robot fish. In *Proceedings of the 11th IEEE Mediterranean Conference on Control and Automation*, pages 1–6, 2003.

[62] K. A. Morgansen. Geometric methods for modeling and control of free-swimming fin-actuated underwater vehicles. *IEEE Transaction on Robotics*, 23(6):1184–1199, 2007.

[63] T. Wang, W. Ma, and J. L. Ma. Study on control algorithm of tail fin flapping of robofish. In *IEEE International Conference on Industrial Informatics*, pages 815–820, 2006.

[64] Y. Handoko, Y. Y. Nazaruddin, B. Riyanto, and E. Leksono. Study on turning and straight motion of a fish robot using catching prey and escape behaviors mode. In *Proceedings of the Second Indonesia Japan Joint Scientific Symposium*, pages 157–160, 2006.

[65] J. M. Anderson, K. Stritlein, D. S. Barrett, and M. S. Triantafyllou. Oscillating foils of high propulsive efficiency. *Journal of Fluid Mechanics*, 360:41–72, 1998.

[66] A. J. Healey, S. M. Rock, S. Cody, D. Miles, and J. P. Brown. Toward an improved understanding of thruster dynamics for underwater vehicles. In *Proceedings of the 1994 Symposium on Autonomous Underwater Vehicle Technology*, pages 340–352, 1994.

[67] M. R. Chaithanya and K. Venkatraman. Hydrodynamic propulsion of a flexible foil undergoing pitching motion. In *10th Annual Computational Fluid dynamics Symposium*, pages 1–6, Bangalore, 2008.

[68] Q. Zhu and K. Shoele. Propulsion performance of a skeleton-strengthened fin. *Journal of Experimantal Biology*, 211:2087–2100, 2008.

[69] P. Prempraneerach, F. S. Hover, and M. S. Triantafyllou. The effefct of chordwise flexibility on the thrust and efficiency of a flapping foil. Technical report, Department of Ocean Engineering, Massachussets Institute of Technology, 2003.

[70] F. Repoulias and E. Papadopoulos. Three dimensional trajectory control of underactuated auvs. In *Proceedings of the European Control Conference*, pages 3492–3499, 2007.

[71] C. Silvestre and A. Pascoal. Depth control of the infante auv using gain- scheduled reduced order output feedback. *Control Engineering Practice*, 15(7):883–895, 2007.

[72] L. Rodrigues, P. Tavares, and M. Prado. Sliding mode control of an AUV in the diving adn steering plane. In *Proceedings of the MTS/IEEE Oceans '96. Prospects for the 21st Century*, volume 2, pages 576–583, 1996.

[73] S. Singh, A. Simha, and R. Mittal. Biorobotic AUV maneuvering by pectoral fins: inverse control design based on CFD parametrization. *IEEE Journal of Oceanic Engineering*, 29(3):777–785, July 2004.

[74] M. Narasimhan. Optimal yaw regulation and trajectory control of biorobotic AUV using mechanical fins based on CFD parametrization. *Journal of Fluids Engineering*, 128:687–698, July 2006.

[75] D. Fryxell, P. Oliveira, A. Pascoal, and C. Silvestre. An integrated approach to the design and analysis of navigation, guidance and control systems for AUVs. In

Proceedings of the 1994 Symposium on Autonomous Underwater Vehicle Technology, pages 208–217, 1994.

[76] W. C. Wu, R. J. Wood, and R. S. Fearing. Halteres for the micromechanical flying insect. In *Proceedings of the 2002 IEEE International conference on Robotics and Automation*, volume 1, pages 60–65, 2002.

[77] F. Bullo and A. D. Lewis. *Geometric control of mechanical systems: modeling, analysis, and design for simple mechanical control systems.* Springer, 2005.

[78] V. I. Arnold. *Mathematical methods of classical mechanics.* Springer-Verlag, 2nd edition, 1989.

[79] D. H. S. Maithripala, J. M. Berg, and W. P. Dayawansa. An intrinsic observer for a class of simple mechanical systems on a Lie Group. In *Proceeding of the American Control Conference*, volume 2, pages 1546–1551, Boston, Massachusetts, 2004.

[80] D. H. S. Maithripala, J. M. Berg, and W. P. Dayawansa. Almost-global tracking of simple mechanical systems on a general class of Lie Groups. *IEEE Transactions on Automatic Control*, 51(2):216–225, 2006.

[81] F. Bullo and R. M. Murray. Tracking for fully actuated mechanical systems: a geometric framework. Technical report, Control and Dynamical Systems, California Institute of Technology, Pasadena, CA, 1997.

[82] D. E. Koditschek. The application of total energy as a Lyapunov function for mechanical control systems. In J. E. Marsden, P. Sambamurthy and J. C. Simo, *Dynamics and control of multibody systems*, volume 97, pages 131–157. American Mathematical Society, 1988.

[83] P. Kodati, J. Hinkle, A. Winn, and X. Deng. Microautonomous robotic ostraciiform (MARCO): hydrodynamics, design and fabrication. *IEEE Transactions on Robotics*, 24(105-117), 2008.

[84] Z. Deng, M. Richmond, G. Guensch, and R. Mueller. Study of fish response using particle image velocimetry and high-speed, high-resolution imaging. Technical report, U.S. Department of Energy, 2004.